SCUOLA DI DOTTORATO
UNIVERSITÀ DEGLI STUDI DI MILANO-BICOCCA

Department of Material Science

PhD program in Materials Science and Nanotechnology

Cycle XXXVIII

Hybrid Solid-State Nanopores for Engineer Ion Channels

Shukun Weng

Registration number 907325

Tutore / Tutor: Sergio Brovelli

Supervisor: Denis Garoli

Coordinatore / Coordinator: Francesco Montalenti

ACADEMIC YEAR 2024/2025

“欲速则不达”

— 孔子，《论语·子路》

“Haste makes waste”

— Confucius, The Analects

Abstract

Dynamic control of ion transport at the nanoscale is essential for advancing nanofluidic systems toward applications in biosensing, energy conversion, and iontronic computing. Conventional solid-state nanopores, while mechanically robust and geometrically tunable, are fundamentally passive and lack the adaptive functionality of biological ion channels. This thesis explores three hybrid strategies that transform passive nanopores into actively programmable ionic devices by integrating responsive polymers, two-dimensional materials, and chemically reactive electrolytes.

First, thermoplasmonic gating is realized by functionalizing SiN nanopores with the thermoresponsive polymer PNIPAM and a plasmonic bullseye structure. Localized laser heating induces reversible polymer collapse, achieving an on/off ratio up to 60 and millisecond switching times, with spatial selectivity enabling multi-pore logic operations. Second, an electrically gated MoS_2/SiN hybrid nanochannel is developed, where gate voltage modulates surface charge asymmetry to control ion conductance, rectification. The nanochannel also shows potential for scalable osmotic power generation, with a power density of up to ~33,700 W/m², as well as prolonged protein translocation enabled by interactions between unfolded bovine serum albumin and sulfur vacancies on MoS_2. Third, a chemically gated mechanism is introduced based on voltage-controlled precipitation and dissolution of metal phosphates inside SiN nanopores. This approach yields extreme rectification ratios exceeding 40,000, history-dependent conductance, and memristive switching with sub-nanowatt power consumption. In-situ surface-enhanced Raman spectroscopy provides direct vibrational evidence of reversible precipitate formation within the pore.

Together, these hybrid nanopore systems demonstrate progressively increasing levels of transport programmability—from externally triggered gating to continuously tunable electrostatic control and finally to a two-terminal memory device. The results establish potential routes towards smart nanofluidic devices, iontronic circuits, and neuromorphic computing platforms.

Content

Chapter 1 Introduction

Ever since the famous speech given by Richard Feynman, nanotechnology has been widely explored in different areas with huge progress established. As an effective sensor, nanopore help to explore the nanoscale world, has established its importance role in single molecule detection especially for DNA sequencing. From bionanopore to solid-state-nanopore, with the help of advanced modern nanofabrication techniques, the application of interest for nanopores are gradually shifting from maturely explored DNA sequencing to complicated protein sequencing, as well as other potential applications such as nanoscale chemical reaction monitoring, osmotic power generation, fluidic neuromorphic computing (e.g. ionic transistor, ionic memristor…) [1–3].

1.1 Nanopores as Confined Ionic Transport Systems

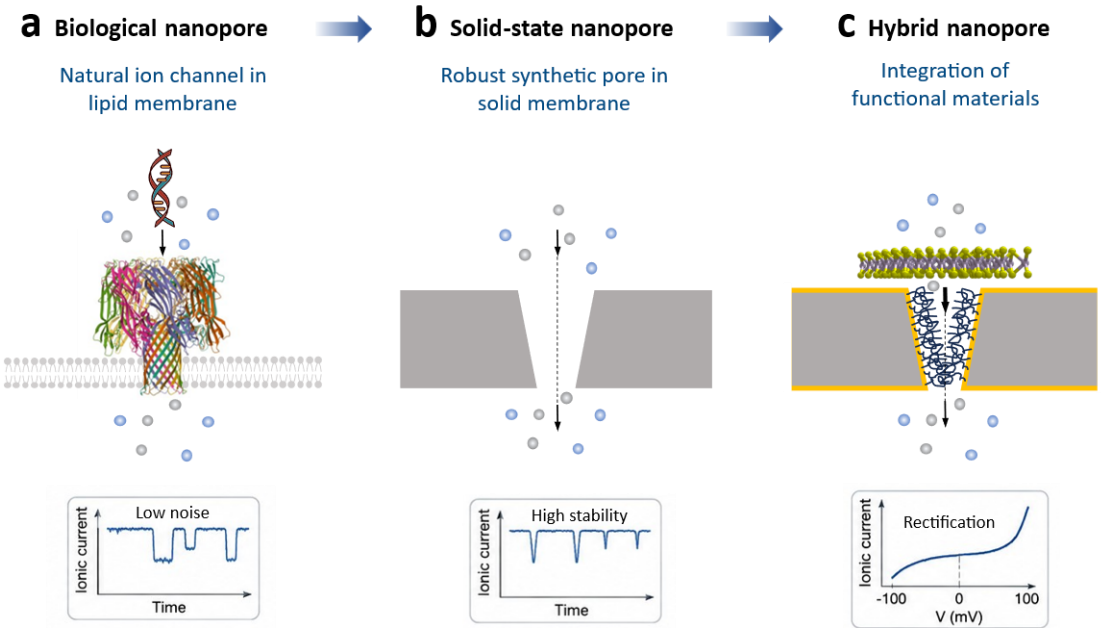

Figure 1.1 Evolution of nanopore technologies from biological nanopores toward dynamically regulated hybrid iontronic systems. ***a*** *Early biological nanopores provided highly selective molecular transport.* ***b*** *The development of solid-state nanopores enabled mechanically robust and geometrically tunable nanofluidic devices.* ***c*** *Subsequent integration of responsive functional interfaces introduced active transport modulation capabilities. protein structure obtained from Protein Data Bank (www.rcsb.org)*

Nanopores are nanometer-scale apertures that confine the transport of ions and molecules into dimensions comparable to their characteristic electrostatic and hydrodynamic length scales. Under such confinement, ionic transport deviates fundamentally from macroscopic electrolyte behavior and becomes increasingly governed by surface interactions, electrical double layer overlap, ion selectivity, and nonlinear electrokinetic phenomena. Because of this, nanopores are not merely miniature holes in membranes, but functional nanofluidic elements capable of actively regulating ionic transport.

The conceptual origin of nanopore sensing can be traced to the Coulter counter, developed in the 1950s, which detected suspended particles through transient changes in ionic current as particles passed through a microscale aperture. Scaling this principle down to the nanometer regime enabled the detection of single biomolecules. A landmark advance was reported by Kasianowicz et al. in 1996, who demonstrated that single-stranded DNA molecules could translocate through the biological nanopore α-hemolysin while generating characteristic ionic current blockades [4]. This experiment established nanopores as single-molecule analytical platforms and initiated the field of nanopore-based biosensing.

Biological nanopores, typically protein ion channels embedded within lipid bilayers, possess atomically defined geometries and highly evolved functionalities such as voltage gating, ligand responsiveness, and ion selectivity. These properties enable remarkable sensing performance, including single-base discrimination during DNA sequencing. However, biological nanopores also suffer from several practical limitations, including limited mechanical stability, sensitivity to environmental conditions, restricted pore geometries, and difficulties in large-scale integration with conventional microfabrication technologies [5].

To overcome these limitations, solid-state nanopores emerged as an alternative platform. Solid-state nanopores are typically fabricated in silicon nitride, silicon dioxide, graphene, MoS_2, or polymer membranes using focused ion beam milling, transmission electron microscopy drilling, dielectric breakdown, or lithographic methods [6–8]. Compared to biological nanopores, solid-state systems offer superior mechanical robustness, tunable geometry, chemical stability, and compatibility with semiconductor processing techniques. Most importantly, they provide a versatile platform for engineering ion transport through independent control of pore size, geometry, surface chemistry, and external stimuli [1,5,9,10].

As the characteristic dimensions of nanopores approach the Debye screening length, surface charge effects increasingly dominate ionic transport. Counterions accumulate near charged pore walls to form electrical double layers (EDLs), while co-ions are partially excluded [11,12]. In sufficiently small nanopores, overlapping EDLs can produce ion-selective transport, concentration polarization, ionic rectification, and nonlinear current-voltage behavior. These phenomena distinguish nanofluidic transport from bulk electrolyte conduction and create opportunities for controlling ionic motion using external electrical, optical, chemical, or mechanical stimuli [10].

Consequently, nanopores have evolved beyond their original role as passive sensing elements. Increasingly, they are being explored as dynamically controllable nanofluidic systems capable of emulating functionalities traditionally associated with biological ion channels and electronic devices. This transition—from passive transport structures toward active iontronic elements—forms the conceptual foundation of this thesis (Figure 1.1).

1.2 From Passive Nanopores to Active Ionic Devices

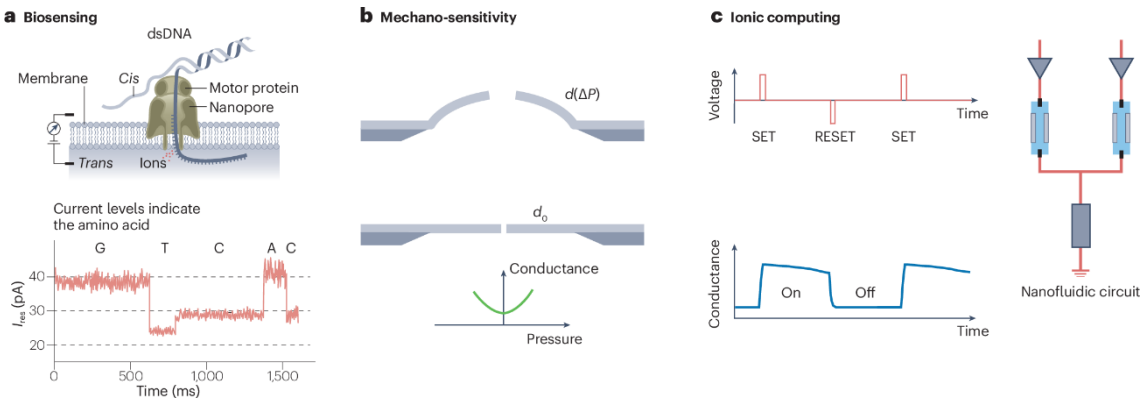

Figure 1.2 Evolution of nanopore functionalities. ***a*** *Nanopore sequencing using a biological nanopore and motor protein (top) reads the DNA bases as levels of different heights (bottom) in the current trace.* ***b*** *An example of mechano-sensitivity. When pressure is applied, the deformation of a nanopore enlarges its cross-section and conductance; d_0 is the pore diameter at rest and $d(\Delta P)$ is the diameter under applied pressure. Another scenario involves a nonlinear coupling resulting in a parabolic G–P curve.* ***c*** *Ionic computing with a nanofluidic memristor. The device conductance can be set and reset with high-amplitude positive or negative voltage pulses. Right: logic circuit with two nanofluidic memristors; by connecting two nanofluidic memristors in this way, Boolean operations can be implemented. dsDNA, double-stranded DNA. Reprinted with permission from ref [1].*

Despite their advantages, conventional solid-state nanopores remain fundamentally passive systems. Their transport characteristics are primarily determined by static structural parameters such as pore diameter, aspect ratio, and intrinsic surface charge.

Once fabricated, these properties are difficult to dynamically modulate. As a result, traditional solid-state nanopores exhibit limited adaptability, restricted selectivity, and relatively simple transport behavior compared to biological ion channels [5].

In biological systems, ion transport is highly dynamic and tightly regulated. Voltage-gated ion channels open or close in response to membrane potential changes, ligand-gated channels respond to chemical binding events, and mechanosensitive channels react to external mechanical forces. These gating mechanisms enable complex behaviors such as neuronal signaling, adaptive transport regulation, and synaptic plasticity (Figure 1.2). The dynamic nature of biological ion channels illustrates that efficient information processing and selective transport require active control over ionic conduction rather than static structural confinement alone.

Replicating such adaptive functionality in artificial nanofluidic systems has become a major objective in nanopore research. The central challenge is therefore no longer merely fabricating smaller nanopores, but engineering nanopores whose transport properties can be actively modulated by external stimuli. To better achieve this objective requires integrating functional materials, responsive interfaces, or active environments within robust solid-state nanopores [13].

One important consequence of dynamic transport regulation is the emergence of iontronic functionality. Analogous to semiconductor electronics, iontronic systems seek to manipulate ionic transport through functionalities such as gating, rectification, switching, and memory effects. Various ionic analogs of electronic components, including ionic diodes, ionic transistors, and nanofluidic memristors, have been demonstrated in recent years. Unlike electronic systems, however, iontronic devices involve the coupled transport of charged species, solvent molecules, and chemical information, resulting in rich nonequilibrium transport phenomena that are strongly influenced by nanoscale interfacial interactions.

The development of dynamically controllable nanofluidic systems has also expanded the functional scope of nanopores beyond molecular sensing. Emerging applications now include osmotic energy harvesting, adaptive filtration, ion-based logic operations, neuromorphic computing, responsive drug delivery, and bioinspired transport regulation [13–17]. Recent studies have further established that nanofluidic memristive behavior can be programmed through electrolyte composition, surface interactions, channel geometry, and electrical excitation conditions, highlighting the rich coupling

between nanoscale confinement and ionic memory effects [18]. These advances suggest that the central challenge in modern nanofluidics is no longer merely the fabrication of smaller nanopores, but the development of systems in which ionic transport can be actively programmed and dynamically controlled.

This functionality shifting has driven the emergence of hybrid nanofluidic systems. In these devices, a mechanically stable solid-state nanopore serves as the structural framework, while an integrated functional component introduces responsiveness, nonlinearity, selectivity, or memory effects. The interaction between the scaffold and the functional element enables forms of ion transport control that cannot be achieved using homogeneous materials alone. Hybrid nanopores therefore represent an important transition in nanofluidics: from passive ionic conduits toward dynamically programmable iontronic devices.

1.3 Hybrid Strategies for Active Ion Modulation

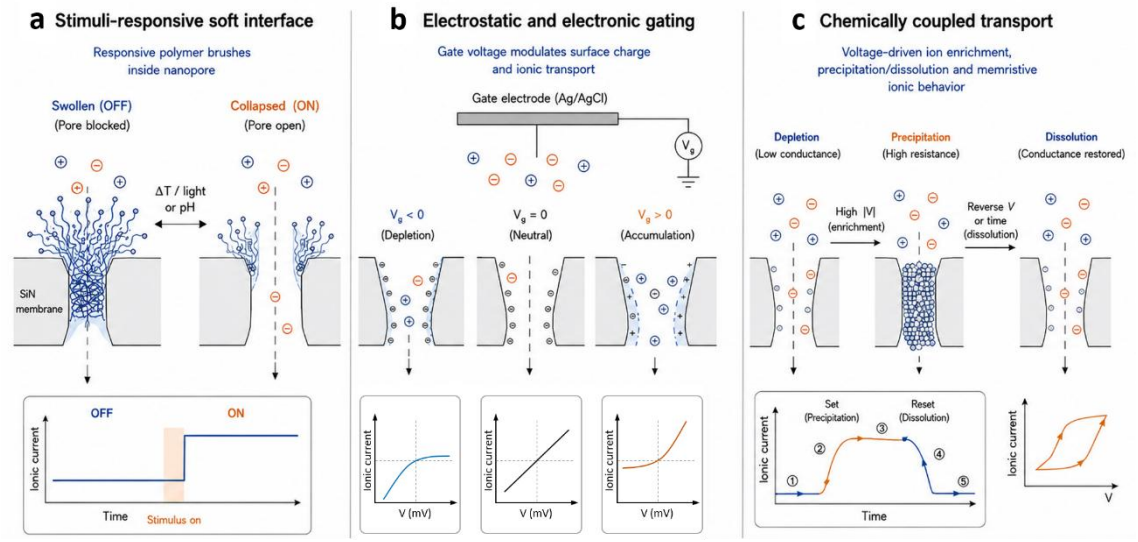

Figure 1.3 Strategies of hybrid nanopore system. ***a*** *Stimuli-responsive materials integrated within a nanopore with two distinguishable states in the presence or absence of external stimuli.* ***b*** *Electrode integrated nanopore system displaying diode-like I-V behavior under varying gating conditions.* ***c*** *Controllable nanoscale chemical reaction integrated inside nanopore system showing time dependent-ionic current.*

Hybrid nanofluidic systems encompass a broad range of architectures, including biohybrid interfaces, stimuli-responsive materials, electrochemical systems, optofluidic structures, as well as chemically active components. Because many of these systems involve multiple coupled physical effects, a strict material-based classification is often

ambiguous. In this thesis, hybrid nanopores are instead organized according to the dominant mechanism through which ionic transport is dynamically regulated. Among the various approaches reported so far, three representative and conceptually distinct strategies are particularly relevant to the systems investigated in this thesis: stimuli-responsive soft interfaces, electrostatic and electronic gating systems, and chemically coupled transport systems (Figure 1.3).

1.3.1 Stimuli-Responsive Soft Interfaces

One widely explored strategy for dynamic ion transport regulation involves the integration of stimuli-responsive materials into nanopores and nanochannels. In these systems, soft or adaptive interfaces reversibly modify the effective pore geometry, surface wettability, steric confinement, or local ionic environment in response to external stimuli.

A variety of responsive materials have been investigated for this purpose, including polymer brushes, hydrogels, self-assembled molecular layers, DNA nanostructures, and biomolecular assemblies. These systems can respond to temperature, light, pH, ionic strength, magnetic fields, or molecular recognition events through reversible conformational changes [10].

Among these materials, thermoresponsive polymers such as poly(N-isopropylacrylamide) (PNIPAM) have attracted particular attention because of their lower critical solution temperature (LCST) behavior [19–21]. Below the LCST, PNIPAM chains adopt a swollen hydrophilic state, while above the LCST they collapse into a denser hydrophobic conformation. When confined inside nanopores, this transition can dynamically regulate ionic conductance by modifying the accessible transport volume and interfacial properties.

Responsive nanofluidic systems enable several important transport functionalities, including reversible ionic gating, dynamic selectivity control, nonlinear conductance modulation, and adaptive transport regulation [22]. Coupling responsive interfaces with localized actuation methods such as plasmonic heating or optical excitation further enables spatiotemporal control of ionic transport with high precision.

Compared with purely static nanopores, responsive nanofluidic systems more closely resemble biological ion channels in their ability to dynamically regulate ionic conductance in response to environmental changes. As a result, these systems represent an important route toward adaptive nanofluidic devices and biomimetic ionic transport architectures.

1.3.2 Electrostatic and Electronic Gating

Another important mechanism for programmable ionic transport relies on electrostatic and electronic modulation of nanochannels. At nanometer length scales, ionic transport is highly sensitive to surface charge due to the formation of electrical double layers at solid-liquid interfaces. Consequently, modulation of surface potential can strongly influence ion distribution, ionic conductance, and transport selectivity.

This principle forms the basis of electrically gated nanofluidic devices, often referred to as ionic transistors or nanofluidic field-effect systems. In these architectures, external gate voltages are used to dynamically modulate surface charge density or local electrostatic potential within the nanochannel, thereby enabling active regulation of ionic transport analogous to carrier modulation in semiconductor electronics.

Various electronically active materials have been explored for electrically gated nanofluidics, including conductive polymers, carbon nanotubes, graphene, MXenes, and semiconducting two-dimensional materials such as MoS_2 [23]. Two-dimensional materials are particularly attractive because their atomic-scale thickness enables strong electrostatic coupling between electronic and ionic degrees of freedom while simultaneously providing nanoscale confinement [24].

Electrostatically gated nanofluidic systems have demonstrated a broad range of functionalities including ionic rectification, tunable ion selectivity, osmotic energy conversion, ionic logic operations, and programmable conductance modulation [13,25–27]. Compared with geometry-based gating strategies, electrostatic modulation enables continuous and reversible control over ionic transport without requiring large structural changes in the nanopore itself.

The coupling between ionic transport and electronically tunable interfacial states provides an important foundation for future iontronic devices integrating nanofluidics with electronic control architectures.

1.3.3 Chemically Coupled Ion Transport

In addition to structural and electrostatic regulation, ionic transport in nanoconfined systems can also become strongly coupled to local chemical processes occurring at solid–liquid interfaces. Under nanoscale confinement, ion transport, interfacial reactions, and concentration redistribution may interact dynamically, leading to transport behavior that deviates substantially from equilibrium nanofluidic models.

Chemically coupled nanofluidic systems arise when ionic motion influences the local physicochemical environment, while the evolving chemical state simultaneously feeds back on ionic transport. Such coupling may involve ion enrichment or depletion, local pH variation, redox reactions, adsorption and desorption processes, concentration polarization, or reaction–diffusion dynamics within confined nanochannels. Recent studies have emphasized that such chemically and electrostatically coupled processes are central to the emergence of history-dependent and memristive ion transport, where changes in interfacial chemistry and ion redistribution can serve as internal state variables [28]. Because these processes occur on length scales comparable to ionic screening and molecular transport distances, relatively small local chemical variations can produce significant changes in ionic conductance and selectivity.

Compared with passive transport systems governed primarily by fixed geometry and surface charge, chemically coupled nanofluidic systems often exhibit strongly nonlinear and nonequilibrium behavior. In many cases, the transport properties of the nanochannel become dynamically dependent on the evolving internal physicochemical state of the system. As a result, ionic conductance may display transient switching, hysteresis, delayed relaxation, or adaptive responses under external electrical stimulation.

These nonequilibrium transport phenomena are attracting increasing interest in the emerging field of iontronics because they introduce dynamic internal-state regulation into ionic transport systems. In contrast to conventional static nanopores, chemically coupled nanofluidic systems provide a potential route toward adaptive ionic devices capable of information storage, signal processing, and bioinspired transport regulation.

1.4 Toward Programmable Iontronic Nanopore Systems

The development of hybrid nanopore systems is ultimately motivated by the broader objective of transforming passive nanofluidic channels into programmable ionic devices. In conventional solid-state nanopores, ion transport is primarily governed by fixed structural parameters such as pore geometry, surface charge, and electrolyte composition. In contrast, hybrid nanopores incorporate responsive, electronically active, or chemically dynamic components that enable the transport properties of the system to evolve under external stimuli. As a result, ionic conductance can become dynamically tunable, nonlinear, adaptive, and in some cases history dependent.

These capabilities form the physical foundation of emerging iontronic systems, in which ionic transport is manipulated analogously to electronic charge transport in semiconductor devices. Recent advances in nanofluidics have demonstrated ionic analogs of transistors, diodes, memristors, and logic elements, opening new possibilities for ion-based information processing, neuromorphic architectures, biosensing, and energy conversion [18,22,29]. In such systems, ionic transport is no longer determined solely by static confinement and equilibrium electrostatics, but also by dynamically evolving internal states arising from molecular conformational changes, electrostatic gating, ion redistribution, or electrically driven chemical reactions [18].

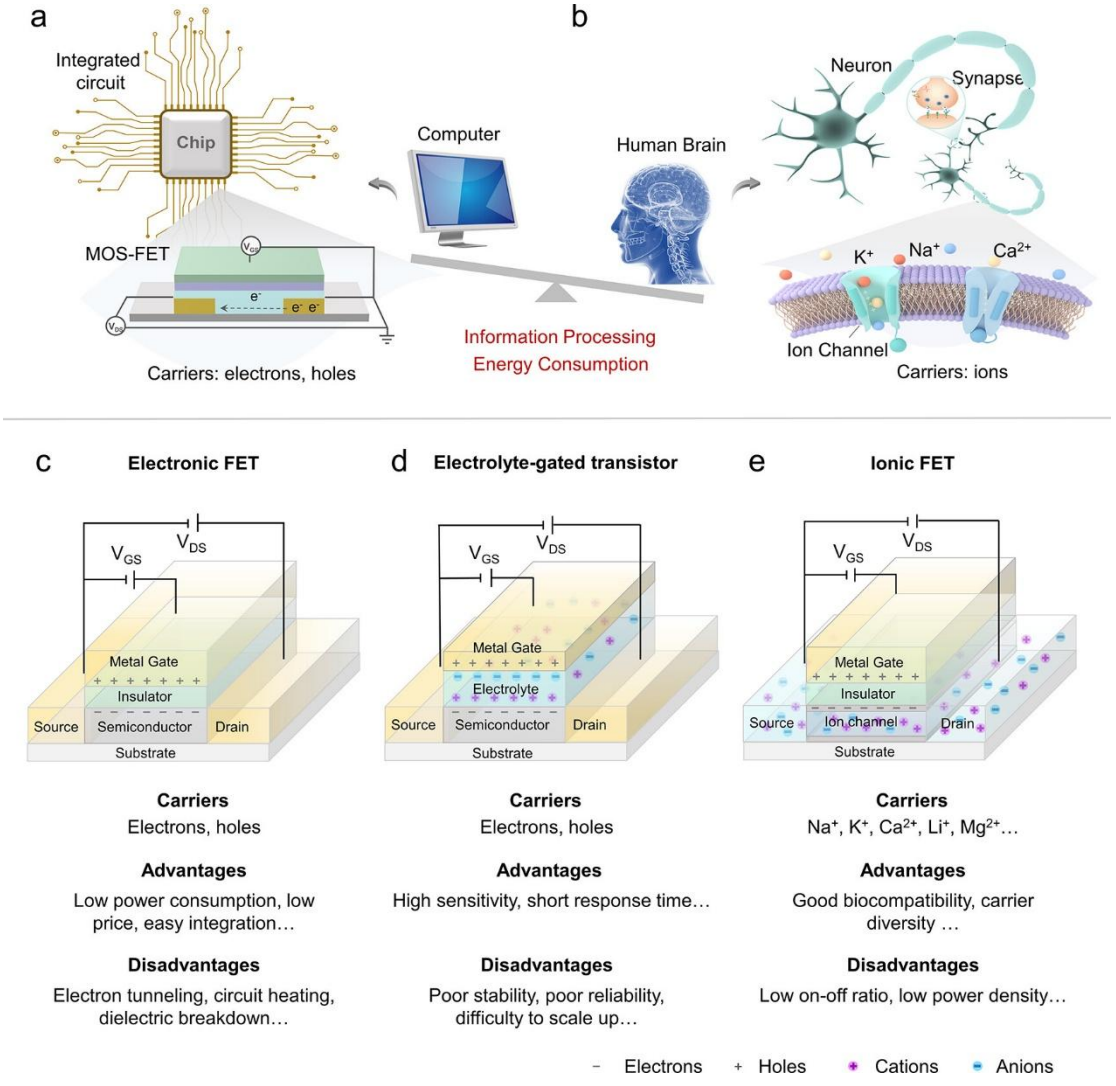

Figure 1.4 Concept schematic of ionic transistors. ***a*** *An electronic transistor with electrons as carriers is the core of electronic devices in the information age.* ***b*** *The rapid information transmission in intelligent organisms uses ions as carriers, which is both efficient and low energy consumption. Schematic structure, carriers and dis-/advantages of* ***c*** *electronic FET;* ***d*** *electrolyte-gated transistor;* ***e*** *ionic FET. Reprinted with permission from Ref [2].*

The hybrid nanopore systems investigated in this thesis represent three distinct levels of transport programmability. Chapter 3 explores reversible ionic switching through thermally responsive PNIPAM-functionalized nanopores activated by localized thermoplasmonic heating. Chapter 4 investigates continuously tunable ion transport in electrically gated MoS_2/SiN nanochannels, where gate-controlled surface charge modulation enables programmable ionic conductance and rectification. Chapter 5 further extends this concept toward adaptive and history-dependent transport through electrically induced precipitation and dissolution reactions, leading to memristive ionic behavior governed by internal chemical state evolution.

Together, these systems illustrate how hybridization strategies enable progressively more sophisticated forms of ionic transport control, ranging from externally triggered gating to adaptive iontronic functionality with memory effects. The physical concepts and device architectures developed throughout this thesis contribute to the broader emergence of programmable nanofluidic systems and provide new perspectives for future iontronic technologies.

1.5 Scope and Outline of This Thesis

This thesis investigates dynamic ion transport control in hybrid solid-state nanopores through the integration of responsive polymers, electronically active materials, and chemically reactive electrolyte systems. The central objective is to explore how hybridization strategies can progressively transform passive nanopores into actively gated nanofluidic devices with programmable transport characteristics.

Chapter 2 introduces the theoretical background of ion transport in nanofluidic systems, including electrical double layer formation, surface-charge-governed transport, ionic conductance models, ion current rectification, and electrokinetic phenomena relevant to nanopore operation.

Chapter 3 presents thermoplasmonically gated solid-state nanopores functionalized with PNIPAM. By integrating plasmonic bullseye structures with thermoresponsive polymer coatings, localized optical heating is used to achieve reversible and spatially selective ion transport gating.

Chapter 4 investigates hybrid MoS_2/SiN nanofluidic devices in which ionic conductance is dynamically modulated through electrostatic gating. The coupling

between two-dimensional materials and confined electrolytes enables voltage-controlled transport regulation and enhanced iontronic functionality.

Chapter 5 explores chemically coupled ion transport based on electrically controlled precipitation and dissolution reactions within nanopores. These reactive systems exhibit strong ionic rectification, dynamic conductance modulation, and memristive behavior arising from voltage-dependent nanochemistry.

Together, these studies demonstrate how hybrid integration enables progressively more dynamic, adaptive, and programmable ion transport behaviors in solid-state nanopores, providing a foundation for future iontronic and neuromorphic nanofluidic systems.

Chapter 2 Physical Principles of Dynamic Ion Transport in Nanopores

2.1 Ion Transport under Nanoscale Confinement

Ion transport in bulk electrolyte solutions is generally well described by continuum electrostatics and diffusion theory. However, when ionic transport is confined within nanoscale geometries whose dimensions approach the characteristic electrostatic screening length of the electrolyte, transport behavior deviates significantly from bulk behavior. Under such confinement, interfacial interactions increasingly dominate ionic motion, leading to nonlinear transport phenomena that are absent in macroscopic systems [30].

The ionic flux inside nanopores is commonly described by the coupled Poisson–Nernst–Planck (PNP) formalism, which accounts for diffusion, electromigration, and convective transport [31]. The total flux of ionic species i can be expressed as:

$$J_i = -D_i \nabla c_i - z_i \mu_i F c_i \nabla \phi + c_i \mathbf{u} \tag{2.1}$$

where D_i is the diffusion coefficient, c_i is the ion concentration, z_i is the ionic valence, μ_i is the ionic mobility, ϕ is the electrostatic potential, and $\mathbf{u}$ is the fluid velocity field. The three terms respectively represent diffusion driven by concentration gradients, migration under an electric field, and convective transport induced by fluid flow.

In nanoscale systems, these transport mechanisms become strongly coupled. Unlike macroscopic electrolyte transport, nanopore conduction is no longer governed solely by bulk ionic conductivity. Instead, the confined geometry amplifies the influence of interfacial electrostatics, resulting in ion-selective transport and nonlinear conductance behavior.

A key parameter governing nanoscale ionic transport is the Debye screening length, which characterizes the thickness of the electrical double layer (EDL) adjacent to charged solid surfaces [32]. The Debye length is given by:

$$\lambda_D = \sqrt{\frac{\varepsilon_r \varepsilon_0 k_B T}{2 N_A e^2 I}} \tag{2.2}$$

where ε_r is the dielectric constant of the electrolyte, I is the ionic strength, and the remaining symbols have their conventional meanings.

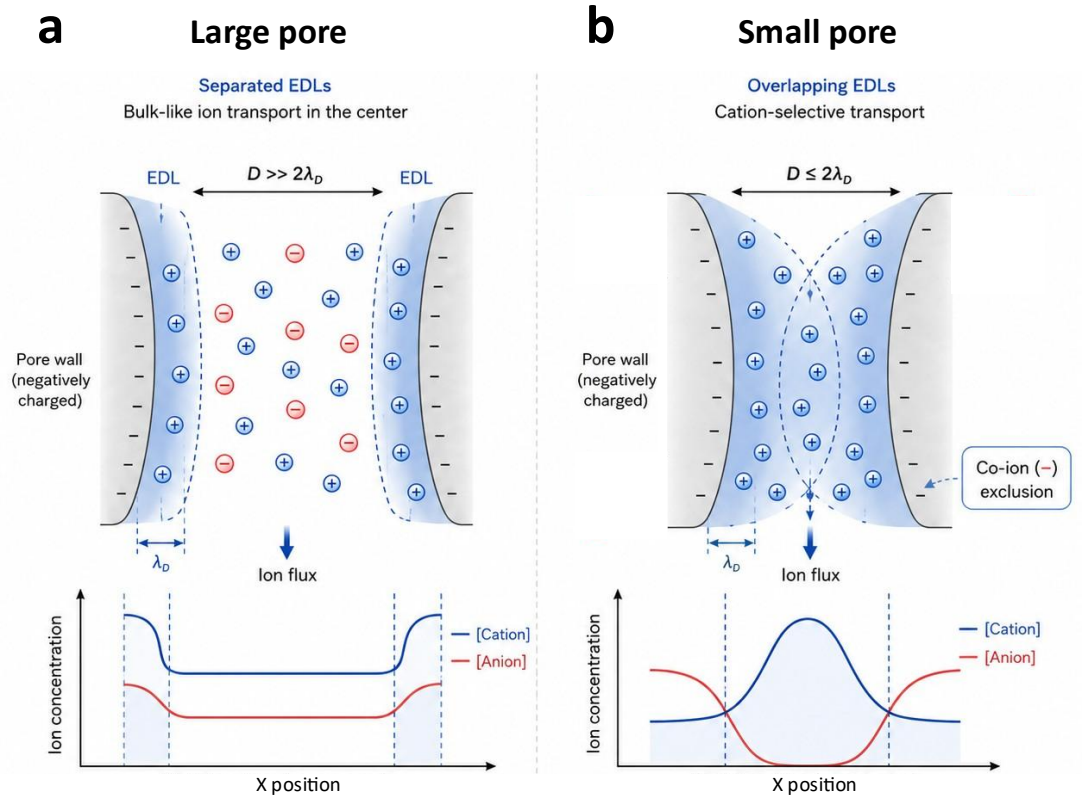

Figure 2.1 EDL overlap under nanoscale confinement. ***a*** *Big size nanopore with negligible EDL overlap, the ion current is dominated by bulk ion conductivity.* ***b*** *Small size nanopore with overlapped EDL exclude co-ions, the ion current is dominated by anti-ion conductivity near the nanopore interwall surface (as well as part of outside wall surface [33]).*

When the nanopore radius becomes comparable to the Debye length, electrical double layers originating from opposing pore walls overlap substantially. Under these conditions, ionic transport becomes dominated by surface interactions rather than bulk electrolyte properties. Counterions accumulate inside the pore while co-ions are partially excluded, resulting in selective ion transport and enhanced electrostatic sensitivity.

Another important characteristic length scale is the Dukhin length, which describes the relative contribution of surface conduction to total ionic transport. In sufficiently small nanopores or low ionic strength conditions, surface conduction can exceed bulk

conduction, leading to transport regimes fundamentally different from classical Ohmic behavior.

As a consequence, nanoscale confinement transforms nanopores into highly sensitive electrostatic transport systems in which ionic conduction can be strongly modulated by geometry, surface chemistry, external fields, and local ionic environments. These confinement-induced transport effects form the physical basis for dynamic ion gating and iontronic functionality in hybrid nanopore systems.

2.2 Surface-Charge-Governed Ion Transport

Surface charge plays a central role in determining ionic transport through nanopores. In contrast to bulk electrolyte systems, where transport is primarily governed by ion diffusion and migration in the solution volume, nanoconfined systems are strongly influenced by electrostatic interactions at the solid–liquid interface.

For silicon nitride nanopores, surface charge originates mainly from the ionization of hydroxyl and amine groups formed during surface oxidation and hydroxylation. The surface charge density depends strongly on pH, electrolyte composition, and surface functionalization. At neutral or alkaline pH conditions, silicon nitride surfaces typically exhibit negative surface charge due to deprotonation reactions.

The electrostatic interaction between charged pore walls and mobile ions leads to the formation of electrical double layers. The EDL consists of a compact Stern layer near the surface and a diffuse layer extending into the electrolyte. Within the diffuse layer, counterions accumulate to compensate the surface charge while co-ions are depleted.

When nanopore dimensions are significantly larger than the Debye length, the electrical double layers remain localized near the pore walls and transport in the center of the pore resembles bulk electrolyte behavior. However, when the pore diameter approaches the Debye length, overlapping EDLs can occupy a substantial fraction of the pore volume. Under these conditions, ionic transport becomes surface-charge governed [14].

Surface-charge-governed transport results in several important nanofluidic phenomena. First, the nanopore becomes ion selective because counterions preferentially occupy the pore interior. Second, the ionic conductance becomes highly sensitive to changes in surface charge density. Third, the transport behavior becomes increasingly nonlinear and dependent on electrolyte concentration.

The total nanopore conductance can therefore be viewed as the combination of bulk ionic conduction and surface-mediated conduction:

$$G = G_{bulk} + G_{surface} \tag{2.3}$$

At high ionic concentrations, bulk conduction dominates and the conductance scales approximately linearly with electrolyte concentration. In contrast, under low ionic strength conditions or strong confinement, surface conductance becomes increasingly important and may even dominate total ionic transport.

Because surface charge strongly influences local ion distributions, even relatively small modifications of the pore surface can produce substantial conductance changes. Functional coatings, external gate voltages, adsorbed molecules, or local chemical reactions can all modulate the electrostatic environment within the nanopore. Consequently, surface-charge-governed transport provides the fundamental mechanism underlying many active nanofluidic gating strategies.

This sensitivity to interfacial electrostatics is particularly important in hybrid nanopore systems, where functional materials are integrated specifically to dynamically manipulate the local surface environment and thereby regulate ionic transport.

2.3 Ionic Conductance and Transport Asymmetry

The ionic conductance of a nanopore depends on both its geometry and its electrostatic environment. In its simplest approximation, nanopore conductance is determined by the combined contributions of pore resistance and access resistance. For cylindrical nanopores, the conductance can be approximated as:

$$G = \kappa \left(\frac{4L}{\pi d^2} + \frac{1}{d} \right)^{-1} \tag{2.4}$$

where κ is the electrolyte conductivity, L is the pore length, and d is the pore diameter.

Although this expression captures the geometric dependence of conductance, it neglects important nanoscale effects associated with surface charge and ion selectivity. In nanoconfined systems, ionic transport becomes increasingly asymmetric due to nonuniform ion distributions inside the pore.

Ion selectivity arises when charged nanopores preferentially transport ions of one polarity. Negatively charged nanopores favor cation transport, whereas positively charged nanopores favor anion transport. This selectivity becomes particularly strong under overlapping EDL conditions.

Transport asymmetry may also arise from structural asymmetry such as conical pore geometry, asymmetric surface charge distribution, or spatially varying electrolyte concentration. Under applied voltage bias, these asymmetries generate unequal ion enrichment and depletion conditions for opposite voltage polarities. As a result, ionic current becomes direction dependent, leading to ion current rectification.

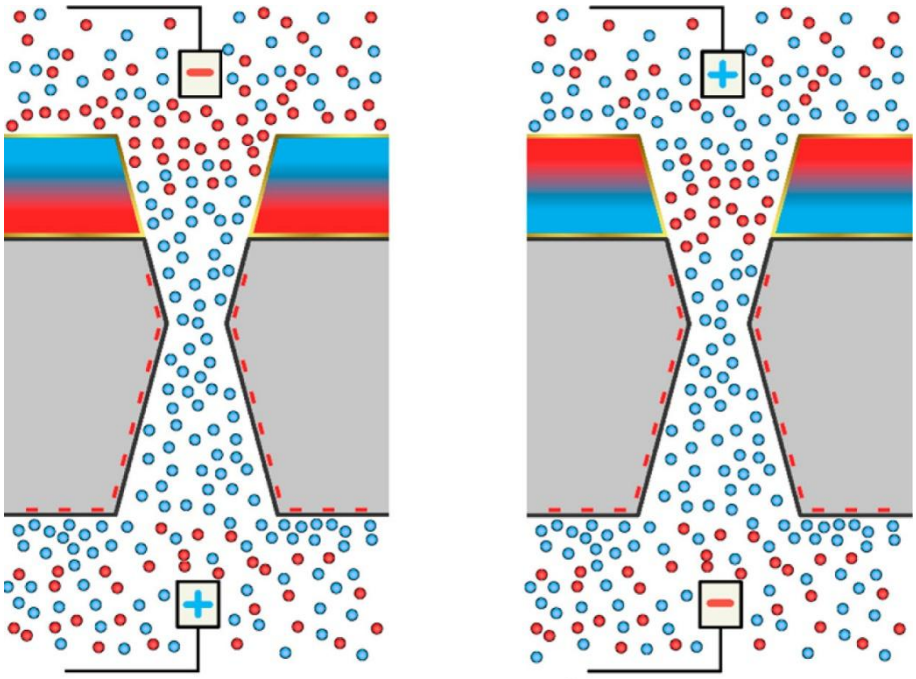

Figure 2.2 Scheme of asymmetric surface charge induced unsymmetric ion distribution inside Au/SiN nanopore. Red (blue) color in the Au layer indicates induced negative (positive) charge. The transmembrane potential causes formation of zones with effective positive and negative charges on Au; a bipolar double-layer is formed in the solution. The arrangement of the zones is dependent on the polarity of transmembrane potential. Reprinted with permission from Ref [34].

Ion current rectification is analogous to electrical diode behavior in semiconductor systems. Under forward bias conditions, ion enrichment inside the nanopore enhances conductance, whereas reverse bias conditions produce ion depletion and reduced conductance [35]. The rectification ratio is commonly defined as:

$$R_{Rect} = \left| \frac{I(+V)}{I(-V)} \right| \tag{2.5}$$

Rectification behavior is strongly influenced by surface charge density, electrolyte concentration, nanopore geometry, and external gating conditions. Importantly, rectification is fundamentally associated with asymmetric ionic concentration profiles rather than simply geometric asymmetry alone [36].

Under strong confinement or high applied electric fields, ion enrichment and depletion zones may extend beyond the nanopore into the surrounding electrolyte reservoirs. These non-equilibrium concentration fields play a crucial role in concentration polarization phenomena and dynamic ionic transport modulation.

Because ion current rectification is highly sensitive to interfacial electrostatics and local ionic distributions, it provides an effective probe of dynamic gating processes in hybrid nanopores. In particular, strong rectification behavior often emerges in systems exhibiting active ion transport modulation, concentration polarization, or chemically induced transport asymmetry.

2.4 Dynamic and History-Dependent Ion Transport

Unlike electronic conductors, ionic systems often exhibit intrinsically slow dynamical responses because ion transport involves mass motion, diffusion, adsorption, hydration rearrangement, and chemical reactions [37]. As a result, ionic conductance frequently depends not only on the instantaneous applied voltage, but also on the prior evolution of the system.

One important source of dynamic behavior arises from finite ionic relaxation times [38,39]. Following changes in applied electric field, ionic concentration distributions require finite time to reorganize inside confined nanopores. Similarly, adsorption and desorption processes at charged interfaces may evolve slowly relative to electrical excitation timescales. In chemically active systems, reaction kinetics and phase transformations can introduce even longer characteristic response times.

These delayed ionic responses often produce hysteretic current-voltage behavior. Under time-varying voltage sweeps, the ionic current may follow different trajectories depending on the direction and rate of the applied bias. Such hysteresis reflects the existence of internal transport states that evolve dynamically during operation.

Several physical mechanisms can contribute to history-dependent ionic transport, including delayed EDL relaxation, concentration polarization dynamics, ion trapping, adsorption-desorption processes, conformational transitions in responsive polymers, and electrically driven chemical reactions [3].

Among these mechanisms, chemically coupled transport is particularly important because it introduces internal state evolution directly into the transport pathway. Precipitation and dissolution reactions occurring inside nanopores can reversibly alter the

effective pore geometry, local ion selectivity, and transport resistance. Since these reactions proceed over finite timescales, the resulting conductance depends strongly on previous voltage history.

This behavior is closely related to memristive transport. A memristive system exhibits conductance states determined by the past evolution of electrical excitation. In nanofluidic systems, memristive behavior may emerge from ion redistribution, dynamic surface charge modulation, or voltage-controlled chemical transformations within confined electrolyte environments.

Compared to conventional electronic memristors based on electronic charge transport, nanofluidic memristive systems operate through ionic and chemical degrees of freedom. These systems often exhibit low operating power, rich nonlinear dynamics, and strong coupling between transport and chemistry, making them attractive candidates for iontronic and neuromorphic applications.

The dynamic transport phenomena discussed throughout this chapter provide the physical basis for the hybrid nanopore systems investigated in this thesis. In the following chapters, these principles are applied to achieve thermally gated transport using responsive polymers, electrostatically controlled ionic modulation using two-dimensional materials, and chemically induced memristive behavior through electrically controlled precipitation reactions.

Chapter 3 Light Switchable SiN Nanopore with PNIPAM Modification

Solid-state nanopores can work as artificial nanofluidic structures that mimic the gating functions of biological ion channels. They are gathering increasing attention because they represent a platform for fundamental research and are highly attractive for diverse applications [15,26,40–47]. The ability of nanopores to manipulate the movement of molecules and ions at the nanoscale is a pivotal factor driving this interest. For example, in biosensing applications, controlled gating facilitates the selective detection of biomolecules [5,48–50]. Similarly, in drug delivery systems, molecular gating enables targeted release of therapeutic agents [17]. Important recent developments in this field involved the incorporation of stimuli-responsive molecules and functional chemical groups into nanopores [51–53]. This advancement has led to the creation of "smart" nanopores and innovative nanodevices, for example by molecular recognition in nanoporous membranes and the development of tunable nanofluidic diodes [54–56]. An interesting material in this respect is PNIPAM, known for its phase transition at a lower critical solution temperature (LCST) of ≈32 °C [52,57,58]. If used as a functional layer inside a nanopore, PNIPAM can be used as a gate, *i.e.*, below the LCST, the polymer expands to block the nanopore, while above this temperature, the polymer collapses to open the pore to ionic flux [19,59–61]. This temperature-dependent behavior enables thermal modulation of the nanopore channel, offering a straightforward yet effective gating mechanism. However, the gating control reported so far relies on external heaters, which limit the system's functionality, in particular, in terms of reaction time in response to the temperature change and spatial resolution [19,44,55,61]. An important remaining challenge is the selective gating of individual nanopores within an array, which requires precise and highly localized temperature control [19,44]. In this context, plasmonic-driven optical gating represents an innovative solution that optimizes the nanopore gating by means of thermo-plasmonic effects.

In this work, the challenge of spatially selective gating was addressed by using plasmonic nanostructures for targeted heating with µm spatial resolution. We demonstrate that plasmonic nanopores as shown in Figure 3.1, functionalized with PNIPAM and surrounded by a plasmonic bullseye structure, can effectively achieve thermoplasmonic gating.

The bullseye was illuminated by a HeNe laser (at 633 nm) and focused the electromagnetic field intensity on the aperture of the nanopore, which resulted in rapid and reproducible temperature changes. The effectiveness of this thermoplasmonic modulation is demonstrated through ionic conductivity measurements within single and multiple nanopores. We achieve an On/Off ratio of up to 60 of the ionic current and stable switching demonstrated in multiple cycles. The precision, efficiency, and practicality of the thermoplasmonic nanopore gating mark a significant advancement in nanofluidics. This novel approach for selective optical gating of nanopores paves the way to new possibilities in the development of smart nanofluidic systems.

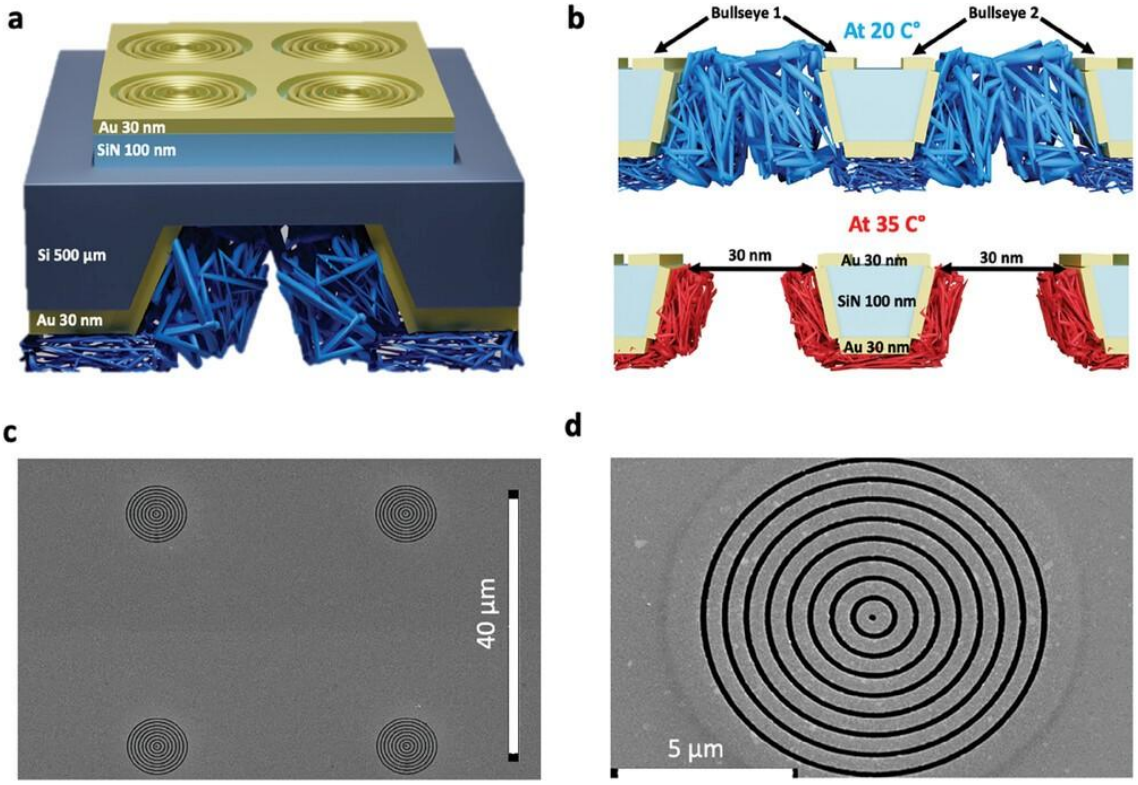

Figure 3.1 Device architecture of PNIPAM nanopores. ***a*** *illustration of an array of nanopores on the same membrane coated with PNIPAM (bottom side) and bullseye (top side).* ***b*** *illustration of two individual nanopores on the same membrane coated with PNIPAM (bottom side) and bullseye (top side) above and below the LCST value, respectively.* ***c*** *SEM image of an array of the gold plasmonic bullseye used in this work, scale bar "40 µm".* ***d*** *SEM image of plasmonic bullseye structure, scale bar "5 µm".*

3.1 Device Fabrication and Characterization

3.1.1 Membrane fabrication

Freestanding Si_3N_4 membrane chips were prepared following a standard membrane fabrication procedure. In particular, an array of square membranes was prepared on a commercial double-sided 100 nm LPCVD Si_3N_4 coated 500 µm Si wafer via UV photolithography, following reactive ion etching and subsequent KOH wet etching. Subsequently, a 5 nm layer of titanium, followed by a 30 nm layer of gold, was evaporated onto both the top and bottom sides of the membranes. This resulted in an overall membrane thickness, inclusive of the adhesion layer, measuring 170 nm. Notably, each silicon chip has dimensions of 5 × 5 mm^2 and a thickness of 500 µm. Afterward, nanopores featuring a diameter of 30 ± 10 nm, and bulls-eye milling (on the top side), were fabricated using a focused Ga^+ ion beam. Precise adjustments to milling times were made to achieve the optimized bullseye geometry.

3.1.2 PNIPAM modification

PNIPAM chains were grafted into the pores of the flat membrane using a self-assembled monolayer. The samples were plasma-treated for 60 s in oxygen. To create reactive sites on the gold surface for PNIPAM-amine (molecular weight 25 kD) attachment, 11-mercaptoundecanoic acid (MUA) was used. A solution of the thiol-based molecule 5 mM MUA in ethanol was prepared and the nanopores were immersed overnight then the samples were rinsed to remove any unbound molecules and dried under a stream of nitrogen. Finally, the samples were immersed in a solution of 400 mM EDC, 100 mM NHS, and 10 wt.% PNIPAM-amine in methanol for 3 h and then rinsed and dried under nitrogen.

3.1.3 Ion current measurements

Electrical measurements were conducted in 10 mM KCl buffer solution using the same instrument/reader from Elements srl. The measurements were performed either in the dark or under an excitation wavelength of 632.8 nm using a Renishaw InVia Raman system with a 50X long distance objective. Prior to the measurement the pores were wetted with DI/IPA for 5 min. Electrical readout of DNA and NPs translocations was conducted in 10 mM KCl by using the same instrument/reader from Elements srl. During the nanopores array measurements, objectives with different magnifications were used to

activate different pores. Figure 3.2 shows the horizontal flow cell and the setup used that allowed for optical access from the top for activation of the selective optical gating. Furthermore, when switching from one magnification to another the laser power was adjusted to be 1 mW cm^{-2}.

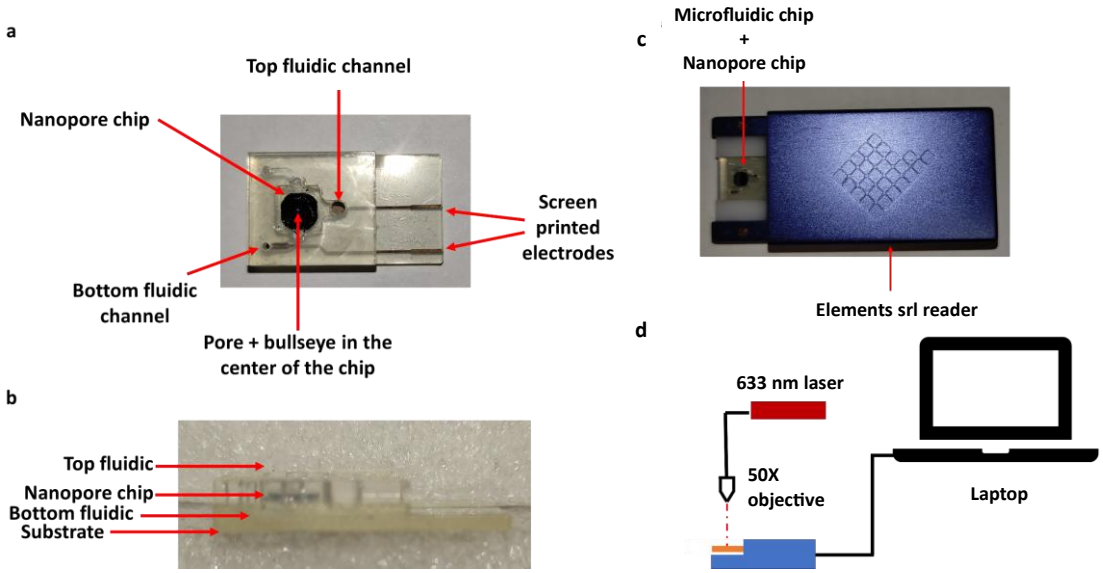

Figure 3.2 Nanopore ionic current measurement configuration. ***a*** *top view of the microfluidic chip integrated with screen printed electrodes used during the electrical measurements and showing the different parts of the microfluidic,* ***b*** *cross-view of the microfluidic showing the different parts ranging from the bottom fluidic, nanopore chip, and top fluidic,* ***c*** *top view of the electrical reader from Elements srl with the microfluidic chip,* ***d*** *illustration of the measurement set-up.*

3.2 Results and Discussion

3.2.1 Characterization of PNIPAM graft on Au

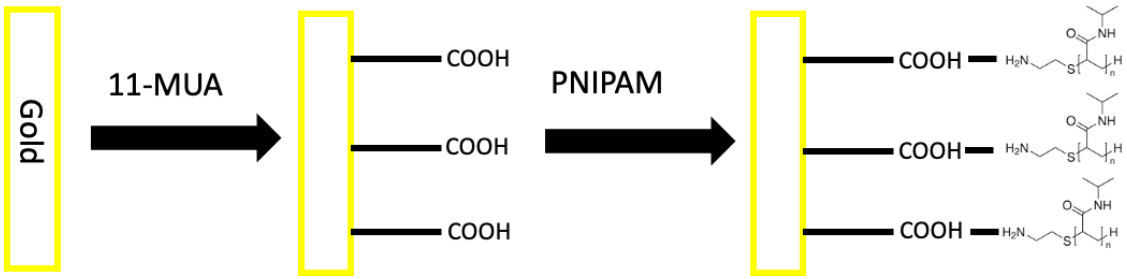

Figure 3.3 The chemical modification processes for PNIPAM grafting on gold.

The thermoplasmonic gating mechanism utilizes a combination of temperature-responsive polymers and targeted laser activation of a plasmonic bullseye structure to control the ion channel conductivity of nanopores (Figure 3.1a). As depicted in Figure 3.1b, in the absence of laser activation (at RT), the PNIPAM layer at the back side

of the nanopore remains in a swelled state as the ambient temperature is below the LCST. This swelled state of PNIPAM blocks the ion passage through the nanopore, leading to an inactive or "Off" state. Under laser illumination (T ≥ 33 °C), the increased electromagnetic field intensity induced by the bullseye leads to a local increase in temperature at the center of the bullseye where the nanopore is located, and by surpassing the LCST, causes the PNIPAM brushes to be compacted. This molecular shrinkage opens the pore, allowing the ion flow, and switches the nanopore to the "On" state as previously shown [53,57,58].

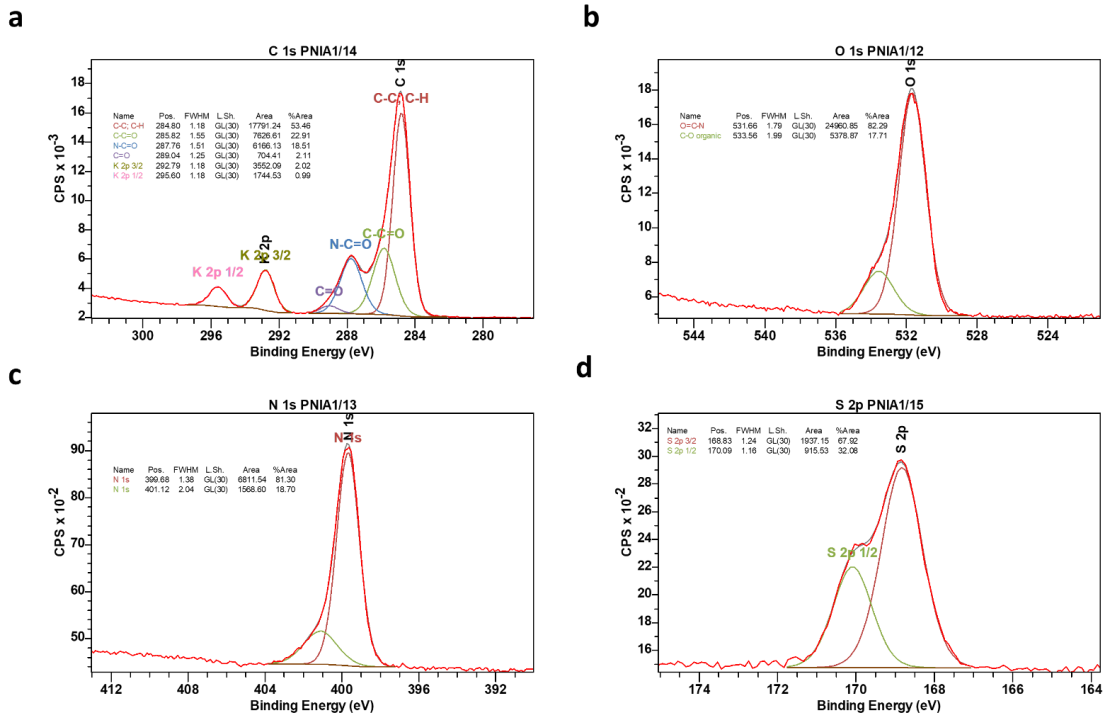

Figure 3.4 X-ray photoelectron spectra of PNIPAM grafted onto gold. ***a*** *C 1s peak,* ***b*** *O 1s peak,* ***c*** *N 1s peak,* ***d*** *S 2p peak.*

We fabricated the nanopores in a Silicon Nitride membrane with a thickness of 100 nm by focused ion beam (FIB) milling. The diameters of these nanopores were determined by two complementary methods: imaging with scanning electron microscopy (SEM), and conductance measurements in a 1 M KCl solution [62]. The latter is based on pores with a conical channel shape and correlated the ionic flux to the effective pore size. We obtained a good agreement between the pore diameters derived from the channel conductance and those imaged via Scanning Electron Microscope (SEM) thus providing reliable values for the nanopore sizes that we fabricated. In the next step, PNIPAM was covalently linked to the backside of the pore by self-assembly (as shown in Figure 3.3) to

enable the functionalization of the nanopore with PNIPAM. We note that in the calculations of the effective pore diameter, we assumed a uniform modification of the pore size and membrane surfaces, which takes also the increase in membrane thickness caused by the PNIPAM layer into account.

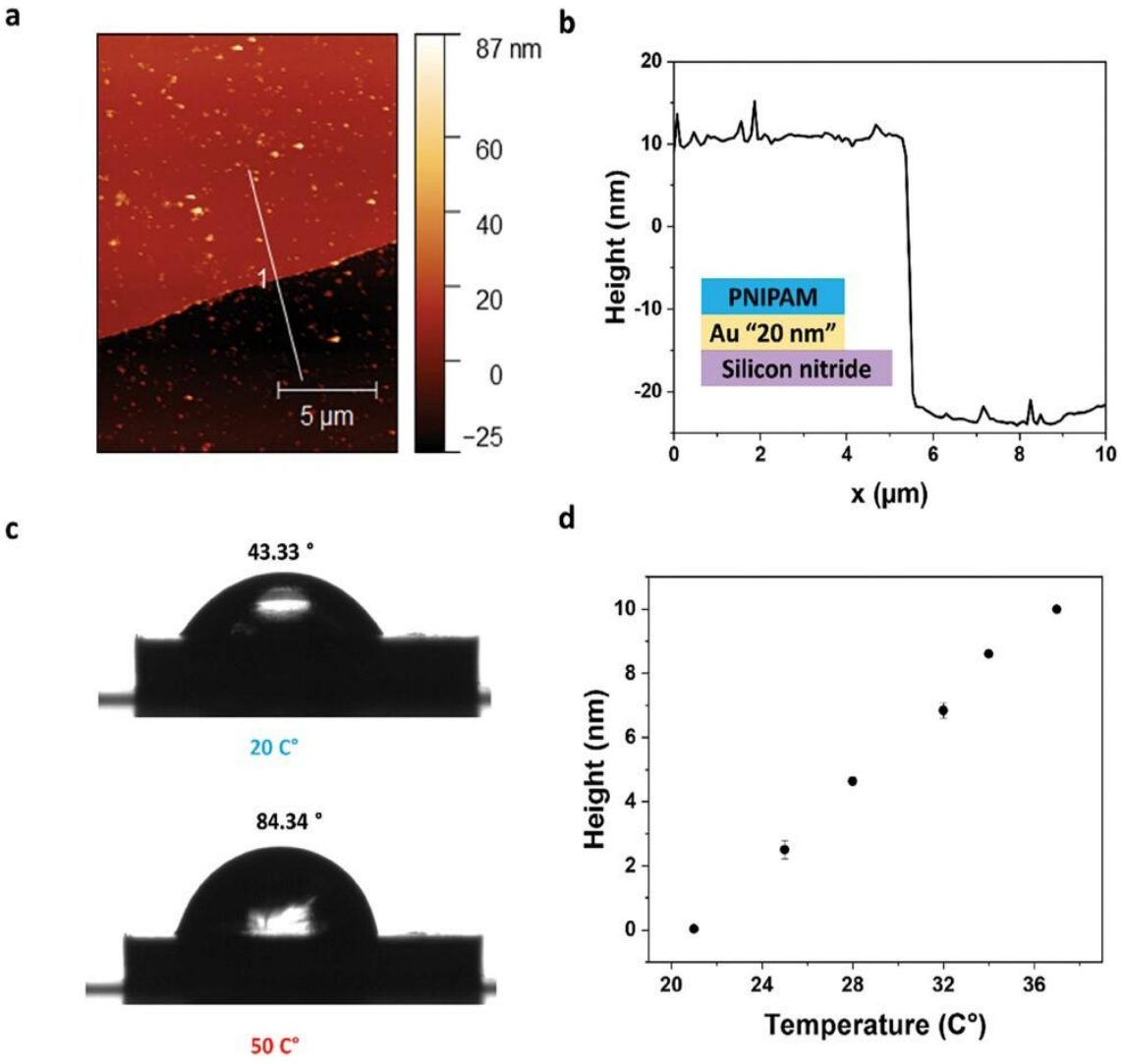

Figure 3.5 Characterization of Au layer surface with PNIPAM. ***a*** *AFM image and* ***b*** *the profile of elongated PNIPAM indicates a layer of 10 nm thick at room temperature.* ***c*** *contact angle measurement showing the change in wettability of the PNIPAM film, demonstrating a decrease in hydrophilicity and the state switch from hydrophilic to less hydrophilic.* ***d*** *the response of a QCM sensor functionalized with PNIPAM in 10 mM KCl at different temperatures from 23 to 40 °C, the PNIPAM-modified sensor exposed to a gradual increase in the temperature showed a decrease in the thickness of the PNIPAM layer.*

To corroborate the effective immobilization of PNIPAM (blue layer) on the nanopores, X-ray photoelectron spectroscopy (XPS) was performed. The XPS spectra displayed in Figure 3.4 show a carbon peak at 283.1 electron volts (eV), a nitrogen peak at 397.9 eV, and an oxygen peak at 529.8 eV that are characteristic of the elemental composition of

PNIPAM [63]. They reveal three types of carbon **c** species, each corresponding to different bonding within the PNIPAM molecule. The peak at 285.0 eV was attributed to carbons in C─C and C─H bonds, commonly found in the backbone of the polymer chain. The peak at 286.1 eV corresponded to carbon-nitrogen (C─N) bond that is a key component of the PNIPAM structure. The peak at 287.8 eV can be associated with C═O bonds, which is indicative of the carbonyl groups in the polymer [64–66]. The distinct presence of these peaks confirmed the successful immobilization of PNIPAM on the nanopores.

We used atomic force microscopy (AFM) to investigate the PNIPAM film morphology on a flat surface (Figure 3.5a) at room temperature. Knowledge of the film thickness and roughness is important, because the thickness needs to be tailored to the nanopore size to enable switching, and the roughness determines the accuracy of the switching mechanism. The height profile in Figure 3.5a exhibits a film with a 10 nm thickness and homogenous surface texture with a roughness of ≈1 nm that demonstrates the uniform PNIPAM surface coating.

To confirm the thermo-responsive nature and the hydrophobic/hydrophilic switching behavior of the PNIPAM film, we performed contact angle measurements at two distinct temperatures above and below LCST: 50 and 20 °C (Figure 3.5b,c). At 50 ° C we observe a large contact angle (84.34 °) that stems from high hydrophobicity. This conformation is attributed to the contraction of polymer chains above the LCST of PNIPAM, which is ≈32 ° C. At 20 ° C (below LCST), the contact angle is much smaller (44.03 °), implying a more hydrophilic and expanded state of the polymer [58,59].

The critical role of PNIPAM thickness variation in the gating mechanism of the nanopore requires detailed control of this parameter for temperatures below and above the LCST at which the switching is operated. We used a quartz crystal microbalance with dissipation monitoring (QCM-D) to obtain a qualitative assessment of conformational changes of the PNIPAM film with temperature. This technique is particularly effective in evaluating the restricted movement of PNIPAM when tethered to surfaces, thereby approximating both the dynamics within the nanopore sensors, as well as mimicking comparable surface chemistry, as a gold-coated quartz crystal was used for measurements. A temperature increases from room temperature to above LCST resulted in a notable

increase of frequency of ≈ 60 Hz, as well as an increased dissipation of $\approx 2 \times 10^{-6}$ (Figure 3.6). Based on the measured dissipation limit, we concluded that we could approximate the polymer height based on the Sauerbrey equation, which models the polymer as a rigid film [67]. The Sauerbrey equation relates the change in frequency to the change in mass of the film. Our data yields a decrease in polymer layer thickness of ≈ 10 nm (Figure 3.5d) upon increased temperature exposure. This indicates that PNIPAM undergoes a transition to a more compact structure as the temperature surpasses the LCST.

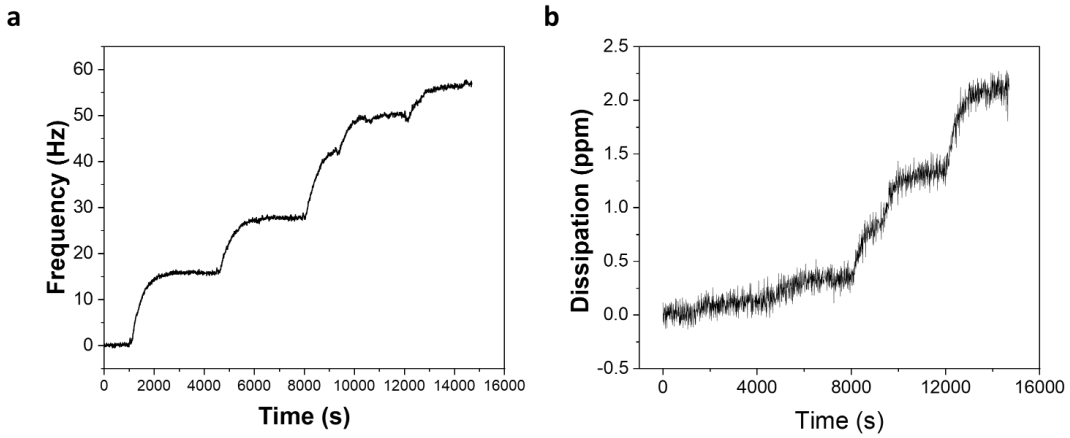

Figure 3.6 QCM of PNIPAM/Au/SiN sample. ***a*** *The frequency change of PNIPAM immobilized on QCM balance upon temperature increase.* ***b*** *The dissipation changes of PNIPAM immobilized on QCM balance upon temperature increase results in a dissipation increase of ~ 2.2 parts per million (ppm).*

The integration of SEM, AFM, XPS, and contact angle analysis provided a comprehensive characterization of gold surfaces grafted with PNIPAM. This multifaceted approach confirmed the successful functionalization of nanopores with PNIPAM. Importantly, these analyses confirmed the ability of PNIPAM to modify its physical state in response to thermal stimuli, notably transitioning from hydrophilic to hydrophobic properties as temperatures exceed its LCST. Additionally, AFM and QCM-D analyses elucidated the layer thickness of PNIPAM and the height variation upon heating beyond the LCST, leading to insights on the optimal pore diameter for effective pore blockage.

3.2.2 PNIPAM phase change via plasmonic heating

After characterizing the PNIPAM layer, the coated nanopores underwent electrical (ionic) measurements. The reported gating mechanism in this work relies on plasmonic heating to modulate the pore temperature, causing the PNIPAM layer to swell or shrink. Figure 3.7a shows that without laser activation, the PNIPAM layer remains

swollen at temperatures below the LCST, blocking ion passage and keeping the nanopore in an "Off" state. Upon laser illumination, the local temperature exceeds the LCST, shrinking the PNIPAM brushes, opening the pore, and allowing ion flow, thus switching the nanopore to the "On" state (Figure 3.7b).

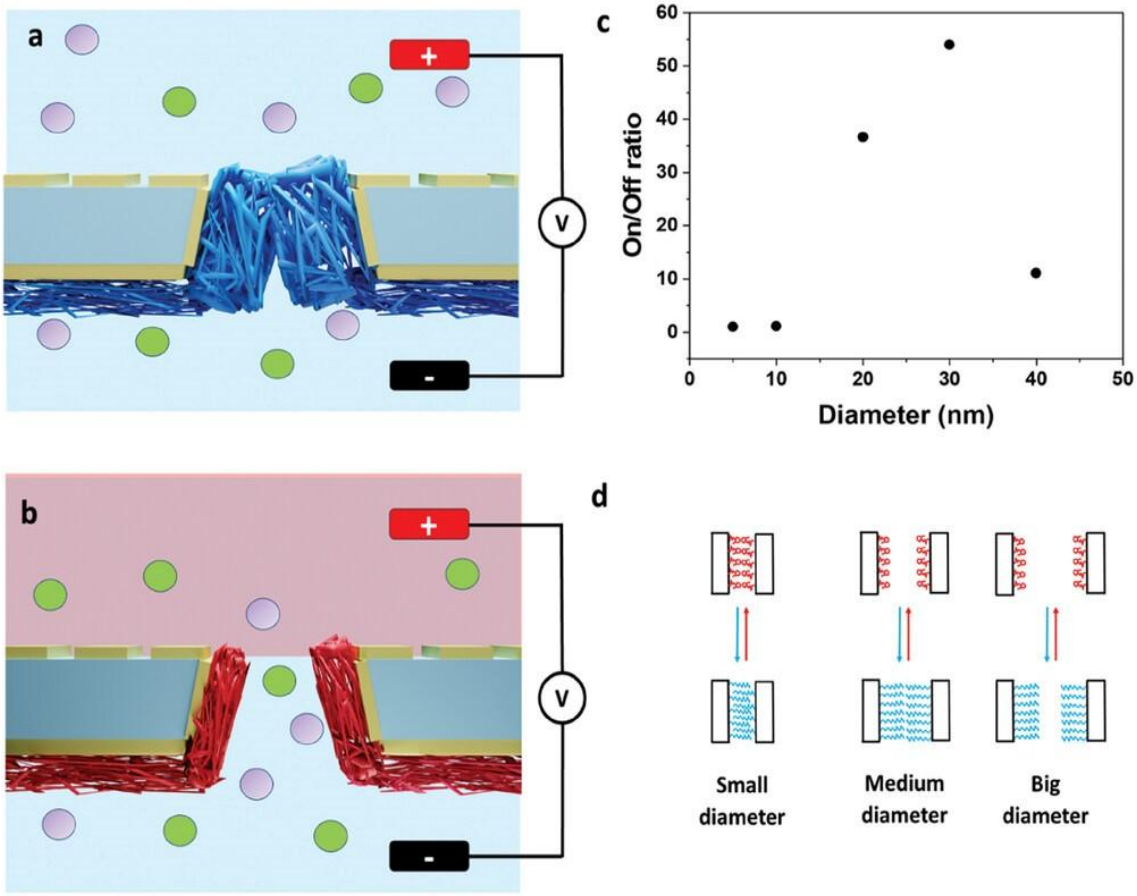

Figure 3.7 Optimization of SiN nanopore size for PNIPAM modification. ***a*** *and* ***b*** *illustration of an individual nanopore coated with PNIPAM (bottom side) and bullseye (top side) with laser off and on, respectively.* ***a*** *with the laser off the temperature inside the pore was lower than the LCST value, hence, the PNIPAM was swelled obstructing the ions flow,* ***b*** *with the laser "on" the temperature inside the pore was increased above the LCST, hence, shrinking the PNIPAM and leading to an increase in the current, (green and purple balls represent potassium and calcium ions in the electrolyte).* ***c*** *schematic illustrations of functionalized nanopores with different diameters.* ***d*** *current On/Off ratio versus different pore diameters after gold deposition.*

A further examination of the impact of pore size on the current On/Off ratio is reported in Figure 3.7c. Below a 30 nm nanopore diameter, the on/off ratio was notably low, attributed to constant pore blockage. This effect was due to the minimal pore size alteration resulting from PNIPAM's thickness change, which prevented pore opening even above the LCST. We hypothesized that a high PNIPAM density may restrict the polymer's conformational flexibility and its ability to shrink. Increasing the pore diameter

to 30 nm increased the On/Off ratio, indicating that at this diameter, and at temperatures surpassing the LCST, PNIPAM could sufficiently undergo conformational changes. This alteration allowed more space for ion passage. Conversely, further enlargement of the pore diameter led to a reduction in the On/Off ratio. In this scenario, even the swollen state of PNIPAM was insufficient to block the pores effectively due to their larger size (as shown in schematic Figure 3.7d). In conclusion, these findings highlight the potential of PNIPAM as an effective material for gating nanopores, with an optimal pore diameter of 30 nm for achieving a high on/off ratio.

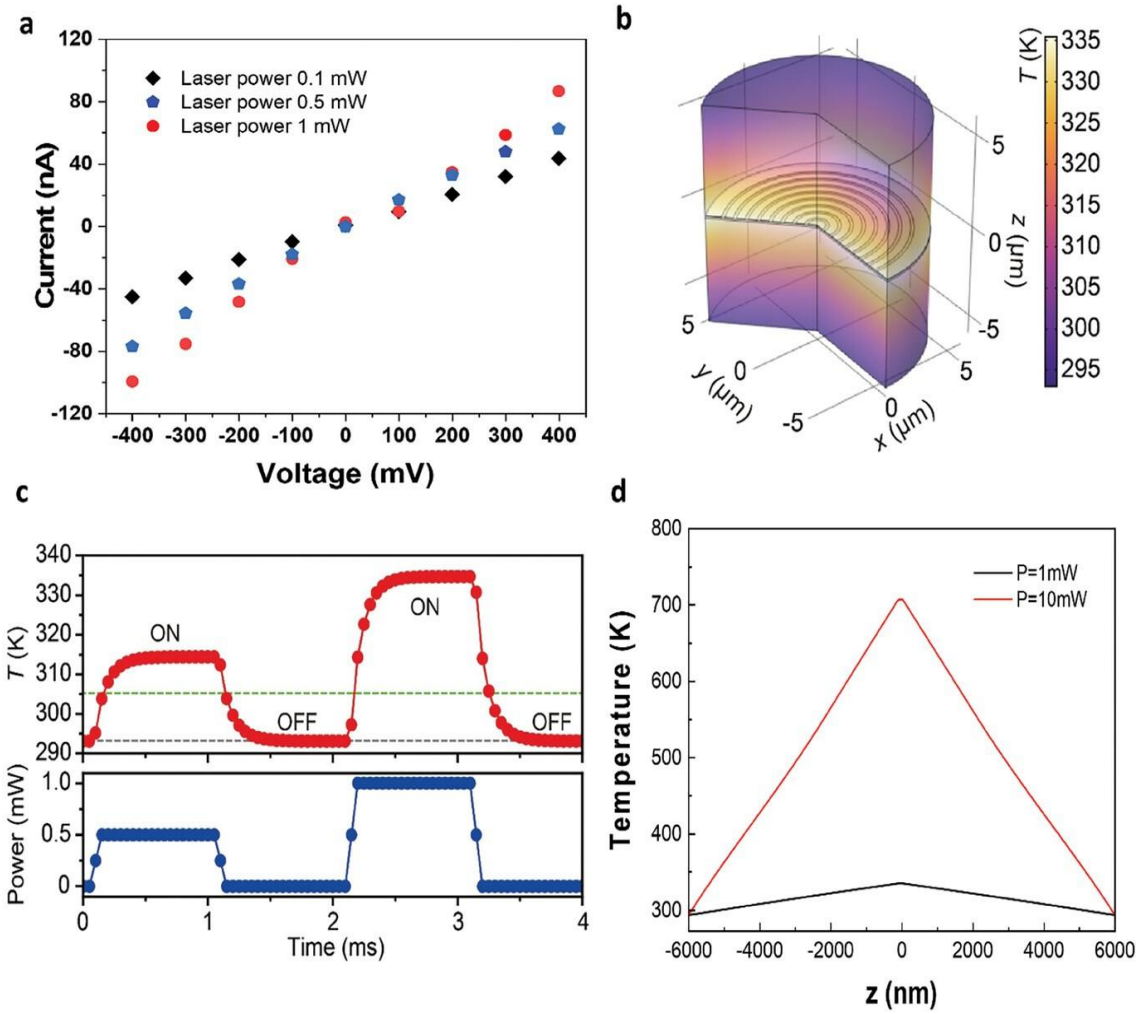

Figure 3.8 Laser heating effect on nanopore. ***a*** *Current-voltage curve of bare nanopore at different laser power irradiation 0, 0.5, and 1 mW in 1 M KCl.* ***b*** *COMSOL modeling of the local temperature in the gold bullseye plasmonic nanopore. Upon illumination with light at 633 nm at 1 mW cm^{-2}. The heat map displays the elevated local temperature at a steady state around the gold pattern.* ***c*** *Temporal response of the temperature at the center of the nanopore, plotted together with the laser power. Green and grey dashed lines denote the threshold temperatures of 32 and 20 °C for switching between the shrunk and extended conformations of the PNIPAM film, respectively.* ***d*** *temperature profile on the z-axis inside the nanopore.*

To achieve fast and possibly highly localized changes of the PNIPAM conformation we harnessed the nanopores with thermoplasmonic structures. In nanophotonics, plasmonic heating has been successfully employed through the utilization of the "bullseye" structure [68]. Figure 3.1d shows an SEM micrograph of the bullseye structure that we fabricated with a nanopore in the center and which we illuminated with a laser at 633 nm to induce the localized plasmonic heating. The goal is to increase the local temperature at the nanopore above the LCST value of PNIPAM to trigger the morphological and hence the opto/thermo gating of the nanopore.

To investigate the temperature changes that can be achieved with this approach, we monitored the conductance change with respect to bullseye illumination, leveraging the temperature-dependent conductivity of potassium chloride (1 M KCl) as an electrolyte, for which an increase in temperature is directly proportional to an increase in conductance. Figure 3.8a reports the current–voltage (*I–V*) curves obtained from a single plasmonic (bullseye) nanopore before the surface functionalization with PNIPAM (bare nanopore). As expected, the conductance of the nanopore depends on the illumination intensity (laser power). We use these measurements to obtain an estimation of the temperature inside the nanopore and apply COMSOL modeling to numerically calculate the expected temperature inside the nanopore for the different laser excitation powers. For the purposes of these simulations, we assumed that 100% of the incident light power was absorbed by the nanopore membrane, specifically the gold components of the bullseye structure. This assumption simplified the modeling of time-dependent energy dissipation and local temperature evolution around the nanopore. The powers applied (0.5 and 1 mW) are those typically used in this configuration and were fully converted into thermal energy for the calculations. For the thermal simulations, the gold bullseye was defined as the heat-generating region, with the absorbed laser power applied as the thermal input. Heat was subsequently dissipated from the gold structure through the surrounding SiN membrane and aqueous electrolyte, which were treated as thermal conducting domains. The model was solved under steady-state conditions, with the system initially referenced to room temperature. Without excitation, the system is at room temperature, while for illumination intensities of 0.5 and 1 mW cm^{-2}, the simulations show temperatures inside the nanopore of 315 and 334.7 K, respectively (see Figure 3.8b,c). The temperature profile inside the nanopore on the z-axis is shown in Figure 3.8d. We note that no substantial conductance change was observed in a control experiment illuminating a nanopore without a bullseye

structure at 1 mW cm^{-2}. This evidences the key role of the thermoplasmonic effect in regulating the temperature at the nanopore with illumination intensities that are sufficiently low to avoid damage of the pore or the PNIPAM film by the laser.

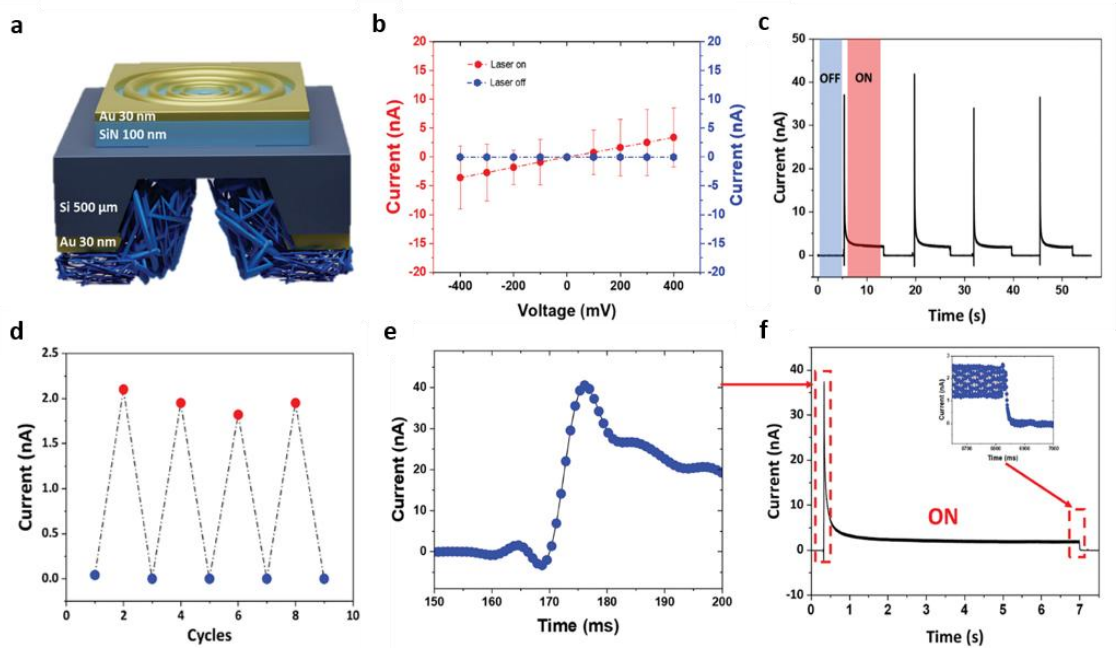

Figure 3.9 Demonstration of repeatable on-off state switch of single nanopore coated with PNIPAM. ***a*** *illustration of the single nanopore coated with PNIPAM.* ***b*** *Current–voltage characteristics of a nanopore decorated with PNIPAM with the laser in the "off state" and "on state" in 10 mM KCl and 1 mW cm^{-2} laser power.* ***c*** *current versus time with cycling where the laser was switched on "red zone" and off "blue zone" at 1 V.* ***d*** *different cycles showing the stability of the pore between switching on and off. e,****f*** *one cycle enlarged showing the respond time of the polymer configuration change.*

Figure 3.9a shows and illustrates the device used in this set of experiments, where a single nanopore coated with PNIPAM was employed. Figure 3.9b shows the *I–V* curves in the presence and absence of laser-induced heating at 1 mW cm^{-2}, respectively. With the laser off, the internal nanopore temperature was below the LCST, with a swelled PNIPAM state that blocks the pore ("Off state"). Under illumination, the nanopore temperature is above LCST, and the shrunk PNIPAM conformation results in an opening of the nanopore channel, signifying the "On state".

Additionally, Figure 3.10a illustrates the current increase in the functionalized nanopore compared to the unfunctionalized nanopore (control sample). As shown, the current increase in the functionalized nanopore is significantly greater than that in the control sample, likely due to the low ionic concentration of the 10 mM electrolyte. To minimize the impact of temperature-induced ionic current increase and to enhance the gating effect of PNIPAM, we utilized a 10 mM KCl solution instead of a 1 M KCl

solution. Key features of the switching performance are the stability over several cycles, and the time scales at which the temperature and PNIPAM conformational changes are occurring. The nanopore's electrical response and stability over time for several On and Off switching events at a fixed bias is reported in Figure 3.9c,d. Each switching-on event (laser power on) induces a spike in conductivity that decreases exponentially to around 2nA (Figure 3.10b, fitting of the decay and evaluation of the decay constants). We attribute this behavior to the capacitive discharging of the charges that accumulated at both sides of the blocked nanopore, and that equilibrate upon pore opening. When the laser is turned off, the current falls to near zero in a few ms, evidencing the blockage of the nanopore. To evaluate the response time for the pore opening and closing processes, we analyze the rise and fall times of the current with the 10% and 90% threshold criteria and obtain 3 and 4 ms, respectively (Figure 3.9e). We note that these values represent upper limits to the conformational opening and closing process since they are derived from the current change that is also impacted by the properties of the electrolyte. Moreover, the fast thermoplasmonic opening/closing behavior of the nanopores was also corroborated by our simulations of the temperature within the nanopore, that rises above the LCST in less than 0.5 ms upon illumination (Figure 3.8b). With switching times of the order of a few ms, the operation of thermoplasmonic nanopore devices with frequencies up to almost 1 kHz should be possible. We note that the impact of the associated increase and decrease in the local viscosity on the nanopore conductance is anticipated as marginal compared with the giant On/Off ratio observed [69].

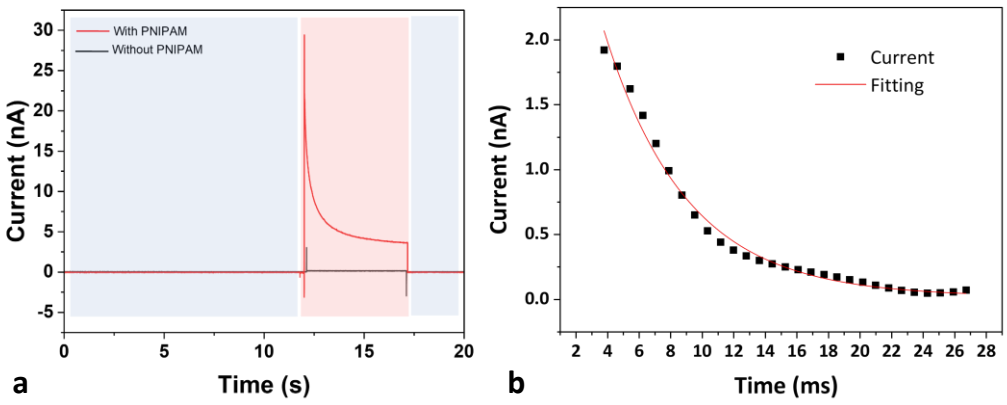

Figure 3.10 Time-dependent ion current trajectory. ***a*** *Current vs. time under laser illumination: laser on (red zone) and laser off (blue zone) at 1V in 10 mM KCl solution of functionalized nanopore (red line) and unfunctionalized nanopore (black line),* ***b*** *Enlarged current vs time.*

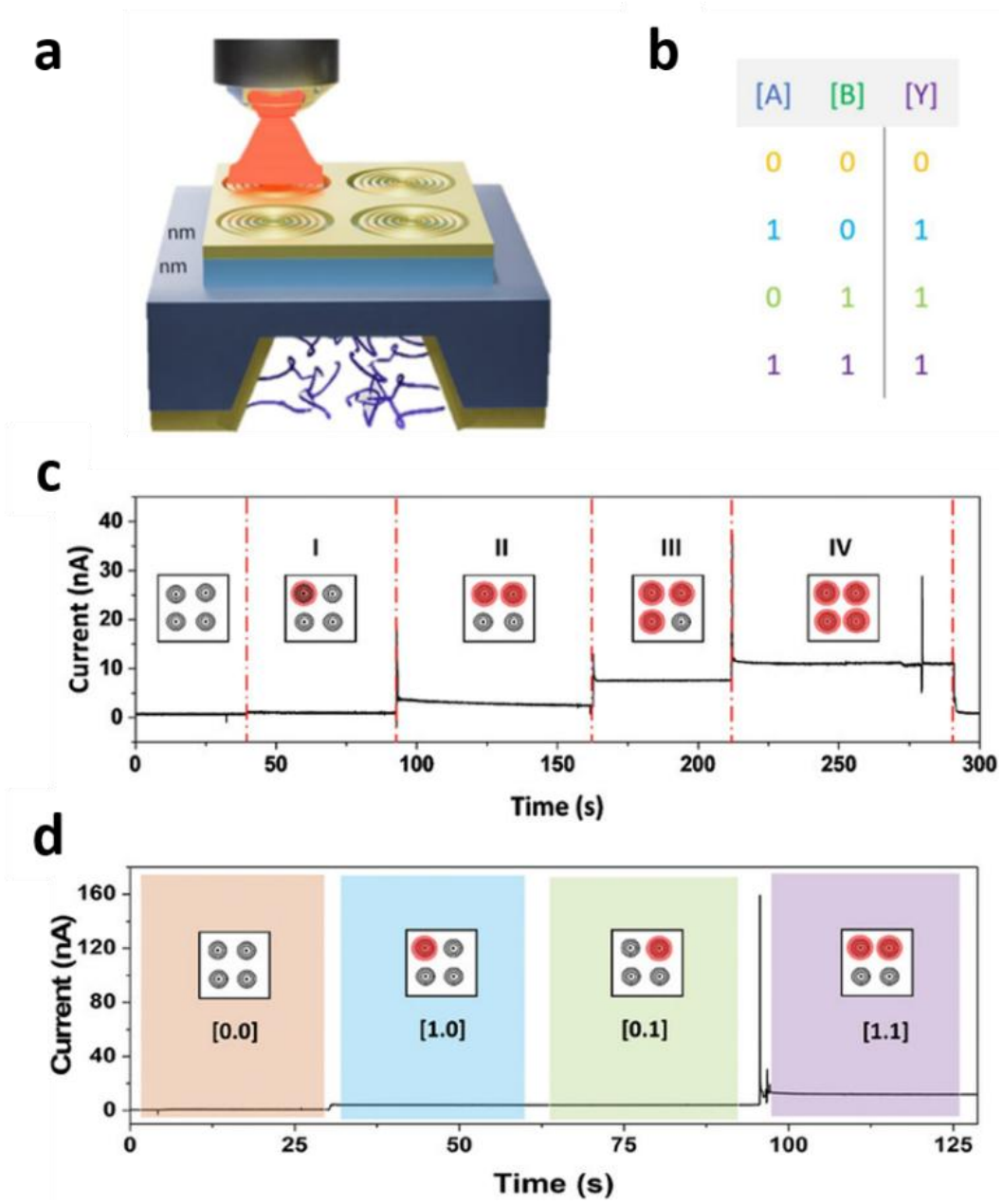

Figure 3.11 Multi-level ion current based on PNIPAM modified nanopore array. ***a*** *illustration of nanopore array, each nanopore is surrounded by bullseye that will lead to a selective heating of nanopores by focusing the laser beam on the desired structure which then leads to a selective opening of nanopores;* ***b*** *represent the OR logic and the current level shown in panel d;* ***c*** *current versus time shows an increase in the current due to opening different pores one after another which leads to an increase in the current and then switching them off one after another which led to a decrease in the current, each roman number represents the number of pores opened;* ***d*** *current from the nanopores array and different following logic gates "OR gate", shows that by modulating two pores with a laser leads to closing nanopore, no current to represent the "off state" of the logic gate then switching on the laser so opening the pore leading to an "on state" logic gate.*

So far, we have discussed the opto/thermal gating of the conductance of a single nanopore. However, this gating concept can be extended to nanopore arrays, where

individual pores can be switched separately or in combination. The laser spot size (diffraction-limited to below 1 μm) and the bullseye pattern (10 μm diameter in Figure 3.1b) define the spatial resolution at which individual nanopores can be addressed. Thus, nanopores in an array with a 12 μm pitch can be controlled on millisecond timescales, opening possibilities for cascaded logic gate ionic computing using our thermoplasmonic nanopores. Cascadability, which is critical for complex logic gate operations, can be achieved by spatially multiplexing optical control across nanopores, where the output of one nanopore system can be fed as input to another in parallel or in series.

Figure 3.11a displays the design of such an array on a chip, where each nanopore is surrounded by a gold bullseye pattern that allows for selective and local thermal heating. Multiple pores can be actuated simultaneously by adjusting the laser spot size to illuminate several adjacent pores as in our proof-of-concept demonstration, or via more sophisticated laser beam multiplexing that could allow to address certain sets of nanopores at will. Fast optical addressing of the nanopores could be achieved by galvanic optical mirrors as in commercial confocal scanning microscopes, for example. In the following, we show a proof-of-concept demonstration of the "OR" logic (Figure 3.11b) gating based on the optical microscope setup in our lab. Here we adjust the laser spot size by focusing and defocusing the microscope optics and address specific chip areas by the movable microscope stage. Figure 3.11c captures the resulting electrical response as multiple nanopores are opto-thermally modulated. The illumination of a nanopore by the laser results in an increase in current. By enlarging the laser spot size, one, then two, three, and four pores can be activated simultaneously, which leads to current values of 2, 5, 8, and 10 nA, respectively. Here the conductance of the individual nanopores varies between 2 and 3 nA due to small differences in nanopore diameter. Addressing pairs of adjacent nanopores is possible by moving the enlarged laser spot with respect to the pore array. With this control on the switching of multiple nanopores, we can achieve optical gating in the realm of logic gate ionic computing. Building a logic circuit with multiple nanopores on the same chip represents a paradigm shift, as current technology is only able to measure single logic gates independently. Figure 3.11b,d represent the operational mechanism of the "OR" logic gate using two nanopores (A and B) that can be switched on and off separately or together. The conductance of this nanopore system is reported in Figure 3.11d. With no laser illumination ([0.0]), both nanopores remain closed, yielding

no current flow and representing a binary “0” for both inputs. With the focus of the laser on nanopore A ([1.0]), a distinct increase in the current corresponds to a binary ‘1’ for input A, while the other nanopore (input **b** maintains a binary ‘0’. When the laser targets the second nanopore ([0.1]), input A reverts to ‘0’ and input B transitions to ‘1’. To obtain the state ([1.1]), the laser illuminates both pores, which leads to a larger current for the individual pores, reflecting a binary ‘1’ for both inputs A and B. This arrangement demonstrates a current-based execution of logical operations, confirming the viability of the nanopores array to be orchestrated to perform logical operations. While the current setup demonstrates an ‘OR’ logic gate, we are actively exploring methods to achieve more universal gate functions, such as NAND and NOR, through ensemble control of nanopores. Achieving these universal gates requires implementing a NOT gate for negation operations. This could be realized by functionalizing the nanopores with photo-sensitive materials, such as spiropyran, which can close upon light illumination [47] By combining thermo-responsive and photo-responsive materials, we could unlock more complex logical operations in ionic computing, paving the way for advanced computational architectures.

3.3 Conclusion

In conclusion, this study represents a significant step forward in the field of nanofluidics, illustrating the successful integration of stimuli-responsive molecules, specifically PNIPAM, into solid-state nanopores alongside a plasmonic structure for opto/thermal gating. This innovative approach overcomes the limitations of traditional temperature-dependent gating methods that rely on external heat sources. By employing thermoplasmonics, this work enabled a selective activation of individual nanopores. This method was validated through ionic conductivity measurements, demonstrating the ability to selectively control nanopores with high precision and On/Off efficiency at a micrometer scale. The high speed in the thermal response (in the millisecond range) enables unprecedented gating efficiency. Furthermore, the introduction of multistage current switching capabilities, exhibiting low, medium, and high (i.e., “0,” “1,” “2” and “3”) quaternary levels of ion conductance, marks a breakthrough in the field. This stable and robust multistage switching could pave the way for multivalued logical gating, managed optically, thereby enhancing the versatility and functionality of nanofluidic devices. Device reproducibility was limited primarily by the variability of PNIPAM

modification and nanopore fabrication. Approximately 20 chips were fabricated, of which only a small fraction showed clear and repeatable optical switching. The functional devices nevertheless exhibited stable switching over hundreds of cycles (Figure 3.9c–d), indicating good short-term operational stability once the polymer gate was properly formed. This research significantly contributes to the evolution of smart nanofluidic systems, broadening their applicability in areas like biosensing and targeted drug delivery. The ability to control nanopores with such enhanced precision and efficiency holds great promise for future innovations in various scientific and medical fields.

Chapter 4 Electrically Gated Ion Transportation of MoS_2/SiN Nanochannels

Ion transport through nanochannels plays a crucial role in a wide range of applications, including drug delivery, biosensing, desalination, and energy harvesting. Among the various systems studied, nanochannels composed of two-dimensional (2D) materials such as MoS_2 and graphene have recently received significant attention. Their atomic thickness allows the creation of sub-nanometer channels, which provide a powerful platform for exploring fundamental phenomena such as quantum friction, ion adhesion, orientational conduction, and DNA translocation [70–73]. Despite these advantages, the fabrication of multi-stacked 2D material structures remains a challenging task, and the development of simpler device architectures would greatly facilitate the study of nanofluidic processes in this unique family of devices.

The strong confinement effect characteristic of 2D-material-based nanochannels results in distinctive ion transport properties. These properties can be modulated through adjustments in interlayer spacing, surface chemistry, or material composition [9,51]. In the context of single-molecule sensing, MoS_2 offers particular advantages compared with graphene. Its hydrophilic surface reduces unwanted interactions with DNA [73–75], while intrinsic sulfur vacancies on the MoS_2 surface provide sites that can selectively slow down or capture proteins containing free thiol groups. This capability highlights MoS_2's potential in advanced protein sensing applications [76,77]. Among emerging nanofluidic device concepts, the ionic transistor stands out as a promising building block for ion-based logic computing. These devices operate by electrically modulating the surface charge of nanopores or nanochannels to control ion transport [2,10,13,25,26,78–83]. Two-dimensional materials such as MoS_2 are especially promising for this purpose, as their carrier type can be efficiently tuned through chemical modification or electrostatic gating [84–89]. However, most existing designs rely on symmetric, suspended 2D

membranes that are mechanically fragile and require complex fabrication procedure, limiting reproducibility and scalability.

To address these limitations, we developed a hybrid nanochannel platform that integrates a mechanically robust MoS_2 flake with a freestanding silicon nitride (SiN) membrane. Unlike conventional 2D material stacks [18,27,30], the device is fabricated by transferring a thick MoS_2 flake onto a FIB-milled trench in SiN, forming an asymmetric channel supported on one side by SiN and electronically active on the other. This architecture provides mechanical stability while preserving the tunable electronic properties of MoS_2 and, crucially, enables selective electrical gating of only the MoS_2 wall. This selective gating produces a programmable charge asymmetry within the channel, an effect that is not accessible in symmetric 2D nanopores. As a result, the platform allows controlled modulation of ion transport through spatially localized gating rather than relying on geometric asymmetry or chemical patterning.

In this chapter, we present a comprehensive study of ion transport in electrically gated MoS_2/SiN nanochannels. We systematically examined how gate voltage, ion concentration, and pH influence surface charge and ion conductance, and we demonstrate the platform's functionality in two applied contexts: osmotic energy generation and single-protein translocation sensing. Our results reveal gate-dependent rectification behavior, competitive osmotic power densities, and prolonged protein dwell times, highlighting the versatility of this hybrid platform for both energy-harvesting and biosensing applications. Through these experiments, we elucidate possible mechanisms of ion translocation in MoS_2/SiN nanochannels and discuss their implications for the design of nanofluidic devices. Overall, the proposed structure design and ion current tuning mechanism contribute to the expanding knowledge of nanoscale ion transport and highlight the promise of electrically tunable MoS_2/SiN nanochannels as a platform for future advances in nanotechnology and biomedicine.

4.1 Device Fabrication and Characterization

Freestanding Si_3N_4 membrane chips were fabricated using the same standard MEMS procedure as described in last chapter, except the size of the membrane are chosen to be ~50 μm^2 which has better robustness compare with larger size membrane, to avoid possible broken with integrated top layer MoS_2 flake.

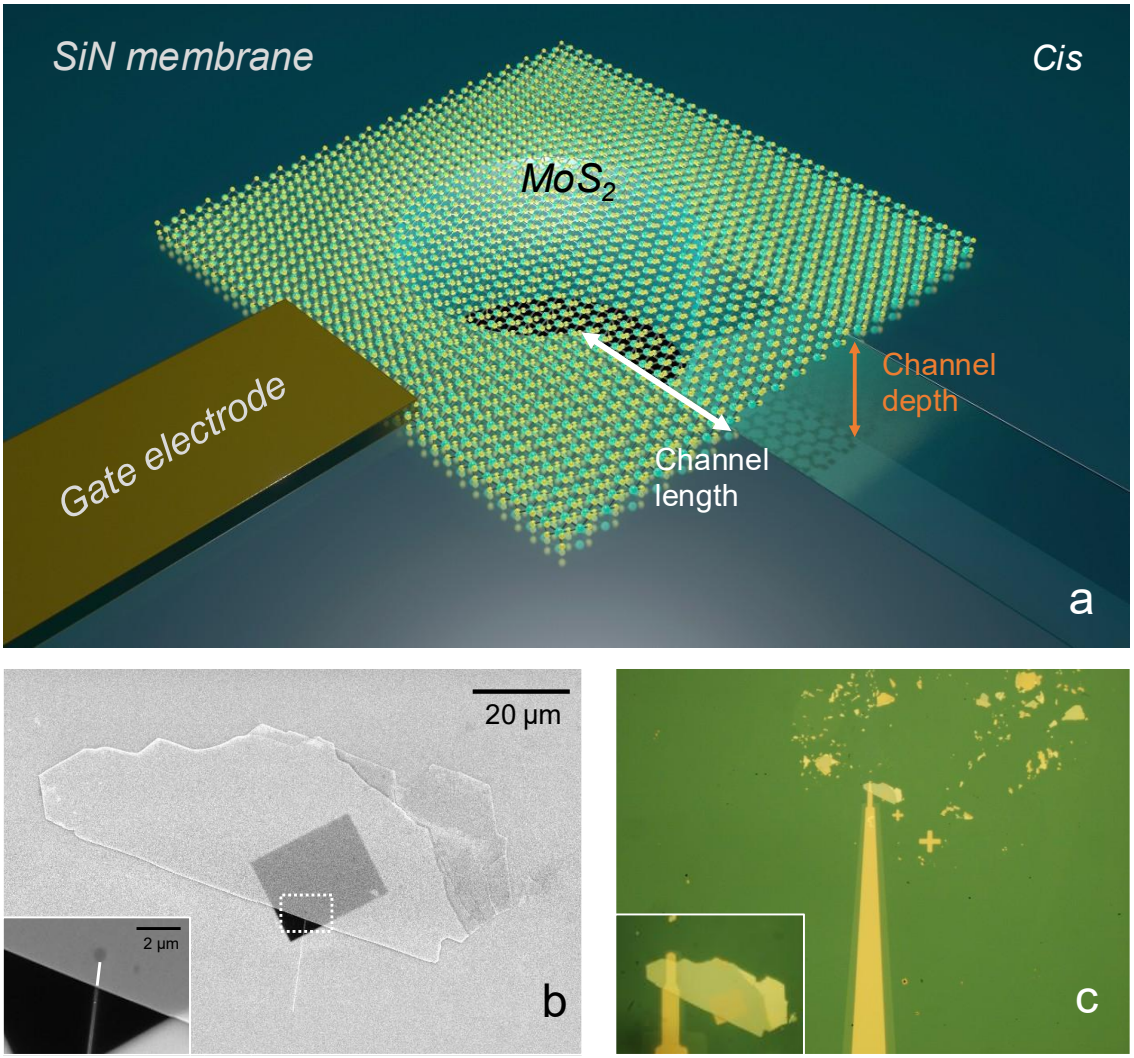

Figure 4.1 Device design. ***a*** *Illustration of nanochannel devices formed by MoS_2 flake and SiN membrane with a nanopore and nano-slit. The length, width, and height of the nanochannel is around 1μm, 100 nm, and 10 nm respectively;* ***b*** *SEM image of nanochannel device just after the transfer of MoS_2; the inset shows the magnification image of white dash line framed region, and the solid white line in the inset image;* ***c*** *Optical image of nanochannel device after the Au electrode deposition.*

4.1.1 Nanostructure fabrication

Here, we propose a novel structure which can be fabricated by a simpler process compared with previously reported sandwiched 2D material stacks structures [30]. The nanopore and the nano-slit(s) are directly milled by focused ion beam (FIB) on suspended SiN membrane with 30 kV acceleration voltage and 18 pA current, after which a thick layer of MoS_2 is transferred on top of the nano-slit to form a nanochannel comprised by SiN and MoS_2 surface, as shown in Figure 4.1a. The MoS_2 flake is typically made thicker than 50 nm to prevent sagging that could obstruct the channel, while still preserving surface charge tunability, since electrons primarily accumulate near the surface. The

nanochannel depth is primarily determined by the ion-beam dwell time during milling. In our case, it typically ranges from 5 to 20 nm, as confirmed by AFM measurements on multichannel samples (Figure 4.2).

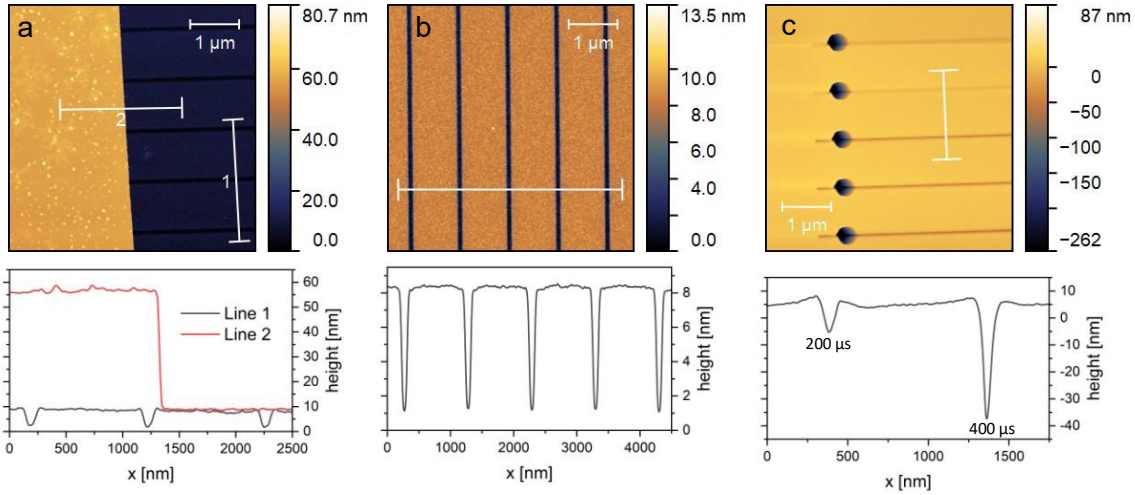

Figure 4.2 AFM data of MoS_2/SiN multichannel devices. ***a*** *Thick MoS_2 layers covered multichannel;* ***b*** *As fabricated multichannel by FIB with 200 µs dwell time under 18 pA;* ***c*** *Channels fabricated by FIB with different dwell time under 18 pA.*

4.1.2 Two-dimensional material transfer

There are mainly two ways to prepare MoS_2 flakes, physically by means of mechanical exfoliation (cleave the original crystal) or chemically (controlled chemical reaction on substrate by CVD/CVT). These two techniques result in different surface charge characteristics [90–92]. On the fresh cleaved MoS_2 flakes, the surface is near intrinsic because of the smooth surface, and the electrons will gradually accumulate on the surface because of the slow desulfurization in the air, which induces a negatively charged MoS_2 surface.

On the other hand, the CVD/CVT grown MoS_2 flakes are always negatively charged because of the dangling bonds generated during the chemical reaction process [92]. MoS_2 flakes prepared via chemical processes can be suspended in proper solvents and easily deposited on solid-state substrates [93] but they typically present a high level of contamination making them not suitable for the scope of this work. Therefore, here, we used exfoliated MoS_2 flakes as a top layer to form the nanochannels (Figure 4.1b). The MoS_2 flakes were exfoliated using well established scotch tape methods onto a 300 nm SiO_2 substrate. By using a standard optical microscope, it is possible to quickly obtain a first check on the quality of the transferred flakes.

A polycarbonate (PC) thin film on top of PDMS dome supported by a transparent cover slide is used to transfer the selected MoS_2 flake from SiO_2 substrate to SiN membrane which has a nanopore connect with a shallow nano-slit (Figure 4.1a) [94,95]. The PC thin film was prepared by a dip-coating method. First, a PC solution was prepared by dissolving polycarbonate in chloroform (10% weight ratio). The solution was then deposited onto a clean glass slide using a drop-casting method. A second glass slide was immediately positioned parallel above the coated slide and gently pressed with finger pressure to eliminate air bubbles between the two surfaces. Subsequently, the upper slide was rapidly removed through a horizontal sliding motion, leaving a thin, uniform layer of PC solution on the lower substrate. The chloroform solvent was allowed to evaporate under ambient conditions for 1 minute, resulting in the formation of an ultrathin, uniform PC film. This free-standing PC film, when combined with perforated double-sided adhesive tape mounted on a PDMS stamp, served as an effective transfer medium for 2D materials in subsequent processing steps [96].

4.1.3 Gating electrode fabrication

The Ti/Au electrode (Figure 4.1c) was fabricated using two photolithography steps. First, the Au electrode region pattern was defined using the resists LOR3B/S1805 spin coated as a double layer to form undercut feature. A 5 nm Ti adhesion layer followed by a 30 nm Au layer was deposited on developed regions by using electron beam evaporation, followed by lift-off in PG remover for 5 min.

A second lithography process using a larger line-width pattern to isolate the Au electrode was performed using a similar process (spin coating photoresist, mask-aligner exposure, evaporation of isolated material and lift-off). As shown in Figure 4.1c, the tip of the Au electrode contacts the MoS_2 flake, while the pad is positioned outside the membrane for electrical characterization of ionic transistor behavior.

4.1.4 Electrochemical measurement configuration

All electrochemical measurements, except for gating, were carried out using a Nanopore Reader (100 kHz) and PMMA flow cells from Elements srl. Prior to each measurement, the nanochannel device was immersed in an ethanol–water (1:1) solution for 10 minutes to ensure proper wetting. Two PDMS blocks with central openings were placed on both sides of the device to facilitate mounting in the cell without leakage. After introducing 70 μL of electrolyte into each reservoir, a constant voltage was applied for 10 s in 100 mV

(or, when required, 20 mV) increments from V– to V+. For osmotic power measurements, triangular voltage sweeps from –500 mV to 500 mV were performed at 10 mV/s to determine the intercept value.

For gating experiments, a Keithley 2612B connected to a probe station was used to apply the three-terminal configuration. In this setup, the source–drain potential was swept from –500 mV to 500 mV over 100 s (10 mV/s).

4.2 Tunable Ion Transportation via External Bias

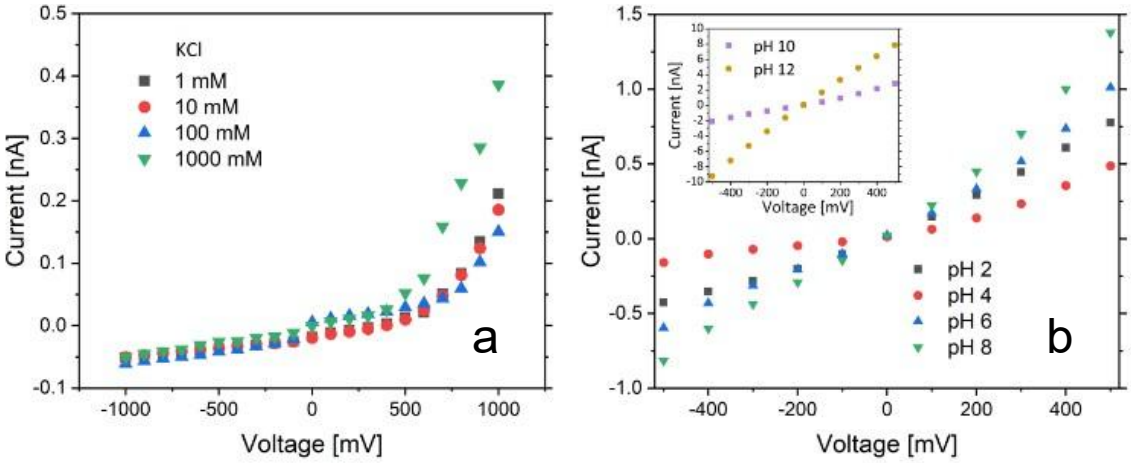

Figure 4.3 Ion transport of nanochannel. ***a*** *Ion current across nanochannel with different KCl concentrations under pH 7.4 before cleaning process and* ***b*** *Ion current of 10 mM KCl across nanochannel with different pH after cleaning process.*

The first characterization of the platform was done by measuring the ionic current with different concentrations of KCl. As shown in Figure 4.3, The conductance of the nanochannel did not increase linearly when the concentration of KCl electrolyte increased from 1 mM to 1000 mM. This non-linear behavior could be attributed to mechanisms such as ionic coulomb blockade as described for sub-nm monolayer MoS_2 nanopore or the predominance of counterions transport [97,98]. While the ion current is very small due to the limited channel height and because of potential hydrocarbon contamination, we observed an ionic rectification with a rectification ratio up to 10 for 1M KCl. In order to verify these first results, we repeated the measurements after a cleaning procedure on the sample. The cleaning process was conducted by applying a potential ranging from –100 mV to 100 mV with an alternating current scan overnight. The alternating electric field prompted ions to accumulate at the nanochannel entrance and repeatedly penetrate the contaminant barrier. Through multiple cycles, the blockages were gradually removed,

thereby restoring the ion transport capacity of the channel (Figure 4.4) [99]. After the cleaning procedure, a larger and more linear ion current was detected (Figure 4.5a). It indicates more symmetric surface charge distribution after the electrolyte cleaning process, as well as the minimal geometric asymmetry.

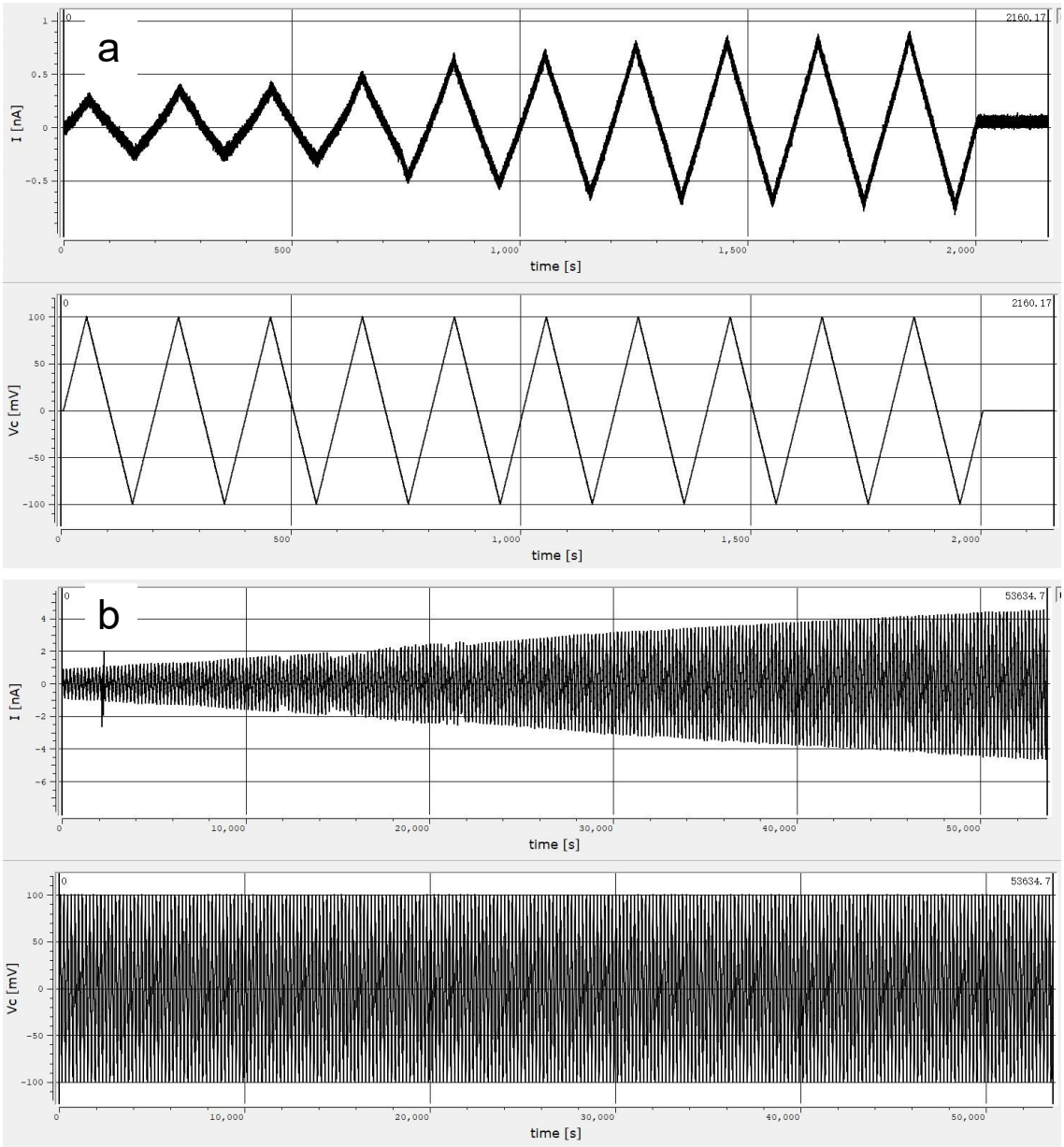

Figure 4.4 Unclogging of the nanochannel by large number of low voltage cycling scan. ***a*** *first 10 scan,* ***b*** *overnight scan.*

4.2.1 Estimate the surface charge density

In order to study the change of surface charge density of the nanochannel system towards ion current flow, we measured the ion current with a different pH of 10 mM KCl. Figure

4.3b shows how the ion current conductance is significantly affected by the pH value of the electrolyte after the cleaning process.

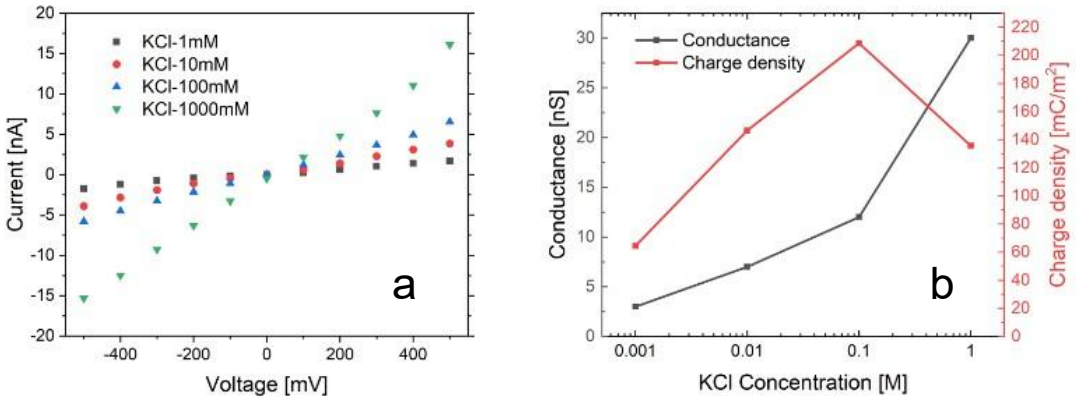

Figure 4.5 ***a*** *Ion current of single MoS_2/SiN nanochannel under different KCl concentrations after the cleaning process.* ***b*** *The calculated conductance based on* ***a*** *and the calculated charge density based on conductance and formula (4.1).*

As the pH increases, the current increases, suggesting that the nanochannel surface becomes more negatively charged, attracting the positively charged ions. The minimal ion current value occurred at pH 4 attributable to the effective isoelectric point of the MoS_2/SiN channel, consistent with published isoelectric point data of MoS_2 and SiN [100,101]. With a pH increased from 10 to 12, the rectification direction changed. This phenomenon can be attributed to the distinct deprotonation behaviors of the two channel walls. While both MoS_2 and SiN remain negatively charged in this alkaline range, their surface charge densities evolve differently: SiN, with an isoelectric point near pH 5–6, is already strongly deprotonated at pH 10, whereas MoS_2 continues to gain substantial negative charge between pH 10 and pH 12. This shift in the relative surface charge asymmetry between the MoS_2 and SiN walls alters the spatial distribution of ion enrichment and depletion zones under bias, thereby inverting the rectification direction without requiring a reversal of absolute charge polarity. The pH-dependent behavior highlights the importance of surface charge in controlling ion transport through the nanochannel [102]. The surface charge density of the MoS_2/SiN nanochannel system can be estimated by ionic conductance measurements, as used for hBN nanotube system [14]:

$$G = 2e^2\mu C_s\frac{A}{L} + e\mu\frac{C}{L}|\sigma|(1+\alpha) \tag{4.1}$$

Where e is the electron charge, C_s is the ion number density of the electrolyte, A and C are, respectively, the area and perimeter of the nanochannel cross-section, L is the

length of the channel, μ is the mean ion mobility of the electrolyte in s/Kg, σ is the surface charge density, and α which account for the electro-osmotic conductance contribution (here this value is around 1).

As shown in Figure 4.5b, the surface charge density of our MoS_2/SiN nanochannel system is around 100 mC/m^2, much higher than the measured surface charge density of SiN nanopore (~15 mC/m^2) [101], indicating that the MoS_2 surface plays a more important role in controlling the ion current of our hybrid nanochannel system.

4.2.2 Tune the surface charge density via bias voltage

Given that the ion current rectification (ICR) observed in the MoS_2/SiN nanochannel may result from an unbalanced surface charge distribution between the two channel walls, we probed ion transport as a function of the MoS_2 surface charge by applying a gate potential through a top electrode. Figure 4.6a shows the electrical measurement setup for the transistor-like configuration, where we used two channels from a Keithley 2612B source meter. As shown in Figure 4.6b, the channel conductance increases with decreasing gate voltage down to -500 mV, which can be attributed to an elevated counter-cation concentration driven by the enhanced negative surface charge on the nanochannel walls. As mentioned in last section (4.2.1), the surface charge of MoS_2 accounts for a larger proportion of the hybrid system, and the charge of the MoS_2 is mainly constrained on the surface [103]. The negative surface charge density enhancement under negative gating bias has been shown in many previous KPFM study papers [104–106]. The surface charge reversal has also been predicted via Density Functional Theory (DFT) study by Mortier et. al [107] which could be the mechanism that lies down under our observation, where with applied positive gate voltage we observed a conductance enhancement in the other direction.

These ambipolar characteristics indicate that the nanochannel surface is nearly electrically neutral at zero gate voltage, and the application of either positive or negative gate voltages increases the accumulation of counter-ions, thereby increasing conductance which has also been proved in CNT base ionic transistor system [13,108]. The I–V curves further reveal a switch in ICR behavior depending on the direction of the applied bias. At zero gate voltage, the current is suppressed under positive transmembrane bias, a trend that persists with increasing positive gate voltage. However, when negative gate voltage

is applied, the rectification behavior reverses — conductance under negative trans-membrane bias decreases relative to that under positive bias.

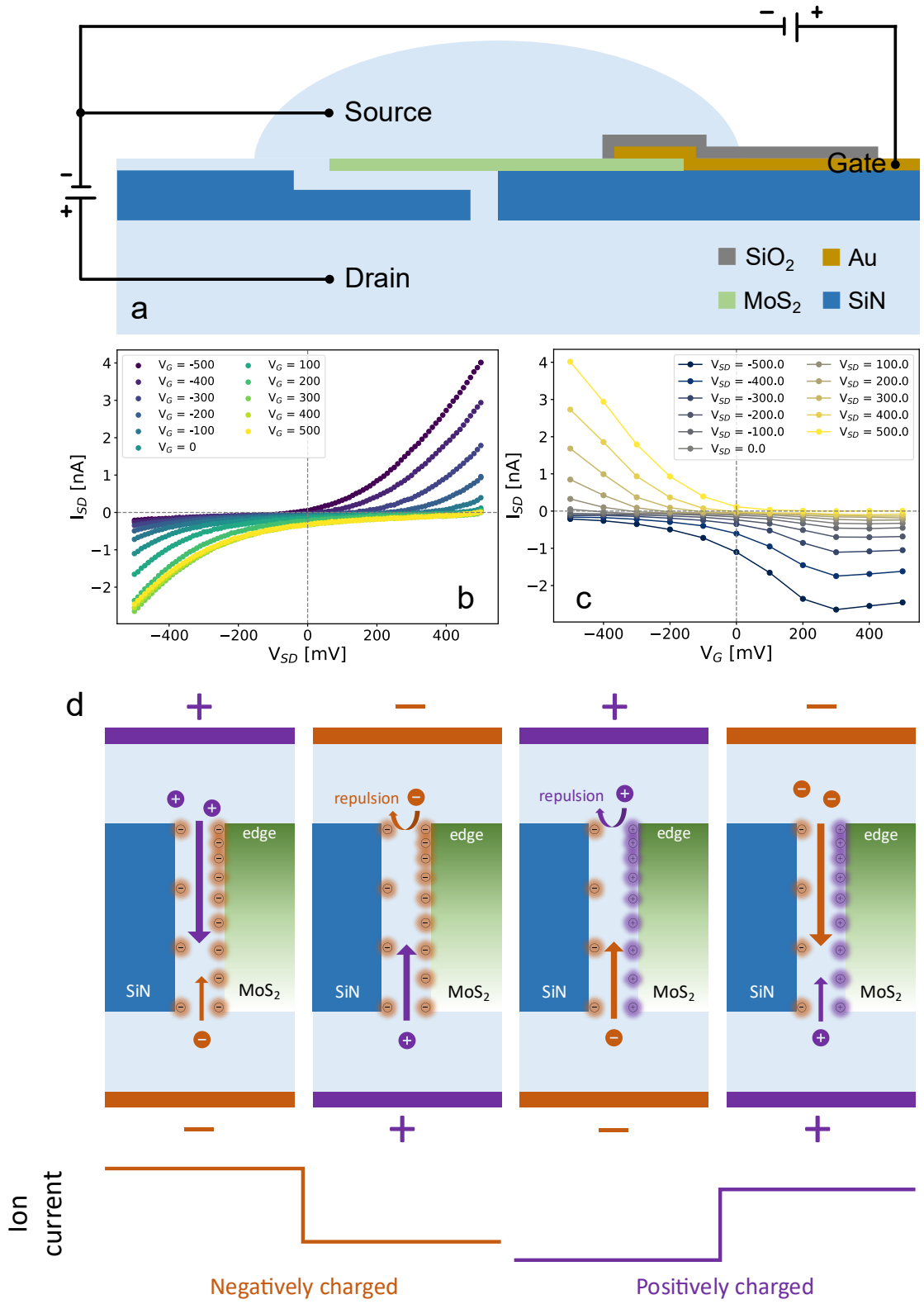

Figure 4.6 Electrically tunable ion transport of MoS_2/SiN nanochannel. ***a*** *Illustration of measurement configuration;* ***(b,c)*** *Ion current of nanochannel under different gate bias and transmembrane voltage "mV" in 10 mM KCl.* ***d*** *Illustration of ion rectification mechanism for the nanochannel.*

Considering the indistinctive ion rectification observed in our nanochannel system without an applied gate bias (particularly after voltage-scan cleaning process), the channel geometry and the surface charge distribution can be considered symmetric. The pronounced ion rectification emerges clearly after applying an external gate bias to the MoS_2 flake, which we attribute to the accumulation of surface charge near the channel edge under small gating bias, an effect consistent with prior microwave impedance microscopy (MIM) characterization on MoS_2 transistor [109]. As illustrated in Figure 4.6d, under a negative gate bias the surface of the MoS_2 becomes more negatively charged, facilitating cations transport enter from the MoS_2 edge side of the channel while impeding anion passage if the transmembrane potential is oriented inversely. The opposite side of the channel exhibits lower ion-selectivity due to its weaker surface charge density. With positive charge accumulation, the anions are favored from MoS_2 edge side while the cations are repelled, creating a bias-dependent asymmetry in ionic current. Furthermore, the non-zero ion current recorded at V_{sd}= 0V under gate bias can be explained by a gate induced built-in potential across the membrane, arising from modulated surface charge asymmetry, which drives ions through the nanochannel in the absence of transmembrane voltage. Similar phenomena have been reported in previous study on ZnO/SiN bilayer nanopores [110] and CNT ionic transistor [13]. Figure 4.6c displayed the gate-dependent ionic current characteristics of our ionic transistor, where an asymmetry can be observed between the response under positive and negative transmembrane potential V_{SD}. For negative V_{SD}, the ion current quickly saturates at around 300 mV while for positive V_{SD} the I_{SD} increases monotonically. This asymmetric behavior could be attributed to the asymmetric of the MoS_2 surface area on cis or trans reservoir, while the surface charge of the smaller area reaches the limited surface charge density faster.

4.3 Scalable Osmotic Power

The high surface charge value further shed light on energy harvesting from salinity gradients. Several recent studies, in fact, demonstrated how it is possible to generate energy from the osmotic process in nanopores / nanochannels using the buffers at the cis/trans sides with two significantly different concentrations [78,110–115]. Here, we first measured the response of our single nanochannel platform using 10X PBS buffer solution (1.37 M NaCl) in both side reservoirs (Cis/Trans) obtaining almost zero ion current without applying any external voltage. On the contrary, replacing the electrolyte

in the trans reservoir to 1X PBS (0.137 M NaCl) we immediately got a positive ion current. By scanning the external potential, we can get IV curves from different configurations as shown in Figure 4.7a. From these data we can calculate the power of our osmotic generator to be ~18 pW (calculated as $P = {V_{osm}}^2 G$, where $V_{osm} = V_{intecept} - V_{redox}$ is the effective osmotic potential and G is the conductance [116]). The redox voltage, V_{redox} is here set to -61.7 mV, as measured from the open voltage of 1000 nm diameter SiN nanopore under the same saline condition (Figure 4.7b) [110].

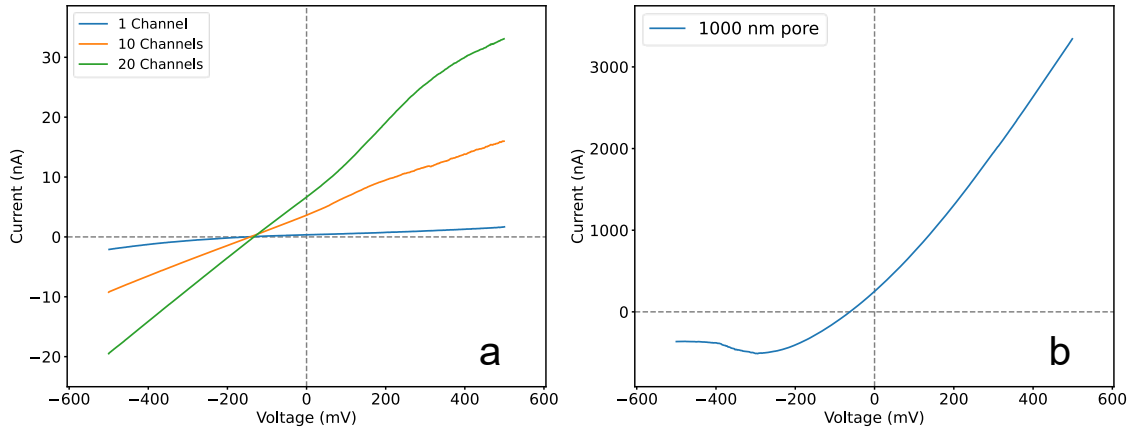

Figure 4.7 ***a*** *Osmotic IV curve of devices with different numbers of channels shows reproducible osmotic voltage and linear ion current enhancement.* ***b*** *IV curve of 1000 nm SiN pore for the extraction of redox potential of our system.*

The power density of our nanochannel can also be derived by considering the power per unit channel surface of the cross section $P_{density} = P_{osm}/A$, where the area of the cross-section A is 1000 nm^2 . Using these values the power density of the single nanochannel was calculated to be 18 kW/m^2, a value higher than that of hBN nanotubes (~3 kW/m^2) [14] and polyimide nanochannel (~3.5 kW/m^2) (see Table 4.1 for more comparisons).

To explore a potential scale-up of this system, we have prepared a few more samples with 10 or 20 nanochannels distributed around a single MoS_2 window as depicted in Figure 4.8. The results show sub-linear short-circuit current (I_{short}) enhancement while the open-circuit voltage (V_{open}) remains at a similar level. We can obtain the average osmotic power density of 10 channels device and 20 channels device as 14425 W/m^2 and 33723 W/m^2, respectively. The power densities reported here for both single and multi-channel devices are normalized to the total cross-sectional area of the active nanochannel(s). This approach is commonly used in fundamental nanofluidic studies to evaluate the intrinsic efficiency of channel material and structure. The consistent power density across devices

with different numbers of channels demonstrates the robustness and scalability of our platform. All multi-channel devices are fabricated in the same plane, with minimal ion concentration polarization (ICP) due to the long channel length and small gradient difference.

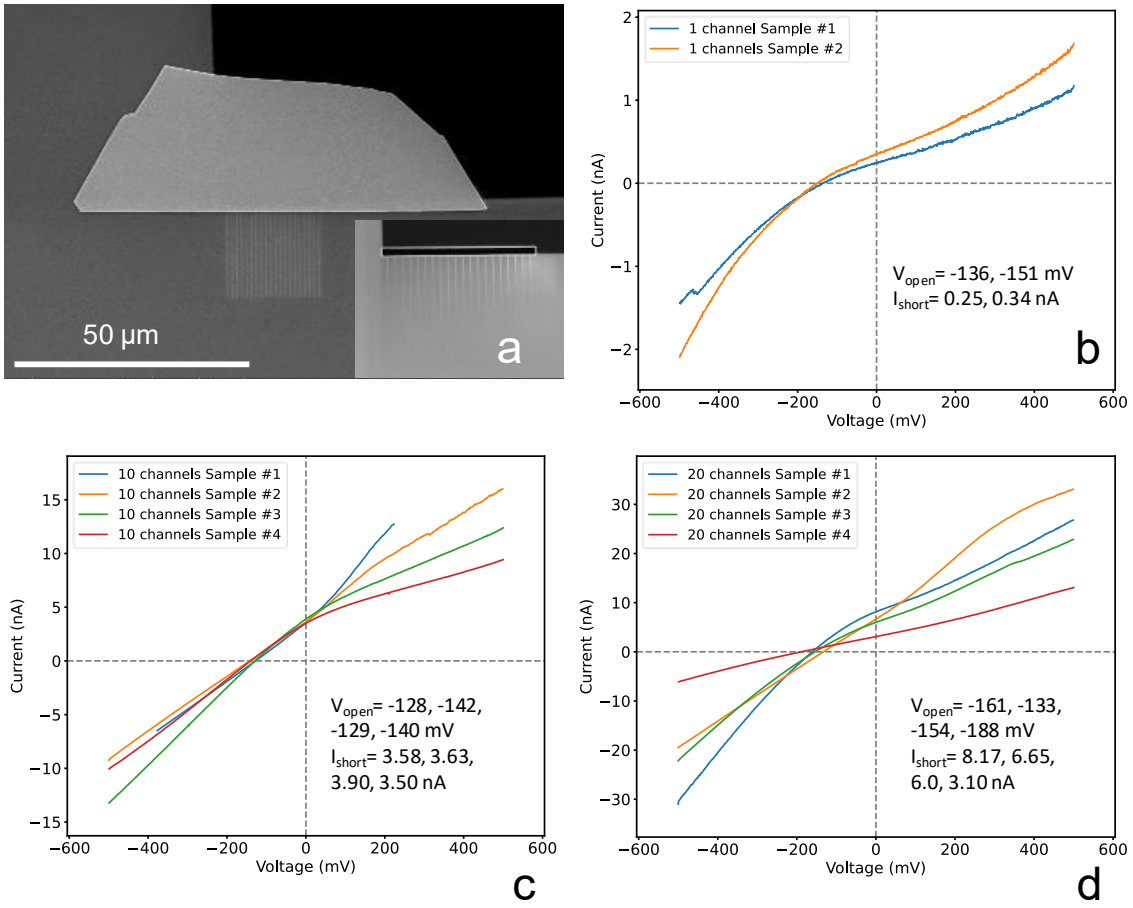

Figure 4.8 ***a*** *SEM image of 10 nanoslits fabricated by FIB which is covered by thick MoS2 flakes. (b-d) are the IV curves of MoS2/SiN nanochannel devices with different number of channels under the same PBS gradient.*

The gate-tunable ion transport observed in the MoS_2/SiN nanochannel can be understood through the interplay of four interconnected physical parameters: channel dimensions, Debye screening length, gate-induced surface charge modulation, and ion concentration polarization.

The nanochannel has a depth h ≈ 5–20 nm and width w ≈ 100 nm, defining a slit-like geometry with an aspect ratio h/w ≈ 0.05–0.2. At the operating electrolyte concentration of 10 mM KCl, the Debye screening length is $\lambda_D \approx 3$ nm. Since h is only a few times λ_D, the electrical double layers (EDLs) extending from the MoS_2 (top) and SiN (bottom) walls

partially overlap across the entire channel height. This confinement increases the contribution of counterions to the total ionic transport and makes the conductance more sensitive to changes in wall surface charge.

Table 4.1 Comparison of osmotic power density in nanofluidic and nanopore-based energy conversion systems.

System	Geometry / Thickness	Electrolyte Gradient	Power Density (W/m²)	Reference
This work: single channel	~10 nm depth, 100 nm width	1X / 10X PBS	~18,000	This study
This work: 10-channels	Same as above	1X / 10X PBS	~14,425	This study
This work: 20-channels	Same as above	1X / 10X PBS	~33,723	This study
PET nanochannels	20–40 nm	KCl gradient	1,000–5,000	[57]
hBN nanotube	~3 nm diameter	KCl gradient	~3,000	[44]
MoS_2 nanopores	~0.7 nm	KCl gradient	10,000–13,000	[54]
Graphene nanopores	0.34 nm	NaCl/KCl gradients	1,000–2,000	[59]

Gate efficiency—defined as the change in channel conductance per unit change in gate voltage— is governed by the electrostatic coupling between the gate electrode, the MoS_2 layer, and the electrolyte, together with the resulting change in MoS_2 surface charge. Because the MoS_2 flake is thick (>50 nm), the electric field does not penetrate the bulk of the semiconductor as in a thin-film transistor. Instead, gating modulates the surface charge density of MoS_2 through carrier accumulation or depletion at the MoS_2–electrolyte interface, a mechanism supported by prior KPFM studies [105–107] and DFT predictions of surface charge reversal [108]. The asymmetric architecture—where only one wall (MoS_2) is gated while the other (SiN) remains at a relatively fixed surface charge—is the origin of the gate-induced rectification. Under negative gate bias, the surface charge of MoS_2 becomes more negative, creating a strong charge asymmetry between the two walls that manifests as ion current rectification (Figure 4.6d). Under positive gate bias, the MoS_2 surface becomes less negative (or even positive in the ambipolar regime), reversing the direction of rectification.

The channel geometry also influences ICP, particularly when the channel becomes strongly ion-selective. In the present devices, the channel height is approximately 10 nm and the Debye length at 10 mM KCl is approximately 3 nm, placing the system in an intermediate confinement regime rather than the strongly permselective limit. The measured osmotic power densities of the multi-channel devices do not show a clear systematic suppression with increasing channel number, suggesting that severe inter-channel concentration polarization is not dominant under the present experimental conditions. Nevertheless, ICP may become increasingly important for smaller channel heights or lower electrolyte concentrations, where stronger ion selectivity and depletion zones are expected.

4.4 Prolonged Protein Translocation

In a previous study, Dekker's group showed that the 2D material stacks nano-slit (nanochannel) can detect different types of DNA translocation events, thereby introducing such nanochannels as a new tool to probe biopolymer properties [73]. Here we tested the ability of our nanochannel for protein translocations measuring the translocation of BSA. Unlike the evenly distributed negative charge and long strand structure of DNA molecules, protein molecules are normally globular which means the dwell time is quite small which makes detection challenging. The unevenly charge distribution makes it difficult for the electrical force driving the protein molecule translocating through the nano-pores/channels [118]. Sodium dodecyl sulfate (SDS) has been proved to unfold protein and stabilize this denatured state. The absorbed SDS alongside the unfolded protein chain can also introduce uniformed negative charge which can facilitate its electrophoretic translocation through 10 nm solid-state nanopore [119,120].

According to the literature, measuring the magnitude of translocation spikes of BSA protein molecules through ~55 nm SiN nanopore with 20 nm thickness, it is possible to estimate the size of the BSA between 7 to 9 nm [121]. After unfolding SDS, the hydrodynamic radii of BSA-SDS were determined to be around 5.9 nm [122]. Here, we used 1 M KCl and 200 μM SDS solution buffered with Tris-EDTA at pH 8 as the electrolyte to measure the translocation of BSA (~8 mg in 4 mL TE buffer solution, ~30 μM). In our MoS_2/SiN nanochannel, a voltage of 200 mV is sufficient to initiate the translocation of BSA-SDS chains, which is sufficiently low to prevent damage or

delamination of the MoS_2 layers [30]. An ionic current trace of the MoS_2/SiN nanochannel at a bias voltage of 200 mV is recorded over 2 min (Figure 4.9) for translocation events analysis as shown in Figure 4.10. A representative 3-seconds segment highlighting characteristic signal features was selected for detailed analysis and presented in Figure 4.10b. Compared to previously published works of BSA translocation through single-layer MoS_2 nanopore or of BSA-SDS translocation through few nanometers size SiN nanopore, we observed a significant enhancement of the translocation dwell time, which could stem from the noncovalent interaction between the disulfide bonds from BSA chain and the S-vacancies from the MoS_2 surface [86].

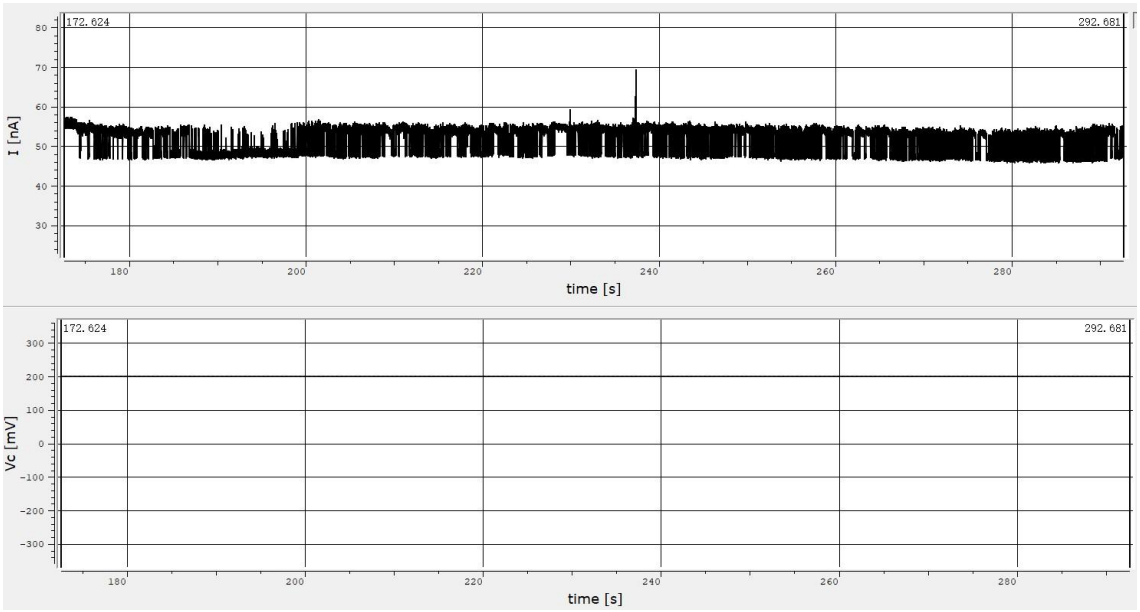

Figure 4.9 BSA translocation events of single nanochannel device under 200 mV with 2 min long recording.

A significant increase in the baseline ionic current was observed in the MoS_2/SiN nanochannel after the channel was incubated by low concentration SDS/KCl solution and the high concentration SDS-modified BSA solution was introduced into the nanochannel (Figure 4.10b), reaching values exceeding 50 nA compared to the smaller baseline of around 20 nA measured under similar electrolyte conditions (Figure 4.5a). After introducing 10 μL unfolded SDS-BSA into the cis reservoir, we observed a pronounced enhancement in the ion current (Figure 4.10d) accompanied by a clearer rectification effect. A non-zero ion current was also recorded in the absence of an applied transmembrane voltage, consistent with the observation with the presence of gating-bias-induced building electrical field across the channel. These collective phenomena suggest that the adsorption of excess unfolded SDS molecules onto the hydrophobic MoS_2 surface

increases its surface charge density and amplifies the proposed mechanism of localized surface charge accumulation near the channel edge. Additionally, the SDS solution itself introduces high ionic strength (due to its Na^+ counter-ions), further elevating the bulk conductivity within the nanochannel.

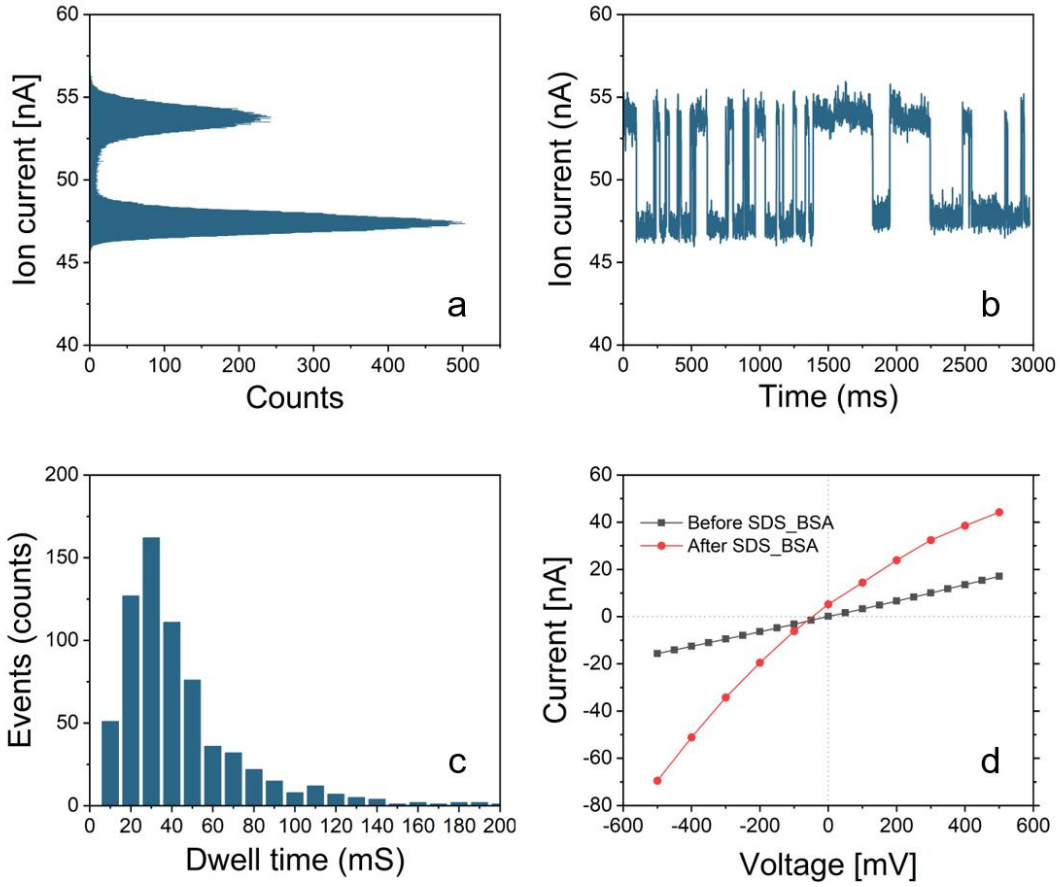

Figure 4.10 Translocation analysis of BSA through the MoS_2/SiN nanochannel under an applied voltage of +200 mV. ***a*** *Dwell time distribution;* ***b*** *Section of translocation trace;* ***c*** *Ion current blockade histogram;* ***d*** *IV curve of the single channel before and after the injection of SDS linearized BSA solution.*

4.5 Summary

In this chapter, we experimentally investigated the ion transport through MoS_2/SiN nanochannels with width ~100 nm and depth ~10 nm, demonstrated its ion current tunability through gating electrode and applications on osmotic power generation and linearized BSA translocation/detection. The ambipolar nanofluidic ion transistor behavior suggests the surface charge tunability of MoS_2 flake. Further work can be expected to extend the single nanochannel configuration to multi-channel structures with separate gate electrodes to achieve multiplex tunability which can be used as an ionic gate. The

large dwell time of linearized BSA translocation indicates the potential of utilizing the interaction between molecules and MoS_2 surface for molecule sensing. While Device yield remained a key limitation of the MoS_2/SiN platform. Of approximately 20 single-channel devices prepared, only three (~15%) showed measurable gate-dependent ion transport. The main failure modes were electrical leakage associated with the dielectric isolation layer and electrode alignment, together with occasional MoS_2 sagging or delamination during wetting and electrolyte exchange. This work may facilitate future fluidic studies along with those applications.

Chapter 5 Transmembrane Voltage Tunable Precipitation inside SiN Nanopores

The previous chapters have demonstrated that ion transport through solid-state nanopores can be modulated by external stimuli that alter the physical or electrostatic state of the channel. Both strategies achieve dynamic control of ionic conductance, yet they share two fundamental limitations. First, they require continuous external stimulation to maintain the gated state: the laser must remain on PNIPAM modified nanopores, and the gate voltage must be continuously applied to MoS_2 surface. Once the external stimulus is removed, the system relaxes back to its equilibrium state very fast—the polymer re-swells, or the surface charge equilibrates. Second, the gating mechanism is essentially physical: the pore geometry, surface charge distribution, or steric occupancy are altered, but the chemical identity of the channel interior remains unchanged.

This requirement for sustained external input presents a critical obstacle for neuromorphic applications. Biological synapses maintain their potentiated or depressed states for minutes to hours after the stimulus has passed, a property known as long-term plasticity that is widely regarded as the cellular basis of learning and memory. A nanofluidic device that relaxes immediately upon stimulus removal cannot emulate this behavior; it can only respond transiently. Moreover, the on/off ratios achievable by physical gating are ultimately limited: even under strong electrostatic gating, the pore cannot be entirely depleted of charge carriers unless the channel dimensions approach the Debye length, which requires sub-10 nm confinement that is difficult to fabricate and operate reproducibly. Polymer brushes can physically occlude the pore only to the extent permitted by their grafting density and swollen volume. In principle, a fundamentally different gating mechanism—one that creates a persistent solid physical barrier inside the pore, and whose state can be retained without continuous external energy input—could circumvent both the retention-time and on/off-ratio limitations simultaneously.

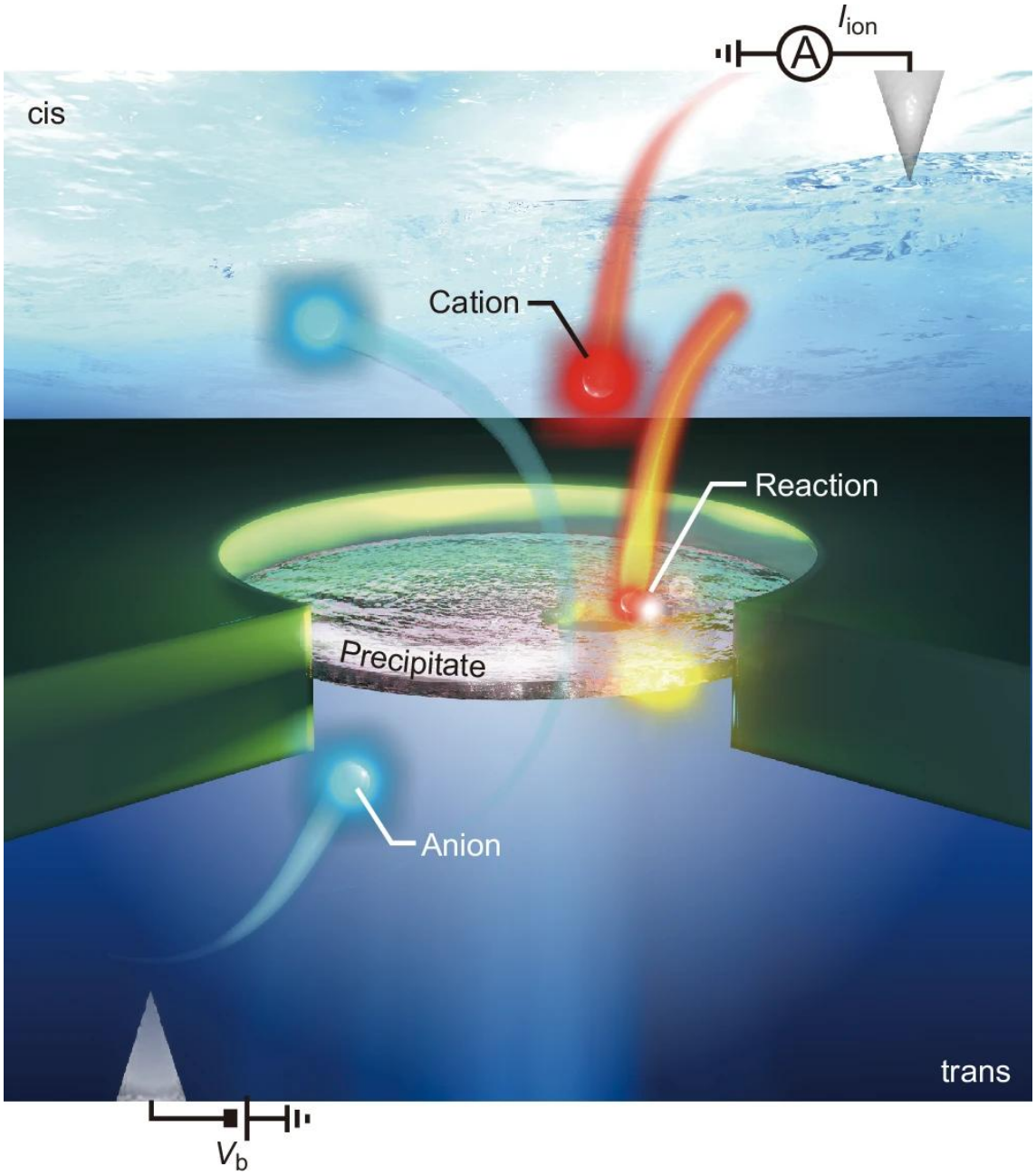

Figure 5.1 A Schematic illustration depicting ion transport-triggered precipitation reaction inside a nanopore. The transmembrane voltage V_b induces the electromigration of ions. The resulting cation flow causes chemical reactions to form or dissolve a metal phosphate compound in a voltage-controllable fashion. The associated dynamic change in the effective pore size is measured by the ionic current I_{ion}.

This chapter introduces a synthetic implementation of this principle: voltage-controlled in-pore precipitation and dissolution of metal phosphates as a gating mechanism. As depicted in Figure 5.1, the core concept is that a transmembrane voltage drives the electromigration of reactive cations from one reservoir into the nanopore, where they encounter phosphate ions present in the buffer of the opposing reservoir. The resulting local supersaturation causes a solid precipitate to form, physically occluding the

pore to ionic flow. Reversing the voltage polarity withdraws the cation supply, and the precipitate dissolves, reopening the pore. Crucially, the precipitate, once formed, remains stable even when the driving voltage is removed—the solid phase does not spontaneously dissolve under neutral pH conditions. This means the gating state can be retained without continuous power consumption, offering an intrinsic chemical memory that the physically gated systems cannot provide. Because the solid phase is impermeable to ions, the current blockade can also be nearly complete, yielding rectification ratios far beyond those attainable by electrostatic or steric gating alone.

The electrical signatures of this chemical gating are extreme: a rectification ratio exceeding 40,000, which is more than an order of magnitude higher than state-of-the-art nanofluidic diodes [123–126]. The time-dependent nature of the precipitation/dissolution process also introduces a history-dependent conductance, realizing a nanofluidic memristor with sub-nanowatt power consumption [127]. The chapter proceeds in two parts. First, the electrical phenomena—strong ionic rectification, memory effects, and memristive switching—are established in conventional SiN nanopores. Second, to unambiguously prove that these observations originate from a chemical reaction confined within the pore, an advanced plasmonic nanopore platform is introduced to perform in situ surface-enhanced Raman spectroscopy (SERS) during voltage cycling. This integrated electrical–optical approach provides direct vibrational signatures of the phosphate precipitates and confirms the chemical nature of the gating mechanism.

5.1 Experimental Strategy for Voltage-Gated Precipitation

To realize chemical gating in a nanopore, one must create conditions under which a solid phase can be formed and dissolved reversibly within the pore volume, and the entire process must be controllable by a single experimental parameter: the transmembrane voltage. This section describes the experimental configuration designed to evaluate the feasibility of such voltage-controlled precipitation and outlines the working hypothesis of the mechanism.

The key design principle is solution asymmetry, wherein two reservoirs divided by the nanopore membrane are filled with different electrolyte solutions. While these solutions are independently stable and homogeneous, their interaction is known to produce an insoluble precipitate. Specifically, the *trans* side always contains phosphate-buffered saline (PBS) with 1.37 M NaCl at pH 7.4, providing a reservoir of phosphate ions (HPO_4^{2-}

and $H_2PO_4^-$) at physiological pH. The *cis* side is filled with a divalent or trivalent chloride salt ($CaCl_2$, $MnCl_2$, $MgCl_2$, or $AlCl_3$, typically at 2 M concentration) dissolved in water without phosphate buffer. The nanopore itself is a bare SiN nanopore with diameter d_{pore}, typically 300 nm. When these two solutions are mixed in a bulk beaker, a white precipitate forms immediately, consistent with the known insolubility of metal phosphates at neutral pH [128–130].

Under an applied transmembrane voltage (V_b), the resulting electric field drives the electromigration of ions through the pore. The central hypothesis is that the polarity of V_b dictates the dominant cation species within the pore, thereby determining the local chemical environment. At positive V_b, cations from the *trans* PBS are driven through the pore into the *cis* side, irrespective of the *cis* salt. The pore interior therefore remains free of divalent cations, and no precipitation occurs; the ionic current is determined by the bulk conductivity of the solutions. At negative V_b, however, the divalent cations (Ca^{2+}, Mn^{2+}, etc.) are electromigrated from the *cis* reservoir into the pore. Upon encountering phosphate ions diffusing or migrating from the trans reservoir, these cations induce local supersaturation of metal phosphate. Provided that the kinetics of nucleation and growth are sufficiently rapid relative to the ion transit time, a solid precipitate is expected to form, occluding the pore and consequently suppressing the ionic current.

Two extra fabrication process were designed to monitor the local precipitation inside the nanopore. For thermal detection, an Au/Pt nanowire thermocouple was embedded in proximity to a 60 nm-diameter nanopore, enabling simultaneous recording of ionic current and local temperature during voltage cycling [131,132]. For chemical identification, a plasmonic nanopore platform was designed in which the SiN membrane was coated with a Ti/Au bilayer and a bulls-eye grating was milled around the pore by focused ion beam. This grating concentrates the incident laser field into the nanopore, providing the electromagnetic enhancement necessary for surface-enhanced Raman scattering (SERS) while preserving the electrical gating function [68,133]. The thermal and spectroscopic results from these devices will be presented in Sections 5.2 and 5.4, respectively.

5.2 Electrical Signatures of In-Pore Precipitation and Dissolution

5.2.1 Strong ion rectifications under salinity difference

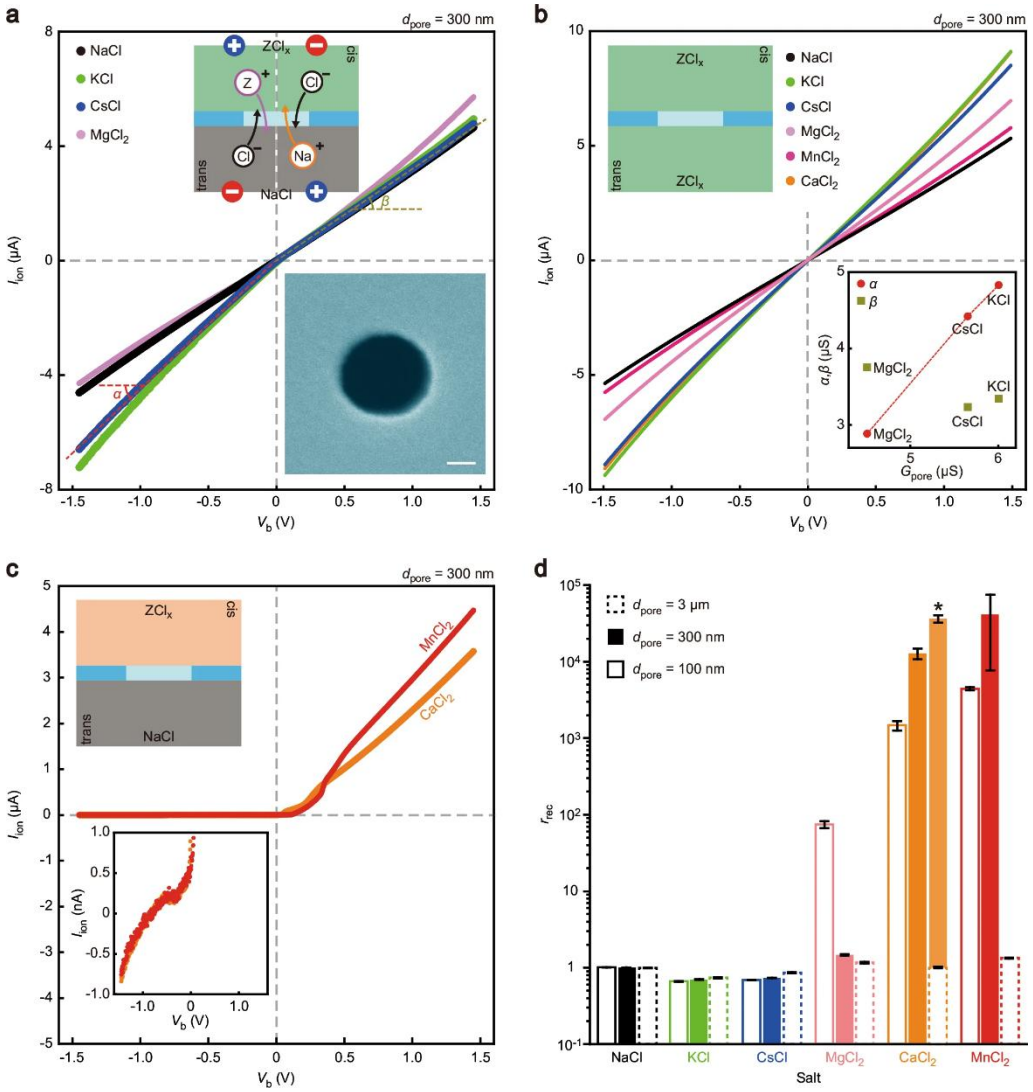

Figure 5.2 Ionic current rectifications in nanopores under salt difference. ***a*** *I_{ion} versus V_b characteristics obtained for a 300 nm pore with the cis side filled with 1.37 M NaCl (black), 2 M KCl (green), 2 M CsCl (blue), and 2 M $MgCl_2$ (pink) while the trans side always with 1.37 M NaCl (pH 7.4). Red and dark yellow dashed lines are linear fitting to the plots at the negative and positive V_b regimes, respectively, which give the slopes α and β. Inset sketch depicts the difference in the electromigration of cations and anions under negative (left) and positive V_b (right). The scanning electron micrograph displays a 300 nm nanopore. Scale bar denotes 100 nm.* ***b*** *The ion transport properties under no salt difference (NaCl (black), KCl (green), CsCl (blue), $MgCl_2$ (pink), $MnCl_2$ (magenta), and $CaCl_2$ (orange)). The salinity was also the same at cis and trans (1.37 M for NaCl and 2 M for the rest of the salts). The inset plots α (red) and β (dark yellow) in* ***a*** *as a function of the nanopore conductance G_{pore} with no salt difference.* ***c*** *Ionic current rectifications were observed for 2 M $CaCl_2$ (orange) and $MnCl_2$ (red) at the cis with the trans filled with 1.37 M NaCl (pH 7.4). Inset is a magnified view of the suppressed ionic current at $V_b < 0$ V.* ***d*** *The rectification ratio r_{rec} at $V_b = \pm 1$ V obtained from the ionic current characteristics measured in pores of three different diameter d_{pore} and various salts at the cis (with the trans filled with 1.37 M NaCl at pH 7.4). r_{rec} tends to be close to 1 when the I_{ion}–V_b characteristics show ohmic behaviors. On the other hand, $r_{rec} > 1$ denotes I_{ion} suppression at negative transmembrane voltage. The high r_{rec} for the 3 μm micropore with $CaCl_2$ is a result obtained at a low V_b scan rate of 6.5 mV s^{-1} (marked by an asterisk), while the other data are of 65 mV s^{-1}. Note that the rectification ratio attains over 40,000 for the case of a 300 nm-sized nanopore with a $MnCl_2$/NaCl configuration.*

Ionic current (I_{ion}) was measured under transmembrane voltage (V_b) with a scan rate (r_{scan}) of 65 mV/s in phosphate-buffered saline containing 1.37 M NaCl at pH 7.4 (hereafter, NaCl solution refers to the phosphate buffer unless otherwise denoted). The observed ohmic behavior showed a slope ($G_{pore} = I_{ion}/V_b$) of 3.2 μS (Figure 5.2a), consistent with Maxwell–Hall's model [134] for d_{pore} of 300 nm and solution resistivity of 0.08 Ω m (with negligible contributions of surface conduction due to the relatively large pore size compared to the sub-nanometer scale Dukhin length in the high ionic strength saltwater [135]). On the other hand, replacing NaCl at the cis compartment with other salts resulted in asymmetry in the I_{ion}–V_b characteristics. In the case of KCl and CsCl (2 M concentration unless otherwise stated), for instance, G_{pore} tended to be higher under negative voltages. $MgCl_2$ also rendered a similar feature yet with an opposite trend in the conductance at $V_b < 0$.

Here, the ionic conductivity is affected by the concentrations and mobilities of cations and anions. From this viewpoint, it is noticeable that positive transmembrane voltage generates electromigration flow of Na^+ through the pore no matter the salts in the cis, giving rise to a similar conductance at $V_b > 0$ (Figure 5.2a). Likewise, the conductance at negative voltages can be explained by the distinct mobilities of the three cations, as shown by the linear relationship with G_{pore} under homogeneous salt solutions (Figure 5.2b). It, thus, demonstrates V_b -controlled selective transport of cations in the nanopore under the salt difference across the membrane.

In stark contrast to the ohmic behaviors, $CaCl_2$ and $MnCl_2$ exhibited strong suppression of the ionic current at $V_b < 0$ (Figure 5.2c). Strikingly, the rectification ratio $r_{rec} = |I_{+1}/I_{-1}|$ reached over 40,000, where I_{+1} and I_{-1} are I_{ion} at V_b = 1 V and −1 V, respectively (Figure 5.2d). Although still not competitive to solid-state electronic devices, this r_{rec} is more than an order of magnitude higher than the state-of-the-art nanofluidic diodes [123,124] relying on permselective transport [126] and electroosmotic flow mechanisms [125].

5.2.2 Understand the in-pore chemical reactions

The observed strong rectification anticipated formations of a matter via V_b-derived reactions that occluded the space for the electromigration of ions through the pores. To verify the chemical composition of the matter formed inside the pore, Raman spectroscopy analyses and X-ray photoelectron spectroscopy (Figure 5.3 and 5.4) were performed with the white substance appeared upon mixing bulk solutions of NaCl and

$CaCl_2$ (or $MnCl_2$), which is ascribable to precipitation reactions of divalent and trivalent cations with the phosphoric acid included in the electrolyte buffer to form metal phosphates.

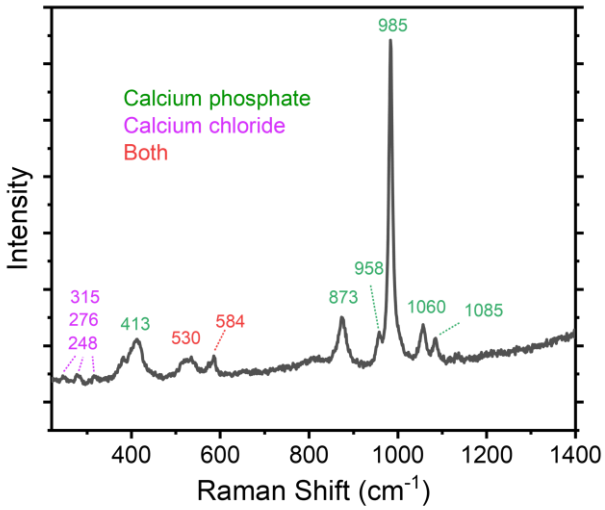

Figure 5.3 Raman spectrum of the white substance precipitated in the mixture solution of $CaCl_2$ water and phosphate buffered saline. Literature values of characteristic Raman peaks for Ca(OH)2 are reported to be found at around 260 cm^{-1}, 260 cm^{-1}, 360 cm^{-1}, 700 cm^{-1}, and 1100 cm^{-1} [136,137] which are not present in the spectrum obtained for the white precipitates (red). Instead, the pronounced peaks at around 400 cm^{-1} and 1000 cm^{-1} (green) suggest that the white precipitates are comprised mostly with $CaPO_x$ [35,138], in addition to a small amount of $CaCl_2$ (purple).

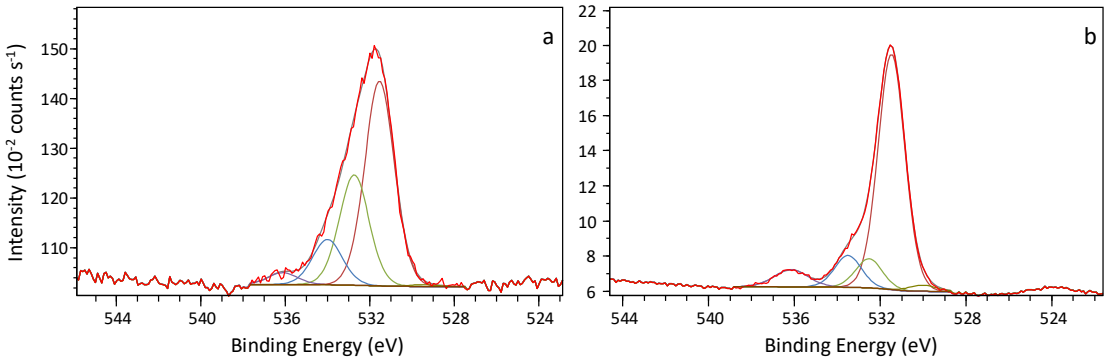

Name	Position	FWHM	%Area
PO4; C=O	531.54	1.65	54.71
C-O	532.75	1.65	29.40
H2O	534.01	1.65	12.11
NaKII	536.12	1.65	3.24
CaO	529.50	1.65	0.55

Name	Position	FWHM	%Area
PO4; C=O	531.46	1.46	72.53
C-O	532.51	1.46	9.07
H2O	533.49	1.46	9.87
NaKII	536.14	1.46	6.54
MnO	530.01	1.46	2.00

*Figure 5.4 X-ray photoelectron spectroscopy (XPS) analysis of precipitate compounds. **a-b**, XPS spectra of white precipitated appeared in mixture solutions of 2 M $CaCl_2$ **a** and $MnCl_2$ **b** with phosphate buffered saline. The features at around 531 eV indicate that the precipitates are phosphate compounds.*

To further verify the reaction-mediated ionic conductance transition mechanism, we performed simultaneous measurements of I_{ion} and the temperature T_{pore} at a nanopore to

detect the local heat dissipation involved in the chemical processes (Figure 5.5a). For this, we embedded a nanowire thermocouple [131] at the proximity of a 60nm-sized pore. We observed rectifying behavior upon scanning V_b with $CaCl_2$ solution at the cis. At the same time, the thermovoltage V_t at the thermocouple was recorded, from which T_{pore} was deduced through the relation $T_{pore} = 5.3\times10^6 V_t$ obtained in the calibration measurements [139]. T_{pore} was found to increase steadily with V_b in the positive voltage regime denoting the local Joule heating by ion transport [132,140].

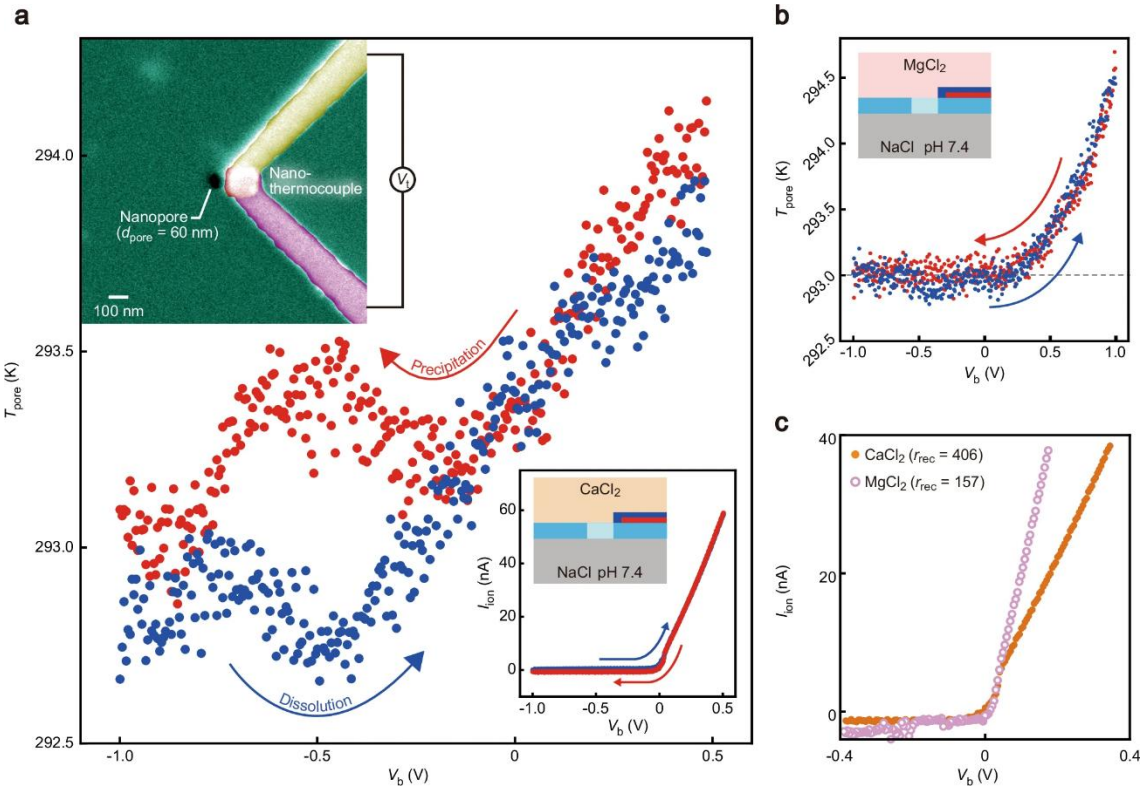

Figure 5.5 Cation flow-mediated precipitation/dissolution reactions of metal phosphates in nanopores. ***a*** *Change in the nanopore temperature T_{pore} during voltage scans for a 60 nm nanopore with the $CaCl_2$/NaCl configuration. Red and blue plots were recorded during negative and positive V_b scans, respectively. Inset electron micrograph at the upper left shows the device used for the measurement, where the Au/Pt thermocouple was used to probe the temperature at the point of contact in the vicinity of the pore. The plots at the lower right are the transmembrane ionic current simultaneously recorded with the thermovoltage V_t at the thermocouple representing rectifying behavior.* ***b*** *T_{pore}–V_b characteristics acquired for a $MgCl_2$/NaCl system. Arrows denote the voltage scan directions (positive (blue) and negative (red)). No notable change in the nanopore temperature was observed reflecting the small reaction heat generated in the precipitation/dissolution of magnesium phosphates.* ***c*** *Simultaneously recorded I_{ion}–V_b characteristics demonstrating ionic current rectification similar to the case in the $MgCl_2$/NaCl system (pink open circles). The result for the $CaCl_2$/NaCl configuration is also shown (orange solid circles). Voltage scan rate is 1 mV s^{-1} in (d–f).*

In contrast, the nanopore temperature showed a temporal increase to above room temperature upon decreasing V_b to below 0V (Figure 5.5a), which is not attributable to

the ionic heat dissipation since I_{ion} is strongly suppressed under the negative voltage. Instead, it suggests the dissipation of heat generated in the precipitation process. Analogously, T_{pore} exhibited a decrease when scanning back V_b toward 0V, indicative of local cooling by heat adsorption during the calcium phosphate dissolution. No such trait emerged for $MgCl_2$ despite its similar ionic current characteristics to $CaCl_2$ (Fig. 5.5b, **c**, presumably due to the relatively small reaction enthalpy involved in anticipating negligible heat dissipation in the precipitation/dissolution stages. Although the synthesis of the metal phosphates in non-alkaline media is generally a complicated process for predicting whether the reactions inside the nanopore should be endothermic or exothermic [141], the overall results consistently suggest the ion transport-mediated in-pore precipitation/dissolution as a primary factor of the extreme Iion rectifications.

5.3 Dynamic Behavior: Memory Effects and Nanofluidic Memristors

The kinetics of precipitation and dissolution introduce a time-dependent, history-dependent conductance that goes beyond simple rectification. Figure 5.6a–d illustrates this in a 3 μm micropore with $CaCl_2$. Initially, at a fast scan rate of 650 mV s^{-1}, the pore behaves as an ohmic resistor. When the scan rate is slowed to 6.5 mV s^{-1}, strong rectification emerges, indicating that a precipitation layer has formed. If the scan rate is subsequently increased to 650 mV s^{-1} and voltage scans are repeated, the rectification gradually vanishes and the pore returns to an ohmic state. Yet the pore is not chemically pristine: if the scan rate is again set to 65 mV s^{-1}, the diode-like behavior immediately reappears. This history-dependent switching suggests that residual crystal seeds on the pore wall survive the dissolution step and facilitate nucleation in subsequent cycles, lowering the kinetic barrier for precipitation. The pore thus possesses a memory of its voltage history encoded in the surface density of nucleation sites.

This training effect is also crucial for memristor operation. Before stable potentiation/depression cycles can be achieved, a series of voltage scans must be performed to form an initial phosphate layer that serves to initialize the memristor state. Without this pretreatment, the nanopore memristor is not reliably controllable by voltage pulses (Figure 5.8b). The requirement for conditioning is a distinctive feature of this chemically based memory: the device must be “taught” to precipitate in a controlled manner before it can exhibit predictable synaptic-like plasticity.

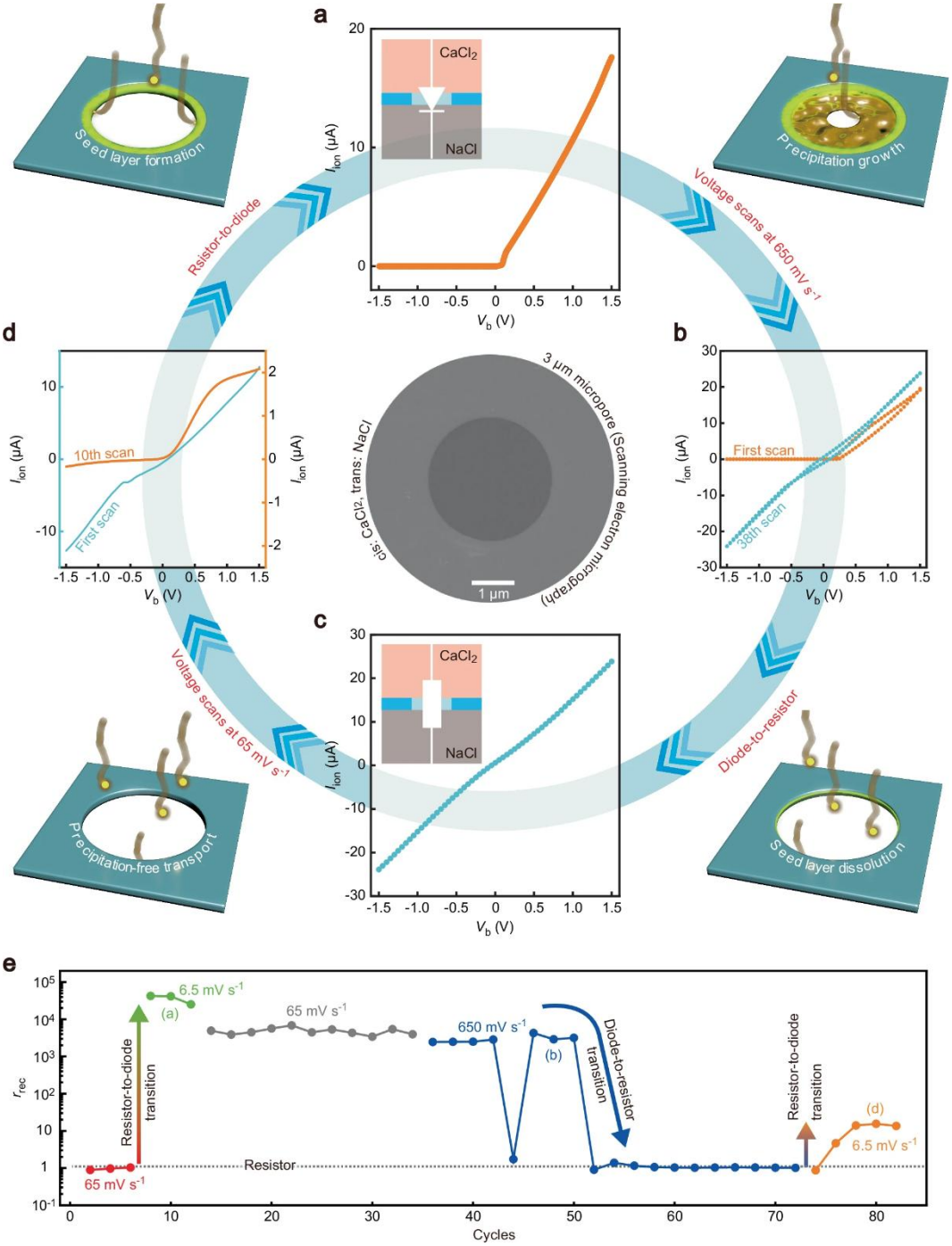

Figure 5.6 In-pore reaction-mediated memory effect in micropore ionic conductance. ***a*** *Originally, a 3 μm micropore with a $CaCl_2$/NaCl arrangement behaved as an ohmic resistor at a voltage scan rate higher than 65 mV s^{-1}. However, the lower scan rate of 6.5 mV s^{-1} led to the emergence of extreme rectification suggestive of precipitation/dissolution reactions of calcium phosphates in the pore.* ***b*** *and* ***c*** *Meanwhile, repetitively scanning V_b at a faster rate (650 mV s^{-1}), the micropore gradually returned to exhibit a resistor-like behavior.* ***d*** *Subsequent scanning at 65 mV s^{-1} can further make the micropore a diode. The image at the center is a scanning electron micrograph of the micropore of 3 μm diameter.* ***e*** *Changes of the rectification behaviors upon the repetitive voltage scanning. Dotted line denotes r_{rec} = 1.*

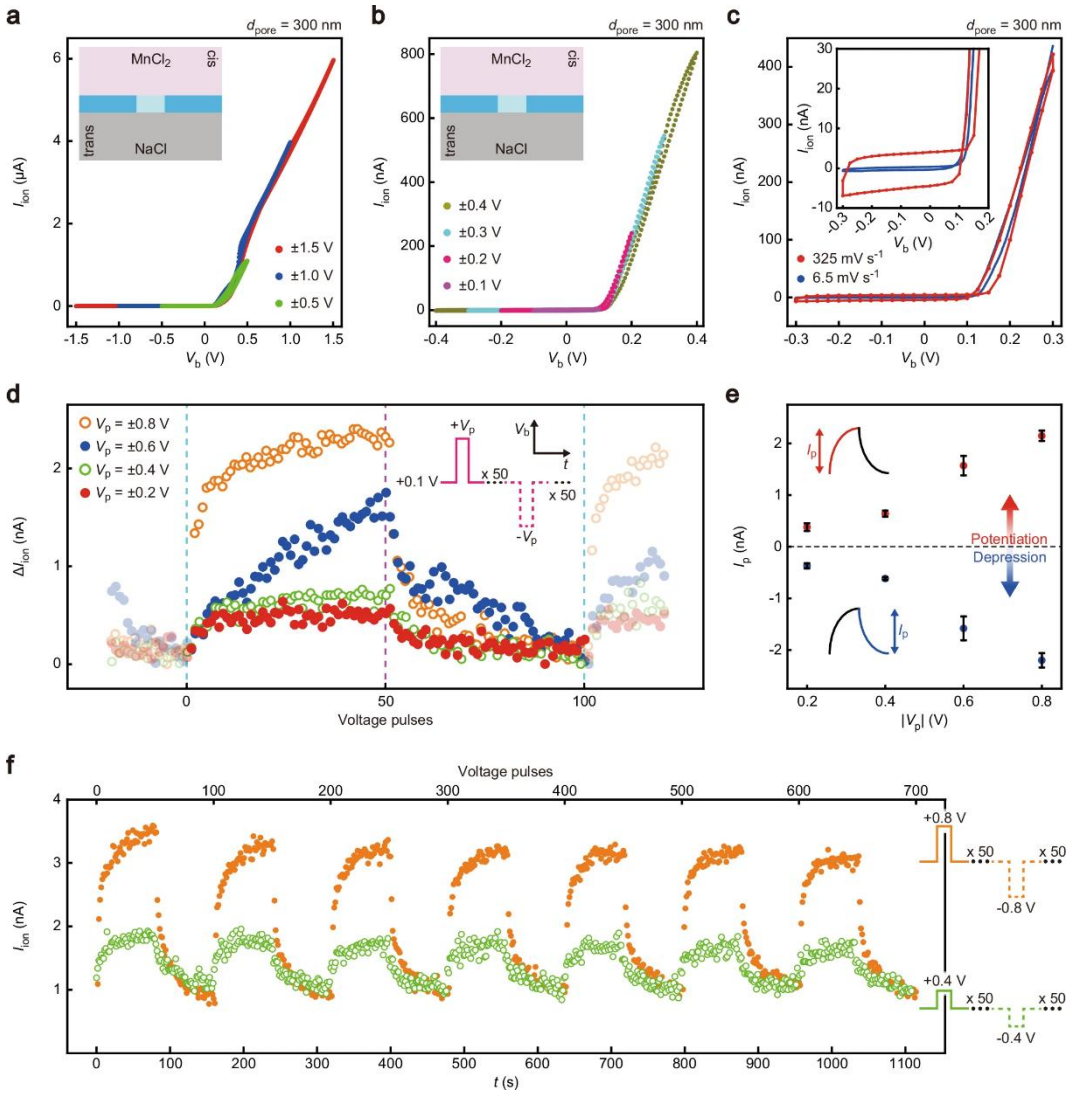

Figure 5.7 In-pore chemical reaction-driven nanofluidic memristor. ***a*** *and* ***b*** I_{ion}–V_b *characteristics of a 300 nm-sized nanopore with an* $MnCl_2$/NaCl *configuration measured under various ranges of transmembrane voltages (±0.1 V (purple), ±0.2 V (pink), ±0.3 V (sky blue), ±0.4 V (dark yellow), ±0.5 V (green), ±1.0 V (blue), ±1.5 V (red)). The insets display the solution configuration around the nanopore membrane in skyblue, where the cis (pink) and trans (gray) compartments are filled with the* $MnCl_2$ *and NaCl solutions, respectively. Note the* I_{ion} *remains suppressed when scanning* V_b *between −0.1 and 0.1 V* ***c*** *Scan rate dependence of* I_{ion}–V_b *displaying pinched hysteresis loops at 6.5 mV* s^{-1} *(blue) and 325 mV* s^{-1} *(red). Inset shows a magnified view of the suppressed* I_{ion} *states.* ***d*** *Memristive characteristics under the applications of 50 ms transmembrane voltage pulses of ±0.2 V (red), ±0.4 V (green), ±0.6 V (blue), and ±0.8 V (orange) amplitudes.* ΔI_{ion} *is the ionic current recorded at +0.1 V after each voltage pulsing (the baseline current was subtracted). The positive and negative pulses drive the potentiation and depression processes of the nanopore memristor via the induced in-pore dissolution/precipitation reactions. Skyblue and purple dashed lines denote the timing when the sign of the voltage pulses were switched from negative to positive and positive to negative, respectively.* ***e*** *The ionic current change* I_p *(defined as* I_{ion} *at the point when the sign of* V_p *was inverted) by the positive (red) and negative (blue) voltage pulses of amplitudes* V_p*. Error bars denote the standard deviations within four independent cycles of potentiation/depression processes on a nanopore. Source data are provided as a Source Data file.* ***f*** *Potentiation/depression of the nanopore memristors under the voltage pulses of* V_p = ±0.8 *V (orange solid circles) and ±0.4 V (green open circles). Read voltage was +0.1 V.*

The memristive character of the in-pore reaction is most directly demonstrated in the pinched hysteresis loops of the I_{ion}–V_b curves (Figure 5.7c). A pinched hysteresis—current crossing zero near zero voltage but following different paths for the forward and reverse sweeps—is the accepted fingerprint of a memristor [127]. By repeatedly switching the voltage polarity, one can drive the pore conductance between higher and lower states (Figure 5.7d-f).

Figure 5.7d shows the results of applying trains of 50-ms voltage pulses to a 300 nm pore with $MnCl_2$/PBS configuration. Positive pulses (e.g., +0.8 V) dissolve the phosphate, incrementally opening the pore and increasing the conductance measured at a small read voltage of +0.1 V (potentiation). Negative pulses (–0.8 V) drive precipitation, closing the pore and decreasing the conductance (depression). The conductance modulation is gradual and approximately symmetric over more than 1000 s of cycling (Figure 5.7e). The energy consumption per pulse is in the sub-nanowatt range, several orders of magnitude below that of conventional solid-state memristors [15,142,143]. Similar behavior was observed in $CaCl_2$ systems, though at a higher baseline conductance reflecting the different solubility product of calcium phosphate (Figure 5.8a).

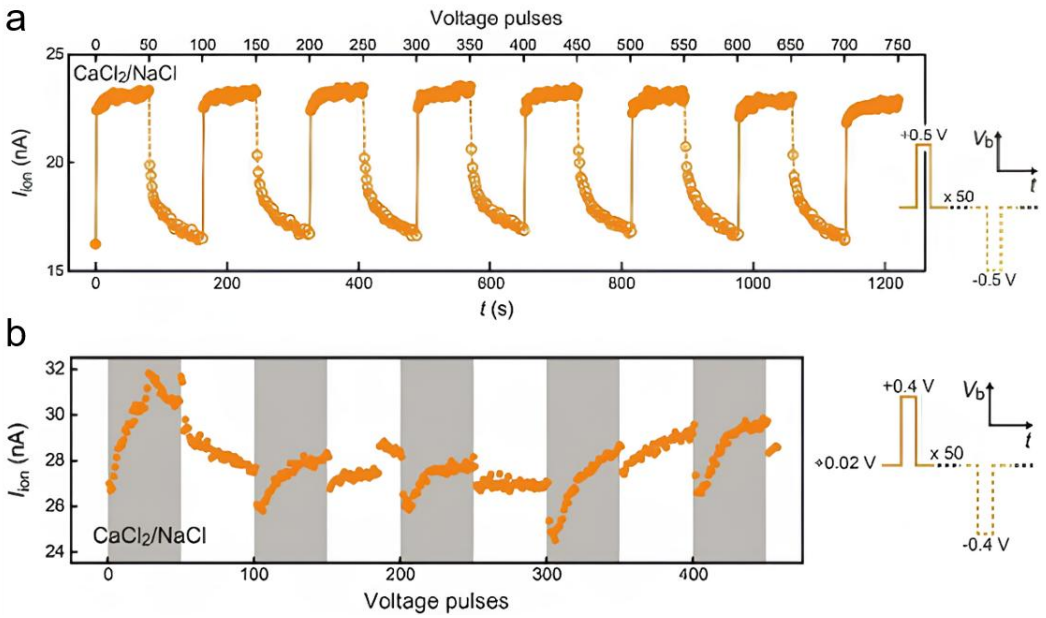

Figure 5.8 Memristive characteristics of a 300 nm pore with CaCl2/phosphate buffered saline. ***a*** *with training and* ***b*** *without training process.*

The physical origin of the memristive behavior is the slow, voltage-controlled accumulation or removal of solid phosphate on the pore wall. During a negative voltage pulse, Ca^{2+} or Mn^{2+} ions are driven into the pore and precipitate with phosphate, adding

mass to an existing layer. During the positive pulse, the cation supply is cut off, and the local environment shifts toward the acidic *cis* solution, causing partial dissolution. However, dissolution is not complete on the timescale of a short pulse; a residual crystalline layer remains, acting as seed for the next precipitation cycle. The pore conductance thus reflects the dynamically evolving thickness of the phosphate layer, which integrates the history of applied voltage.

5.4 In-Situ Spectroscopic Evidence Using Plasmonic Nanopores

All the evidence presented so far—extreme rectification, thermal signatures, SEM/EDS after the fact—supports the precipitation/dissolution hypothesis but is indirect. The nanopore is only about 100 nm thick and 200–300 nm wide, containing a reaction volume on the order of 10^{-3} fL. Conventional analytical techniques cannot resolve chemical species in such a minuscule volume in real time. To definitively identify the precipitate and follow its formation optically, one must (i) concentrate the probing electromagnetic field into the nanopore and (ii) enhance the Raman scattering cross-section of the molecules within it. Surface-enhanced Raman spectroscopy (SERS) in a plasmonic nanopore achieves precisely this goal.

5.4.1 Bullseye structure for SERS

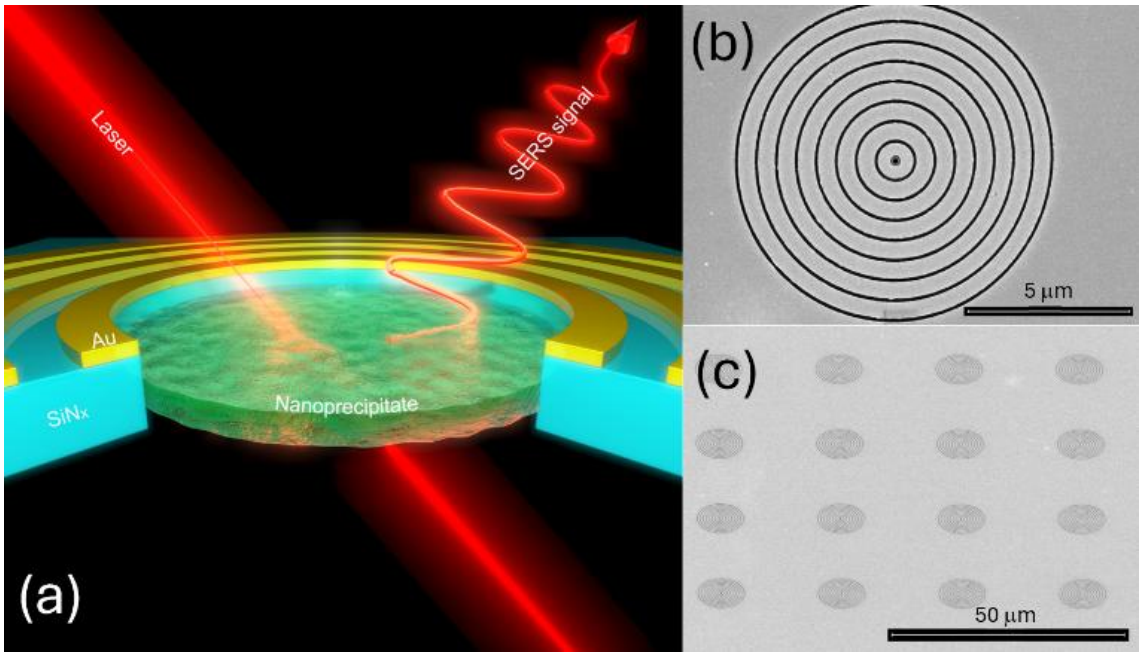

Figure 5.9 SERS measurement of in-pore precipitation. ***a*** *Schematic illustration of the SERS measurement;* ***b*** *top view of a single plasmonic nanopore;* ***c*** *titled view (52°) of plasmonic nanopore array*

The plasmonic nanopore platform replaces the bare SiN membrane with a SiN membrane coated with a 5/25 nm Ti/Au bilayer, into which a bulls-eye grating is milled by focused ion beam (Figure 5.9b,c). The grating period matches the surface plasmon polariton wavelength for 532 nm excitation, the laser wavelength used in the Raman setup. Under illumination, the bulls-eye structure generates a strong near-field enhancement confined to the nanopore aperture, effectively squeezing the electromagnetic field into the same attoliter volume where the chemical reaction occurs (Figure 5.10). This design enables label-free SERS measurements of the chemical species inside a single nanopore.

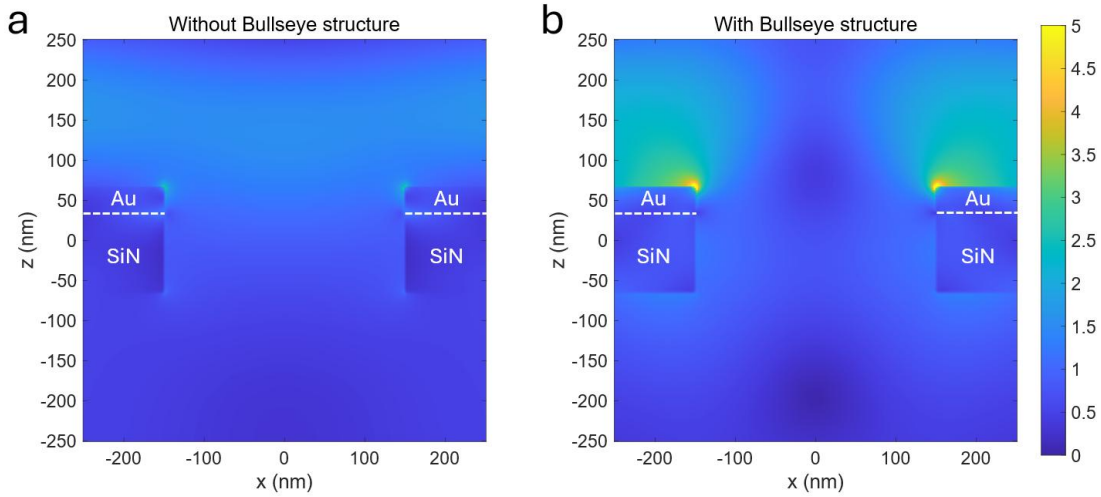

Figure 5.10 Cross-section electrical field intensity of 250nm Au/SiN plasmonic nanopore. ***a*** *nanopore without bullseye structure;* ***b*** *nanopore with bullseye structure. Simulated by ANSYS Lumerical FDTD Solutions.*

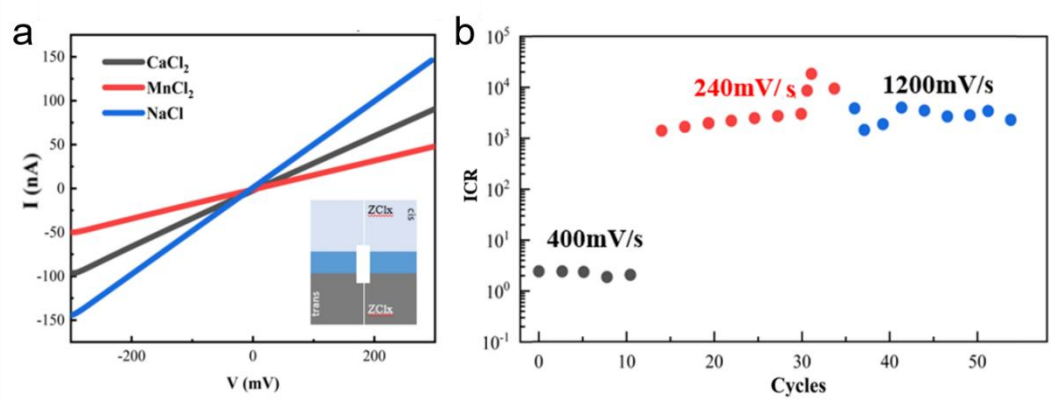

Figure 5.11 Ion current rectification of plasmonics Au/SiN nanopore. ***a*** *the ion transport properties under no salt difference (NaCl(blue), $MnCl_2$(red), and $CaCl_2$ (black)). The salinity was also the same at cis and trans(1.37 M for NaCl and 2 M for the rest of the salts).* ***b*** *ICR values obtained for $CaCl_2$ system at different scan rates.*

Before the optical experiments, the electrical properties of the plasmonic nanopore were verified to ensure that the Au layer does not fundamentally alter the precipitation chemistry. The plasmonic pore, with a diameter of approximately 250 nm, exhibited ohmic conductance of 0.5 µS in symmetric NaCl (Figure 5.11a). Under asymmetric conditions with $CaCl_2$ or $MnCl_2$ on the *cis* side, strong rectification was observed, with ICR values comparable to or exceeding those of bare SiN pores (Figure 5.11b). Thus, the plasmonic pore preserves the chemical gating function while simultaneously providing the optical enhancement required for SERS.

5.4.2 Correlation of electrical gating states with Raman signatures

Raman reference spectra were collected from bulk powders of the individual compounds (Figure 5.12a). PBS shows characteristic phosphate vibrations at 877 cm^{-1}, 979 cm^{-1}, and 1077 cm^{-1}, corresponding to HPO_4^{2-} and $H_2PO_4^-$ modes. Dry $CaCl_2$ and $MnCl_2$ exhibit only a broad band around 1600 cm^{-1} from the H–O–H bending of crystalline water [144]. Importantly, the precipitated salts $Ca_3(PO_4)_2$ and $Mn_3(PO_4)_2$, obtained by mixing the reagents in the same stoichiometry and pH as used in the pore experiments, both show a prominent peak at ~960 cm^{-1}, the symmetric stretching vibration of the phosphate group, as well as a broad water band at ~1600 cm^{-1} (Figure 5.12b) [145,146].

In the in-situ SERS experiment, the Raman laser was focused onto a single plasmonic nanopore from the *cis* side (where only the chloride salt is present, avoiding background from the PBS buffer). The voltage was held at +0.6 V to open the pore and at –0.6 V to close it, with the ionic current monitored to confirm the gating state. Figure 5.12c shows the spectra obtained. In the open-pore configuration, the Raman signal is weak and dominated by the background from the gold surface and the water bending mode. In the closed-pore configuration, a clear new peak emerges at approximately 970 cm^{-1}, matching the phosphate signature of $Ca_3(PO_4)_2$. The intensity of the 1600 cm^{-1} band also increases, consistent with water molecules trapped or incorporated in the precipitated phase. When the voltage is returned to +0.6 V, the 970 cm^{-1} peak disappears, confirming the dissolution of the phosphate and the return to the open-pore state.

The experiment was repeated with $MnCl_2$ using an array of 16 nanopores to increase the total signal (Figure 5.12d). Again, the 970 cm^{-1} peak appeared only in the blocked, negative-bias state and vanished upon switching to the open state. These SERS measurements constitute direct, molecular-level proof that the observed electrical gating

is caused by the reversible formation and dissolution of metal phosphate precipitates within the nanopore.

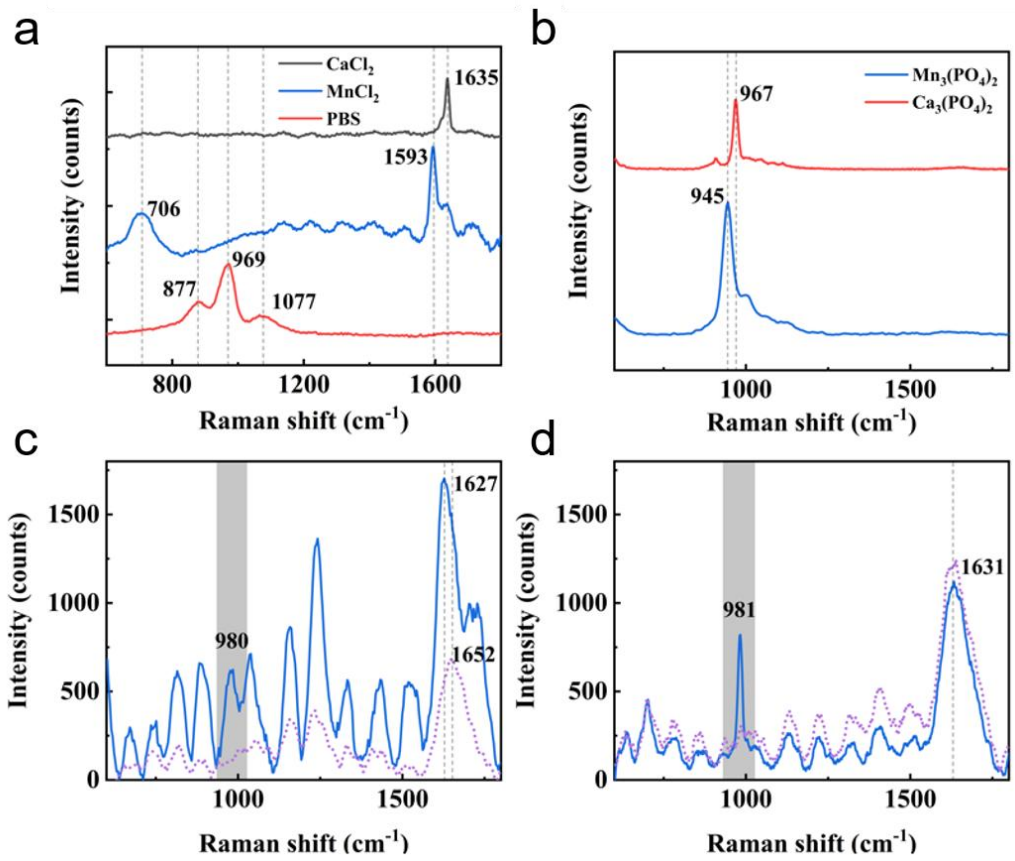

Figure 5.12 In-situ Raman detection of in-pore precipitation. ***a*** *Raman spectra of powdered samples (PBS(red), $MnCl_2$(blue), and $CaCl_2$(black)).* ***b*** *Raman spectra of the precipitate ($Ca_3(PO_4)_2$ (red), $Mn_3(PO_4)_2$ (blue)).* ***c*** *Raman spectra of nanopore opening/closing in a Ca based system (closed (blue), open (purple)).* ***d*** *Raman spectra of nanopore opening/closing in a Mn-based system (closed (blue), open (purple)).*

Although both Ca^{2+} and Mn^{2+} generate a phosphate peak around 960–970 cm^{-1}, subtle differences in the exact peak position and the relative intensity of the water band suggest that the precipitates have distinct structures and hydration states. Calcium phosphate is known to form hydroxyapatite ($Ca_5(PO_4)_3OH$) or amorphous calcium phosphate depending on pH and ion concentrations, while manganese phosphate typically crystallizes as $Mn_3(PO_4)_2 \cdot xH_2O$ [141,147]. The ability to detect these spectral differences in real time, even from a single nanopore, demonstrates the chemical specificity of the combined electrical–SERS platform. This opens the possibility of using different precipitating ions to encode distinct chemical memory states or to create chemically selective sensors.

5.5 Summary

This chapter has introduced and rigorously validated a new mechanism for voltage-gated ion transport in solid-state nanopores: the electrically controlled precipitation and dissolution of metal phosphates within the pore. The approach yields rectification ratios exceeding 40,000, stable current blockade, and a chemically encoded memory effect that enables sub-nanowatt memristive switching. Three complementary lines of evidence—electrical transport, local thermometry, and in-situ SERS—converge to prove that the gating is caused by a reversible solid-state chemical reaction confined to the attoliter volume of the pore.

The integration of plasmonic SERS provides a general methodology for observing chemical reactions in nanopores in operando, a capability that is likely to find applications far beyond the model phosphate system studied here. Future work may extend the concept to other precipitation reactions, electrodeposited polymers, or even enzyme-catalyzed transformations, leveraging the chemical degrees of freedom to create ionic devices with tailored memory, sensing, and logic functions. Combined with the optical gating of Chapter 3 and the electrostatic control of Chapter 4, the chemically gated nanopore completes a versatile platform for ionic computing and smart nanofluidic systems.

Chapter 6 Summary and Conclusions

Nanopore technology has attracted considerable attention because of its potential in applications such as single-molecule detection and sequencing, nanoscale chemical reaction detection, and green energy harvesting. However, the development of tunable nanopore devices for active and smart control remains relatively underexplored. This thesis has demonstrated three hybrid strategies for dynamic ion transport control in solid-state nanopores: thermoplasmonic gating with PNIPAM, electrostatic modulation with MoS_2/SiN heterostructures, and chemically encoded memristive switching via in-pore precipitation. Together, they represent a progression from externally triggered gating to continuously tunable transport and finally to history-dependent ionic memory with extreme rectification (>40,000) and sub-nanowatt switching.

Translating these laboratory demonstrations into practical technologies requires addressing platform-specific scaling challenges, as well as common issues of reproducibility, stability, and integration.

For the thermoplasmonic gating platform (Chapter 3): The current optical addressing scheme relies on a free-space laser and microscope. Moving toward compact, chip-integrated systems would benefit from on-chip waveguides or plasmonic interconnects to deliver light to individual pores without bulky optics. The millisecond switching speed is sufficient for many sensory and adaptive control tasks, but further speed improvements would require optimizing polymer brush density and grafting chemistry to reduce viscoelastic relaxation times. The long-term stability of polymer in the electrolyte also needs to be considered.

For the MoS_2/SiN ionic transistor (Chapter 4): A central challenge is the trade-off between gate control strength and channel dimensions. In current devices (channel depth ~10 nm), the Debye length is comparable to the channel height, enabling effective gating. Scaling to sub-5 nm or Angstrom-scale channels would enhance ion selectivity and rectification but requires solving fabrication challenges: avoiding MoS_2 sagging, ensuring

precise flake transferring. For osmotic power generation, the key is to move from single-channel devices to multi-channel arrays (as shown for 10 and 20 channels) while maintaining power density. However, as multiple channels share reservoirs, concentration polarization might manifest if the gap between channels become too small, while the size of the 2D material also restrict the number of channels. For protein sensing, the prolonged dwell time due to MoS_2-protein interactions is promising for signal averaging, but device-to-device variability and pore clogging remain obstacles. A pragmatic solution would be to use another EBL process make arrays of identical channels.

For the chemically gated memristor (Chapter 5): This platform offers the richest functionality (non-volatile memory, extreme rectification) but also the most complex dynamics. The precipitation-dissolution kinetics depend sensitively on local pH, ion concentration, and temperature. For practical use, the system must be encapsulated and stabilized. The sub-nanowatt power consumption is exceptional, but switching speeds are currently limited by reaction-diffusion times. To accelerate switching, one could reduce pore length (shortening ion transit time) or use cations with faster precipitation kinetics. The ability to tune the memory state via pulse amplitude and duration suggests that arrays of such pores could implement analog synaptic weight matrices for neuromorphic computing, provided that each pore can be addressed independently. A crossbar architecture with orthogonal fluidic channels—while challenging to fabricate—would be the ultimate goal.

Across the three platforms, reproducibility was strongly dependent on the underlying gating mechanism and fabrication complexity. The thermoplasmonic and MoS_2/SiN platforms were primarily limited by fabrication-related variability, whereas the chemically gated platform showed the most reproducible behavior after an initial conditioning process. These results highlight that improving fabrication yield and controlling interfacial variability remain important for translating the demonstrated nanopore concepts toward practical devices.

This thesis has established the physical foundations and experimental tools—plasmonic heating, electrostatic gating, in-pore chemistry, and in-situ SERS—for engineering dynamically programmable ion transport. The path from these demonstrations to functional ionic processors requires sustained advances in nanofabrication, materials chemistry, and circuit architecture.

References

[1] T. Emmerich, N. Ronceray, K. V. Agrawal, S. Garaj, M. Kumar, A. Noy, and A. Radenovic, Nanofluidics, Nat Rev Methods Primers **4**, 69 (2024).

[2] T. Mei, W. Liu, G. Xu, Y. Chen, M. Wu, L. Wang, and K. Xiao, Ionic Transistors, ACS Nano acsnano.3c06190 (2024).

[3] G. Xu, M. Zhang, T. Mei, W. Liu, L. Wang, and K. Xiao, Nanofluidic Ionic Memristors, ACS Nano **18**, 19423 (2024).

[4] J. J. Kasianowicz, E. Brandin, D. Branton, and D. W. Deamer, Characterization of individual polynucleotide molecules using a membrane channel, Proceedings of the National Academy of Sciences **93**, 13770 (1996).

[5] C. Zhao, H. Wang, and H. Zhang, Bio-inspired artificial ion channels: from physical to chemical gating, Mater. Chem. Front. **5**, 4059 (2021).

[6] L. Xue, H. Yamazaki, R. Ren, M. Wanunu, A. P. Ivanov, and J. B. Edel, Solid-state nanopore sensors, Nat Rev Mater **5**, 12 (2020).

[7] X. Lei, J. Zhang, H. Hong, Z. Yuan, and Z. Liu, Controllable Shrinking Fabrication of Solid-State Nanopores, Micromachines-Basel **13**, 923 (2022).

[8] C. Ying, T. Ma, L. Xu, and M. Rahmani, Localized Nanopore Fabrication via Controlled Breakdown, Nanomaterials **12**, 14 (2022).

[9] W. Xin, H. Ling, Y. Cui, Y. Qian, X.-Y. Kong, L. Jiang, and L. Wen, Tunable Ion Transport in Two-Dimensional Nanofluidic Channels, J. Phys. Chem. Lett. **14**, 627 (2023).

[10] P. Liu, X.-Y. Kong, L. Jiang, and L. Wen, Ion transport in nanofluidics under external fields, Chem. Soc. Rev. **53**, 2972 (2024).

[11] C. Lee, L. Joly, A. Siria, A.-L. Biance, R. Fulcrand, and L. Bocquet, Large Apparent Electric Size of Solid-State Nanopores Due to Spatially Extended Surface Conduction, Nano Lett. **12**, 4037 (2012).

[12] A. Esfandiar, B. Radha, F. C. Wang, Q. Yang, S. Hu, S. Garaj, R. R. Nair, A. K. Geim, and K. Gopinadhan, Size effect in ion transport through angstrom-scale slits, Science **358**, 511 (2017).

[13] W. Liu et al., Bioinspired carbon nanotube–based nanofluidic ionic transistor with ultrahigh switching capabilities for logic circuits, Sci. Adv. **10**, eadj7867 (2024).

[14] A. Siria, P. Poncharal, A.-L. Biance, R. Fulcrand, X. Blase, S. T. Purcell, and L. Bocquet, Giant osmotic energy conversion measured in a single transmembrane boron nitride nanotube, Nature **494**, 455 (2013).

[15] G. Paulo, K. Sun, G. Di Muccio, A. Gubbiotti, B. Morozzo della Rocca, J. Geng, G. Maglia, M. Chinappi, and A. Giacomello, Hydrophobically gated memristive nanopores for neuromorphic applications, Nat Commun **14**, 8390 (2023).

[16] J. Cai et al., Magnetic Field Tuning Ionic Current Generated by Chiromagnetic Nanofilms, Acs Nano **16**, 11066 (2022).

[17] C. Zhao, J. Lu, J. Hou, X. Li, J. Wang, L. Jiang, H. Wang, and H. Zhang, Bioinspired Self-Gating Nanofluidic Devices for Autonomous and Periodic Ion

Transport and Cargo Release, Advanced Functional Materials **29**, 1806416 (2019).
[18] A. Ismail et al., Programmable memristors with two-dimensional nanofluidic channels, Nat Commun **16**, 7008 (2025).
[19] Y.-Z. You, K. K. Kalebaila, S. L. Brock, and D. Oupický, Temperature-Controlled Uptake and Release in PNIPAM-Modified Porous Silica Nanoparticles, Chem. Mater. **20**, 3354 (2008).
[20] M. Liu, J. Zhang, Y. Qiao, T. Ye, N. Liu, X. Xu, C. Zou, and S. Huang, Influence of Transmembrane Ionic Current Based on PNIPAM-Modified Nanochannels, J. Phys. Chem. C **123**, 12500 (2019).
[21] Y. Zhang, S. Furyk, D. E. Bergbreiter, and P. S. Cremer, Specific Ion Effects on the Water Solubility of Macromolecules: PNIPAM and the Hofmeister Series, J Am Chem Soc **127**, 14505 (2005).
[22] J. Wang, Y. Jiang, T. Xiong, J. Lu, X. He, P. Yu, and L. Mao, Optically Modulated Nanofluidic Ionic Transistor for Neuromorphic Functions, Angewandte Chemie International Edition **64**, e202418949 (2025).
[23] J. Wang, K. N. Vu, A. D. Abell, A. Santos, and C. S. Law, Nanoporous anodic alumina-based iontronics: fundamentals and applications, J. Mater. Chem. C **11**, 9051 (2023).
[24] X. Hu, H. Xu, J. Lu, F. Cui, H.-A. Wu, F. Wang, L. Jiang, K. S. Novoselov, and H. Wang, Selective ion transport of nonlinear resistive switching by hierarchical nanometer-to-angstrom channels for nanofluidic transistors, Science Advances **11**, eadw7882 (2025).
[25] W. Guan, R. Fan, and M. A. Reed, Field-effect reconfigurable nanofluidic ionic diodes, Nat Commun **2**, 506 (2011).
[26] R. Ren, Y. Zhang, B. P. Nadappuram, B. Akpinar, D. Klenerman, A. P. Ivanov, J. B. Edel, and Y. Korchev, Nanopore extended field-effect transistor for selective single-molecule biosensing, Nat Commun **8**, 586 (2017).
[27] S. Kim, E. I. Ozalp, and J. A. Weldon, Stacked Gated Nanofluidic Logic Gate Membrane, IEEE Trans. Nanotechnology **18**, 536 (2019).
[28] J. Zhou, H. Li, and Y. Hou, Chemical Principles in Regulating Nanofluidic Memristors, Chemistry **7**, 133 (2025).
[29] K. Liu, Y. Wang, M. Sun, J. Lu, D. Shi, and Y. Xie, Resistance-Restorable Nanofluidic Memristor and Neuromorphic Chip, Nano Lett. **25**, 6530 (2025).
[30] B. Radha et al., Molecular transport through capillaries made with atomic-scale precision, Nature **538**, 222 (2016).
[31] R. B. Schoch, J. Han, and P. Renaud, Transport phenomena in nanofluidics, Rev. Mod. Phys. **80**, 839 (2008).
[32] L. Bocquet and E. Charlaix, Nanofluidics, from bulk to interfaces, Chem. Soc. Rev. **39**, 1073 (2010).
[33] Z. Huang, Y. Zhang, T. Hayashida, Z. Ji, Y. He, M. Tsutsui, X. S. Miao, and M. Taniguchi, The impact of membrane surface charges on the ion transport in MoS2 nanopore power generators, Appl. Phys. Lett. **111**, 263104 (2017).
[34] C. Yang, P. Hinkle, J. Menestrina, I. V. Vlassiouk, and Z. S. Siwy, Polarization of Gold in Nanopores Leads to Ion Current Rectification, J. Phys. Chem. Lett. **7**, 4152 (2016).
[35] L.-J. Cheng and L. J. Guo, Nanofluidic diodes, Chem. Soc. Rev. **39**, 923 (2010).

[36] W.-J. Lan, M. A. Edwards, L. Luo, R. T. Perera, X. Wu, C. R. Martin, and H. S. White, Voltage-Rectified Current and Fluid Flow in Conical Nanopores, Acc. Chem. Res. **49**, 2605 (2016).
[37] D. Wang and G. Wang, Dynamics of ion transport and electric double layer in single conical nanopores, Journal of Electroanalytical Chemistry **779**, 39 (2016).
[38] Y. Li, D. Wang, M. M. Kvetny, W. Brown, J. Liu, and G. Wang, History-dependent ion transport through conical nanopipettes and the implications in energy conversion dynamics at nanoscale interfaces, (2014).
[39] W. Brown, M. Kvetny, R. Yang, and G. Wang, Selective Ion Enrichment and Charge Storage through Transport Hysteresis in Conical Nanopipettes, J. Phys. Chem. C **126**, 10872 (2022).
[40] H. Zhang, Y. Tian, and L. Jiang, Fundamental studies and practical applications of bio-inspired smart solid-state nanopores and nanochannels, Nano Today **11**, 61 (2016).
[41] Y. Xu, X. Wang, W. L. Zhang, F. Lv, and S. Guo, Recent progress in two-dimensional inorganic quantum dots, Chem. Soc. Rev. **47**, 586 (2018).
[42] D. Han, X. Dong, G. Yu, T. Gao, and K.-G. Zhou, Tunable mass transport in the artificial smart membranes based on two-dimensional materials, Advanced Membranes **2**, 100045 (2022).
[43] G. Lanzavecchia et al., Plasmonic Photochemistry as a Tool to Prepare Metallic Nanopores with Controlled Diameter for Optimized Detection of Single Entities, Advanced Optical Materials **11**, 2300786 (2023).
[44] J. Svirelis et al., Stable trapping of multiple proteins at physiological conditions using nanoscale chambers with macromolecular gates, Nat Commun **14**, 5131 (2023).
[45] S. Dey, A. Dorey, L. Abraham, Y. Xing, I. Zhang, F. Zhang, S. Howorka, and H. Yan, A reversibly gated protein-transporting membrane channel made of DNA, Nat Commun **13**, 2271 (2022).
[46] T. Ma, M. Walko, M. Lepoitevin, J.-M. Janot, E. Balanzat, A. Kocer, and S. Balme, Combining Light-Gated and pH-Responsive Nanopore Based on PEG-Spiropyran Functionalization, Advanced Materials Interfaces **5**, 1701051 (2018).
[47] G. Wang, A. K. Bohaty, I. Zharov, and H. S. White, Photon Gated Transport at the Glass Nanopore Electrode, J. Am. Chem. Soc. **128**, 13553 (2006).
[48] G. Laucirica, Y. Toum Terrones, V. Cayón, M. L. Cortez, M. E. Toimil-Molares, C. Trautmann, W. Marmisollé, and O. Azzaroni, Biomimetic solid-state nanochannels for chemical and biological sensing applications, TrAC Trends in Analytical Chemistry **144**, 116425 (2021).
[49] A. Stuber, A. Douaki, J. Hengsteler, D. Buckingham, D. Momotenko, D. Garoli, and N. Nakatsuka, Aptamer Conformational Dynamics Modulate Neurotransmitter Sensing in Nanopores, ACS Nano **17**, 19168 (2023).
[50] A. Douaki, A. Stuber, J. Hengsteler, D. Momotenko, D. M. Rogers, W. Rocchia, J. D. Hirst, N. Nakatsuka, and D. Garoli, Theoretical analysis of divalent cation effects on aptamer recognition of neurotransmitter targets, Chem. Commun. **59**, 14713 (2023).
[51] L. Xie, J. Tang, R. Qin, Q. Zhang, J. Liu, Y. Jin, and H. Wang, Surface Charge Modification on 2D Nanofluidic Membrane for Regulating Ion Transport, Advanced Functional Materials **33**, 2208959 (2023).

[52] L. Yang, J. Hu, M.-C. Li, M. Xu, and Z.-Y. Gu, Solid-state Nanopores: Chemical Modifications, Interactions, and Functionalities, Chemistry – An Asian Journal **17**, e202200775 (2022).
[53] D. Zhang, Q. Wang, X. Fan, M. Zhang, J. Zhai, and L. Jiang, An Effective Dark–Vis–UV Ternary Biomimetic Switching Based on N3/Spiropyran-Modified Nanochannels, Advanced Materials **30**, 1804862 (2018).
[54] I. Vlassiouk, T. R. Kozel, and Z. S. Siwy, Biosensing with Nanofluidic Diodes, J. Am. Chem. Soc. **131**, 8211 (2009).
[55] W. Guo et al., Current Rectification in Temperature-Responsive Single Nanopores, ChemPhysChem **11**, 859 (2010).
[56] T.-J. Liu, T. Ma, C.-Y. Lin, S. Balme, and J.-P. Hsu, Origin of Ultrahigh Rectification in Polyelectrolyte Bilayers Modified Conical Nanopores, J. Phys. Chem. Lett. **12**, 11858 (2021).
[57] F. Montagne, J. Polesel-Maris, R. Pugin, and H. Heinzelmann, Poly(N-isopropylacrylamide) Thin Films Densely Grafted onto Gold Surface: Preparation, Characterization, and Dynamic AFM Study of Temperature-Induced Chain Conformational Changes, Langmuir **25**, 983 (2009).
[58] A. Douaki, T. N. Tran, G. Suarato, L. Bertolacci, L. Petti, P. Lugli, E. L. Papadopoulou, and A. Athanassiou, Thermo-responsive nanofibers for on-demand biocompound delivery platform, Chemical Engineering Journal **445**, 136744 (2022).
[59] H. Alem, A. M. Jonas, and S. Demoustier-Champagne, Poly(N-isopropylacrylamide) grafted into nanopores: Thermo-responsive behaviour in the presence of different salts, Polymer Degradation and Stability **95**, 327 (2010).
[60] J. Andersson, J. Svirelis, J. Medin, J. Järlebark, R. Hailes, and A. Dahlin, Pore performance: artificial nanoscale constructs that mimic the biomolecular transport of the nuclear pore complex, Nanoscale Adv. **4**, 4925 (2022).
[61] B. Yameen, M. Ali, R. Neumann, W. Ensinger, W. Knoll, and O. Azzaroni, Ionic Transport Through Single Solid-State Nanopores Controlled with Thermally Nanoactuated Macromolecular Gates, Small **5**, 1287 (2009).
[62] S. W. Kowalczyk, A. Y. Grosberg, Y. Rabin, and C. Dekker, Modeling the conductance and DNA blockade of solid-state nanopores, Nanotechnology **22**, 315101 (2011).
[63] L. Yang, X. Fan, J. Zhang, and J. Ju, Preparation and Characterization of Thermoresponsive Poly(N-Isopropylacrylamide) for Cell Culture Applications, Polymers **12**, 389 (2020).
[64] M. Santhamoorthy, T. T. Vy Phan, V. Ramkumar, C. J. Raorane, K. Thirupathi, and S.-C. Kim, Thermo-Sensitive Poly (N-isopropylacrylamide-co-polyacrylamide) Hydrogel for pH-Responsive Therapeutic Delivery, Polymers **14**, 4128 (2022).
[65] J. Tan, Q. Yang, G. Hu, H. Zhang, L. Pei, and J. Wang, Experimental study on the temperature-sensitive behavior of poly-n-isopropylacrylamide/graphene oxide composites and the flexible conductive cotton fabrics, Polymer Testing **110**, 107563 (2022).
[66] M. H. Futscher, M. Philipp, P. Müller-Buschbaum, and A. Schulte, The Role of Backbone Hydration of Poly(N-isopropyl acrylamide) Across the Volume Phase Transition Compared to its Monomer, Sci Rep **7**, 17012 (2017).

[67] B. D. Vogt, E. K. Lin, W. Wu, and C. C. White, Effect of Film Thickness on the Validity of the Sauerbrey Equation for Hydrated Polyelectrolyte Films, J. Phys. Chem. B **108**, 12685 (2004).
[68] C. R. Crick, P. Albella, B. Ng, A. P. Ivanov, T. Roschuk, M. P. Cecchini, F. Bresme, S. A. Maier, and J. B. Edel, Precise Attoliter Temperature Control of Nanopore Sensors Using a Nanoplasmonic Bullseye, Nano Lett. **15**, 553 (2015).
[69] M. Tsutsui, A. Arima, K. Yokota, Y. Baba, and T. Kawai, Ionic heat dissipation in solid-state pores, Science Advances **8**, eabl7002 (2022).
[70] A. Keerthi, S. Goutham, Y. You, P. Iamprasertkun, R. A. W. Dryfe, A. K. Geim, and B. Radha, Water friction in nanofluidic channels made from two-dimensional crystals, Nat Commun **12**, 3092 (2021).
[71] A. Noy and S. B. Darling, Nanofluidic computing makes a splash, Science **379**, 143 (2023).
[72] Y. Cui, H. Guo, X. Yan, W. Zhou, Q. Ye, C. Ying, Z. Liu, and J. Tian, Nonlinear and Anisotropic Ion Transport in Black Phosphorus Nanochannels, Nano Lett. **23**, 5886 (2023).
[73] W. Yang, B. Radha, A. Choudhary, Y. You, G. Mettela, A. K. Geim, A. Aksimentiev, A. Keerthi, and C. Dekker, Translocation of DNA through Ultrathin Nanoslits, Advanced Materials **33**, 2007682 (2021).
[74] K. Liu, J. Feng, A. Kis, and A. Radenovic, Atomically Thin Molybdenum Disulfide Nanopores with High Sensitivity for DNA Translocation, ACS Nano **8**, 2504 (2014).
[75] P. Wei, M. Kansari, and M. Fyta, Graphene or MoS2 nanopores: pore adhesion and protein linearization, Nanoscale **17**, 3873 (2025).
[76] C. Gu, Z. Yu, X. Li, X. Zhu, Z. Cao, Z. Ye, C. Jin, and Y. Liu, Experimental study of protein translocation through MoS2 nanopores, Applied Physics Letters **115**, 223702 (2019).
[77] S.-C. Chen, C.-Y. Lin, T.-L. Cheng, and W.-L. Tseng, 6-Mercaptopurine-Induced Fluorescence Quenching of Monolayer MoS2 Nanodots: Applications to Glutathione Sensing, Cellular Imaging, and Glutathione-Stimulated Drug Delivery, Advanced Functional Materials **27**, 1702452 (2017).
[78] M. Tsutsui, W.-L. Hsu, D. Garoli, I. W. Leong, K. Yokota, H. Daiguji, and T. Kawai, Gate-All-Around Nanopore Osmotic Power Generators, ACS Nano **18**, 15046 (2024).
[79] H. Hong, X. Lei, J. Wei, Y. Zhang, Y. Zhang, J. Sun, G. Zhang, P. M. Sarro, and Z. Liu, Rectification in Ionic Field Effect Transistors Based on Single Crystal Silicon Nanopore, Adv Elect Materials 2300782 (2024).
[80] C.-Y. Lin, E. Turker Acar, J. W. Polster, K. Lin, J.-P. Hsu, and Z. S. Siwy, Modulation of Charge Density and Charge Polarity of Nanopore Wall by Salt Gradient and Voltage, ACS Nano **13**, 9868 (2019).
[81] N. Di Fiori, A. Squires, D. Bar, T. Gilboa, T. D. Moustakas, and A. Meller, Optoelectronic control of surface charge and translocation dynamics in solid-state nanopores, Nature Nanotech **8**, 946 (2013).
[82] S.-W. Nam, M. J. Rooks, K.-B. Kim, and S. M. Rossnagel, Ionic Field Effect Transistors with Sub-10 nm Multiple Nanopores, Nano Lett. **9**, 2044 (2009).
[83] Y. Xue, Y. Xia, S. Yang, Y. Alsaid, K. Y. Fong, Y. Wang, and X. Zhang, Atomic-scale ion transistor with ultrahigh diffusivity, Science **372**, 501 (2021).
[84] L. Yang et al., Chloride Molecular Doping Technique on 2D Materials: WS2 and MoS2, Nano Lett. **14**, 6275 (2014).

[85] Y. Li, C.-Y. Xu, P. Hu, and L. Zhen, Carrier Control of MoS2 Nanoflakes by Functional Self-Assembled Monolayers, ACS Nano **7**, 7795 (2013).
[86] X. Chen, N. C. Berner, C. Backes, G. S. Duesberg, and A. R. McDonald, Functionalization of Two-Dimensional MoS2: On the Reaction Between MoS2 and Organic Thiols, Angewandte Chemie **128**, 5897 (2016).
[87] S. Kwon, M. H. Kwon, J. Song, E. Kim, Y. Kim, B. R. Kim, J. K. Hyun, S. W. Lee, and D.-W. Kim, Light-Induced Surface Potential Modification in MoS2 Monolayers on Au Nanostripe Arrays, Sci Rep **9**, 14434 (2019).
[88] C. Nie, B. Zhang, Y. Gao, M. Yin, X. Yi, C. Zhao, Y. Zhang, L. Luo, and S. Wang, Thickness-Dependent Enhancement of Electronic Mobility of MoS2 Transistors via Surface Functionalization, J. Phys. Chem. C **124**, 16943 (2020).
[89] C. J. McClellan, E. Yalon, K. K. H. Smithe, S. V. Suryavanshi, and E. Pop, High Current Density in Monolayer MoS2 Doped by AlOx, ACS Nano **15**, 1587 (2021).
[90] M. A. Alibakhshi, X. Kang, D. Clymer, Z. Zhang, A. Vargas, V. Meunier, and M. Wanunu, Scaled-Up Synthesis of Freestanding Molybdenum Disulfide Membranes for Nanopore Sensing, Advanced Materials **35**, 2207089 (2023).
[91] Y. Huang et al., Universal mechanical exfoliation of large-area 2D crystals, Nat Commun **11**, 2453 (2020).
[92] M. D. Siao, W. C. Shen, R. S. Chen, Z. W. Chang, M. C. Shih, Y. P. Chiu, and C.-M. Cheng, Two-dimensional electronic transport and surface electron accumulation in MoS2, Nat Commun **9**, 1442 (2018).
[93] D. Mosconi et al., Site-Selective Integration of MoS_2 Flakes on Nanopores by Means of Electrophoretic Deposition, Acs Omega **4**, 9294 (2019).
[94] B. Yang, B. Bhujel, D. G. Chica, E. J. Telford, X. Roy, F. Ibrahim, M. Chshiev, M. Cosset-Chéneau, and B. J. van Wees, Electrostatically controlled spin polarization in Graphene-CrSBr magnetic proximity heterostructures, Nat Commun **15**, 4459 (2024).
[95] P. J. Zomer, M. H. D. Guimarães, J. C. Brant, N. Tombros, and B. J. Van Wees, Fast pick up technique for high quality heterostructures of bilayer graphene and hexagonal boron nitride, Applied Physics Letters **105**, 013101 (2014).
[96] D. G. Purdie, N. M. Pugno, T. Taniguchi, K. Watanabe, A. C. Ferrari, and A. Lombardo, Cleaning interfaces in layered materials heterostructures, Nat Commun **9**, 5387 (2018).
[97] J. Feng, K. Liu, M. Graf, D. Dumcenco, A. Kis, M. Di Ventra, and A. Radenovic, Observation of ionic Coulomb blockade in nanopores, Nature Mater **15**, 8 (2016).
[98] D. Stein, M. Kruithof, and C. Dekker, Surface-Charge-Governed Ion Transport in Nanofluidic Channels, Phys. Rev. Lett. **93**, 035901 (2004).
[99] S. Goutham, R. K. Gogoi, H. Jyothilal, G.-H. Nam, A. Ismail, S. V. Pandey, A. Keerthi, and B. Radha, Electric Field Mediated Unclogging of Angstrom-Scale Channels, Small Methods **n/a**, 2400961 (2024).
[100] I. V. Sabaraya, H. Shin, X. Li, R. Hoq, J. A. C. Incorvia, M. J. Kirisits, and N. B. Saleh, Role of Electrostatics in the Heterogeneous Interaction of Two-Dimensional Engineered MoS2 Nanosheets and Natural Clay Colloids: Influence of pH and Natural Organic Matter, Environ. Sci. Technol. **55**, 919 (2021).
[101] K. Lin, Z. Li, Y. Tao, K. Li, H. Yang, J. Ma, T. Li, J. Sha, and Y. Chen, Surface Charge Density Inside a Silicon Nitride Nanopore, Langmuir **37**, 10521 (2021).

[102] G.-C. Liu, M.-J. Gao, W. Chen, X.-Y. Hu, L.-B. Song, B. Liu, and Y.-D. Zhao, pH-modulated ion-current rectification in a cysteine-functionalized glass nanopipette, Electrochemistry Communications **97**, 6 (2018).
[103] Y. Zeng, F. He, Q. Wang, X. Yan, and G. Xie, Friction and wear behaviors of molybdenum disulfide nanosheets under normal electric field, Applied Surface Science **455**, 527 (2018).
[104] Z. Wang et al., Visualizing the role of applied voltage in non-metal electrocatalysts, Natl Sci Rev **10**, nwad166 (2023).
[105] H. Yang, S. Zeng, Y. Hu, Z. Zhang, and Z. Sun, Back Gated Electronic Mapping of 2D Transition Metal Dichalcogenides, ACS Appl. Electron. Mater. **7**, 6784 (2025).
[106] R. Dagan, Y. Vaknin, and Y. Rosenwaks, Gap state distribution and Fermi level pinning in monolayer to multilayer MoS_2 field effect transistors, Nanoscale **12**, 8883 (2020).
[107] F. Mortier, D. Zhao, M. Otani, S. Bernard, Y. Wang, and A. Bouzid, First-principles investigation of electrified monolayered MoS2/water interface, Surface Science **764**, 122870 (2026).
[108] R. Fan, M. Yue, R. Karnik, A. Majumdar, and P. Yang, Polarity Switching and Transient Responses in Single Nanotube Nanofluidic Transistors, Phys. Rev. Lett. **95**, 086607 (2005).
[109] D. Wu et al., Uncovering edge states and electrical inhomogeneity in MoS_2 field-effect transistors, Proc. Natl. Acad. Sci. U.S.A. **113**, 8583 (2016).
[110] Sparse multi-nanopore osmotic power generators, Cell Reports Physical Science **3**, 101065 (2022).
[111] M. Tsutsui, K. Yokota, I. W. Leong, Y. He, and T. Kawai, Protocol for preparation of solid-state multipore osmotic power generators, STAR Protocols **4**, 102227 (2023).
[112] J. Feng, M. Graf, K. Liu, D. Ovchinnikov, D. Dumcenco, M. Heiranian, V. Nandigana, N. R. Aluru, A. Kis, and A. Radenovic, Single-layer MoS2 nanopores as nanopower generators, Nature **536**, 197 (2016).
[113] T. Xiao, W. Yu, X. Li, Z. Liu, B. Lu, W. Lei, and J. Zhai, Multilevel geometric optimization in nanochannel membranes for osmotic energy conversion, Journal of Membrane Science **722**, 123912 (2025).
[114] T. Xiao, X. Li, W. Yu, Z. Liu, W. Lei, and J. Zhai, Two-dimensional nanofluidic channels with Janus heterostructures for highly rectified ion transport, Journal of Membrane Science **713**, 123397 (2025).
[115] T. Xiao, X. Li, Z. Liu, B. Lu, and J. Zhai, The nanoscale modulation of interlayer space in two-dimensional nanoclay membranes for osmotic energy conversion, Journal of Membrane Science **695**, 122456 (2024).
[116] M. Graf, M. Lihter, D. Unuchek, A. Sarathy, J.-P. Leburton, A. Kis, and A. Radenovic, Light-Enhanced Blue Energy Generation Using MoS2 Nanopores, Joule **3**, 1549 (2019).
[117] R. C. Rollings, A. T. Kuan, and J. A. Golovchenko, Ion selectivity of graphene nanopores, Nat Commun **7**, 1 (2016).
[118] C. Plesa, S. W. Kowalczyk, R. Zinsmeester, A. Y. Grosberg, Y. Rabin, and C. Dekker, Fast Translocation of Proteins through Solid State Nanopores, Nano Lett. **13**, 658 (2013).
[119] L. Restrepo-Pérez, S. John, A. Aksimentiev, C. Joo, and C. Dekker, SDS-assisted protein transport through solid-state nanopores, Nanoscale **9**, 11685 (2017).

[120] N. Soni, N. Freundlich, S. Ohayon, D. Huttner, and A. Meller, Single-File Translocation Dynamics of SDS-Denatured, Whole Proteins through Sub-5 nm Solid-State Nanopores, Acs Nano **16**, 11405 (2022).
[121] A. Han, G. Schürmann, G. Mondin, R. A. Bitterli, N. G. Hegelbach, N. F. De Rooij, and U. Staufer, Sensing protein molecules using nanofabricated pores, Applied Physics Letters **88**, 093901 (2006).
[122] A. Valstar, M. Almgren, W. Brown, and M. Vasilescu, The Interaction of Bovine Serum Albumin with Surfactants Studied by Light Scattering, Langmuir **16**, 922 (2000).
[123] Q. Liu, Y. Liu, B. Lu, Y. Wang, Y. Xu, J. Zhai, and X. Fan, A high rectification ratio nanofluidic diode induced by an "ion pool," RSC Adv. **10**, 7377 (2020).
[124] V. V. R. Nandigana, K. Jo, A. Timperman, and N. R. Aluru, Asymmetric-Fluidic-Reservoirs Induced High Rectification Nanofluidic Diode, Sci Rep **8**, 13941 (2018).
[125] E. C. Yusko, R. An, and M. Mayer, Electroosmotic Flow Can Generate Ion Current Rectification in Nano- and Micropores, ACS Nano **4**, 477 (2010).
[126] H. Daiguji, Y. Oka, and K. Shirono, Nanofluidic Diode and Bipolar Transistor, Nano Lett. **5**, 2274 (2005).
[127] L. Chua, If it's pinched it's a memristor, Semicond. Sci. Technol. **29**, 104001 (2014).
[128] L. Luo, D. A. Holden, W.-J. Lan, and H. S. White, Tunable Negative Differential Electrolyte Resistance in a Conical Nanopore in Glass, ACS Nano **6**, 6507 (2012).
[129] G. Laucirica, L. M. H. Parra, A. L. Huamani, M. F. Wagner, A. G. Albesa, M. E. Toimil-Molares, W. Marmisollé, and O. Azzaroni, Insight into the transport of ions from salts of moderated solubility through nanochannels: negative incremental resistance assisted by geometry, Nanoscale **16**, 12599 (2024).
[130] M. Ni and B. D. Ratner, Nacre surface transformation to hydroxyapatite in a phosphate buffer solution, Biomaterials **24**, 4323 (2003).
[131] M. Tsutsui, K. Yokota, W. L. Hsu, D. Garoli, H. Daiguji, and T. Kawai, Peltier cooling for thermal management in nanofluidic devices, Device **2**, (2024).
[132] M. Tsutsui, A. Arima, K. Yokota, Y. Baba, and T. Kawai, Ionic heat dissipation in solid-state pores, Science Advances **8**, eabl7002 (2022).
[133] Z. J. Coppens, W. Li, D. G. Walker, and J. G. Valentine, Probing and Controlling Photothermal Heat Generation in Plasmonic Nanostructures, Nano Lett. **13**, 1023 (2013).
[134] S. Garaj, W. Hubbard, A. Reina, J. Kong, D. Branton, and J. A. Golovchenko, Graphene as a subnanometre trans-electrode membrane, Nature **467**, 190 (2010).
[135] C. Lee, L. Joly, A. Siria, A.-L. Biance, R. Fulcrand, and L. Bocquet, Large Apparent Electric Size of Solid-State Nanopores Due to Spatially Extended Surface Conduction, Nano Lett. **12**, 4037 (2012).
[136] E. C. Yusko, Y. N. Billeh, and M. Mayer, Current oscillations generated by precipitate formation in the mixing zone between two solutions inside a nanopore, J. Phys.: Condens. Matter **22**, 454127 (2010).
[137] B. Vilozny, P. Actis, R. A. Seger, and N. Pourmand, Dynamic control of nanoprecipitation in a nanopipette, ACS Nano **5**, 3191 (2011).
[138] F. M. Maddar, D. Perry, and P. R. Unwin, Confined Crystallization of Organic Materials in Nanopipettes: Tracking the Early Stages of Crystal Growth and Making Seeds for Unusual Polymorphs, Crystal Growth & Design **17**, 6565 (2017).

[139] L. Shi and A. Majumdar, Recent Developments in Micro and Nanoscale Thermometry, Microscale Thermophysical Engineering **5**, 251 (2001).
[140] G. Nagashima, E. V. Levine, D. P. Hoogerheide, M. M. Burns, and J. A. Golovchenko, Superheating and Homogeneous Single Bubble Nucleation in a Solid-State Nanopore, Phys. Rev. Lett. **113**, 024506 (2014).
[141] B. Puzio, M. Manecki, and M. Kwaśniak-Kominek, Transition from Endothermic to Exothermic Dissolution of Hydroxyapatite Ca5(PO4)3OH–Johnbaumite Ca5(AsO4)3OH Solid Solution Series at Temperatures Ranging from 5 to 65 °C, Minerals **8**, 281 (2018).
[142] J. Li et al., Sparse matrix multiplication in a record-low power self-rectifying memristor array for scientific computing, Science Advances **9**, eadf7474 (2023).
[143] T. Emmerich, Y. Teng, N. Ronceray, E. Lopriore, R. Chiesa, A. Chernev, V. Artemov, M. Di Ventra, A. Kis, and A. Radenovic, Nanofluidic logic with mechano–ionic memristive switches, Nat Electron **7**, 271 (2024).
[144] L. M. Uriarte, J. Dubessy, P. Boulet, V. G. Baonza, I. Bihannic, and P. Robert, Reference Raman spectra of synthesized CaCl2 · nH2O solids (n = 0, 2, 4, 6), Journal of Raman Spectroscopy **46**, 822 (2015).
[145] S. Zhai, X. Wu, and E. Ito, High-pressure Raman spectra of tuite, γ-Ca3(PO4)2, Journal of Raman Spectroscopy **41**, 1011 (2010).
[146] G. Neher and T. T. Salguero, δ-Polymorph of Manganese Phosphate, Crystal Growth & Design **17**, 4864 (2017).
[147] L. Wang and G. H. Nancollas, Calcium Orthophosphates: Crystallization and Dissolution, Chem Rev **108**, 4628 (2008).

List of Publications

[1] Banerjee, S., Mattarozzi, L., Maccaferri, N., Cattarin, S., **Weng, S.**, Douaki, A., ... & Garoli, D. (2024). Porous aluminum decorated with rhodium nanoparticles: preparation and use as a platform for UV SERS. *Materials Advances*, *5*(15), 6248-6254.

[2] Lanzavecchia, G., Sapunova, A., Douaki, A., **Weng, S.**, Momotenko, D., Paulo, G., ... & Garoli, D. (2024). Tailored Fabrication of 3D Nanopores Made of Dielectric Oxides for Multiple Nanoscale Applications. *Nano Letters*, *24*(33), 10098-10105.

[3] Douaki, A., **Weng, S.**, Lanzavecchia, G., Sapunova, A., Stuber, A., Nanni, G., ... & Garoli, D. (2025). Modular Plasmonic Nanopore for Opto-Thermal Gating. *Advanced Optical Materials*, *13*(3), 2402189.

[4] Zou, Y., Ma, Q., Zheng, Z., **Weng, S.**, Acuna, G., Bald, I., & Garoli, D. (2025). Advances and applications of dynamic surface-enhanced Raman spectroscopy (SERS) for single molecule studies. *Nanoscale, 17(7), 3656-3670*.

[5] Tsutsui, M., Hsu, W. L., Hsu, C., Garoli, D., **Weng, S.**, Daiguji, H., & Kawai, T. (2025). Transmembrane voltage-gated nanopores controlled by electrically tunable in-pore chemistry. *Nature Communications*, *16*(1), 1089.

[6] Y. Zou, L. Mattarozzi, H. Jin, Q. Ma, S. Cattarin, S. Weng, A. Douaki, G. Lanzavecchia, K. Kołątaj, C. Nicco, B. Johns, N. Maccaferri, G. Acuna, Z. Zheng, S. Jin and D. Garoli* (2025), "UV-SERS monitoring of plasmons photodegradation of biomolecules on Aluminum platforms decorated with Rhodium nanoparticles ", *Nanoscale Advances*, 7(17), 5212 – 5220

[7] **Weng, S.**, Douaki, A., Tsutsui, M., Lanzavecchia, G., Sapunova, A., Lannetti, L., Giacomello, A., Krahne, R. & Garoli, D. (2026). Gated MoS2/SiN nanochannel for tunable iontransport and protein translocation. *Journal of Nanobiotechnology*, 24:136.

[8]W. Wang, **S. Weng**, A. Douaki, G. Lanzavecchia, Y. Zou, Q. Ma, H. Jin, S. Jin, M. Tsutsui, and D. Garoli*, "Plasmonic nanopore to monitor in-pore chemistry" *Chemical Communications*, *62*(11), 3536-3540.